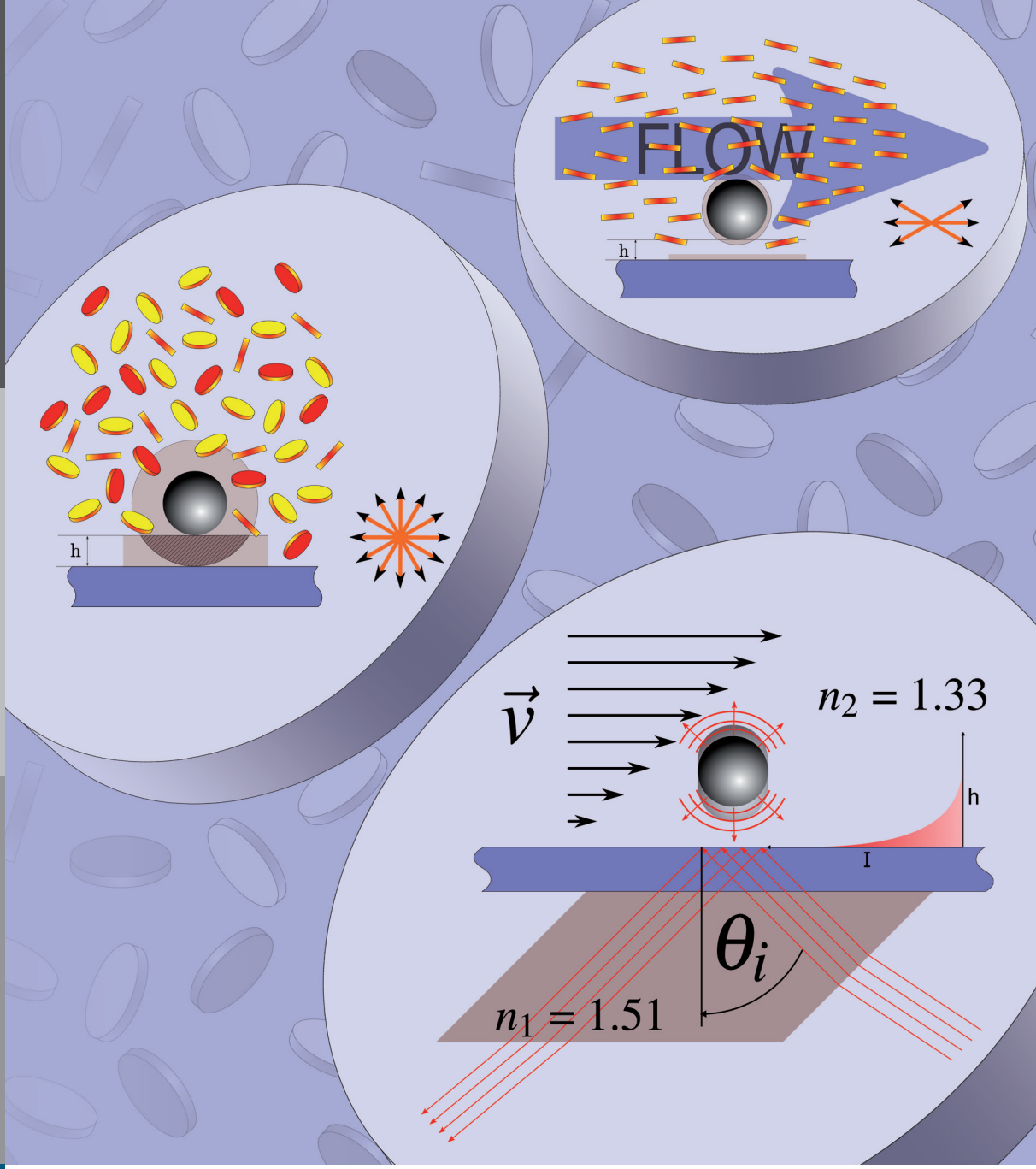

Influence of a shear flow on colloidal depletion interaction

Christoph July

Mitglied in der Helmholtz-Gemeinschaft

JÜLICH
FORSCHUNGSZENTRUM

Schriften des Forschungszentrums Jülich
Reihe Schlüsseltechnologien / Key Technologies Band / Volume 41

Forschungszentrum Jülich GmbH
Institute of Complex Systems (ICS)
Soft Condensed Matter (ICS-3)

Influence of a shear flow on colloidal depletion interaction

Christoph July

Schriften des Forschungszentrums Jülich
Reihe Schlüsseltechnologien / Key Technologies Band / Volume 41

ISSN 1866-1807 ISBN 978-3-89336-791-7

Bibliographic information published by the Deutsche Nationalbibliothek.
The Deutsche Nationalbibliothek lists this publication in the Deutsche Nationalbibliografie; detailed bibliographic data are available in the Internet at http://dnb.d-nb.de.

Publisher and Distributor:	Forschungszentrum Jülich GmbH Zentralbibliothek 52425 Jülich Phone +49 (0) 24 61 61-53 68 · Fax +49 (0) 24 61 61-61 03 e-mail: zb-publikation@fz-juelich.de Internet: http://www.fz-juelich.de/zb
Cover Design:	Grafische Betriebe, Forschungszentrum Jülich GmbH
Printer:	Grafische Betriebe, Forschungszentrum Jülich GmbH
Copyright:	Forschungszentrum Jülich 2012

Schriften des Forschungszentrums Jülich
Reihe Schlüsseltechnologien / Key Technologies Band / Volume 41

D 61 (Diss. Düsseldorf, Univ., 2011)

ISSN 1866-1807
ISBN 978-3-89336-791-7

The complete volume is freely available on the Internet on the Jülicher Open Access Server (JUWEL) at http://www.fz-juelich.de/zb/juwel

Contents

1 Introduction

1.1 Scope of the thesis

In this work colloidal depletion interactions are studied in a quiescent state and under shear flow by means of total internal reflection microscopy (TIRM). Depletion interactions are very weak, entropy driven forces [1], which arise when two or more colloidal particle species are mixed. The first theoretical studies were done by Asakura and Oosawa [2, 3]. The interest in depletion forces is driven by the fact that they are able to influence phase behaviour and self organisation of synthetic and natural colloidal systems [4]. In general, depletion forces are so small that they are difficult to measure by conventional methods such as atomic force microscopy (AFM) [5, 6] or optical tweezers [7]. TIRM is one of the most sensitive methods to probe depletion interactions in colloidal systems [8–10].

This thesis starts with an overview of the fundamental forces acting on a colloid close to a wall (chapter 2). Electrostatic interactions, gravitation, van der Waals forces, and a simple depletion theory are derived for a colloidal sphere in the vicinity of a surface. These theoretical foundations are used as models to fit experimental potentials. Chapter 3 introduces the experimental methods used in this thesis and provides an illustration of the nature of evanescent illumination. The TIRM setup is explained in detail in conjunction with the data evaluation. Sample preparation, measurements of the properties of the used samples, as well as advantages and drawbacks of the employed experimental systems are further discussed in chapter 3. Methods for characterizing samples and cleaning procedures are discussed. In chapter 4, where the results of the thesis are presented, first experiments suggest that using standard TIRM methods result in artifacts when applying a shear flow and trapping the probe particle with optical tweezers at the same time. A significant advancement of this thesis is the modification of the setup in order to remove the unwanted influence of the tweezers when shearing the sample.

This artifact could be exploited in designing a method to measure shear–induced and maybe free rotational diffusion of a spherical colloid by means of TIRM.

Following the development of the setup for the shear affected measurements, the effect of rod–like and platelet shaped depletant agents on the sphere–wall interaction potential are studied. Information about interaction potentials is crucial for the understanding of the bulk behaviour of polymer or colloidal suspensions. Depletion offers a simple way to tune interaction potentials and thereby provide control of phase behaviour and organisation of colloidal crystals [11]. A question yet little investigated is, how depletion is influenced by external force fields, in particular shear gradients. The use of video microscopy techniques such as particle tracking, enables the measurement of multiple probe particles in the field of view. Furthermore, a shear field, created by flowing solvent through a flow cell, can be generated without any restriction to the maximum flow rate. Total internal fluorescence microscopy (TIRF) measurements [12, 13] are made possible without the use of the optical tweezers, providing an increased signal to noise ratio and decreased dependence on the probe particle size.

Static measurements of depletion interaction have to be performed first as reference, in order to understand shear induced changes in sphere–wall interaction potentials. In this work fd virus [14] as rod–like depletant is used. Fd is a bacteriophage in the shape of a long, thin, rigid, nearly monodisperse rod. The depletion behaviour of fd virus is studied over a wide range of depletant mass concentrations in the quiescent state and under flow. In particular, the influence of the finite flexibility of the fd virus is investigated by comparison to a virus mutant, Y21M, which is three times stiffer than the natural virus. The results are compared to theoretical predictions for the depletion caused by long thin rods and literature. Different probe sphere sizes are employed to elucidate a breakdown of the predicted depletion behaviour at high fd mass concentrations. A more detailed analysis of the measured potentials hints at the possibility that fd virus never causes pure depletion behaviour, since the data always deviate from the predictions at short distances. Measurements in shear fields using fd virus as depletant give no solid indication of any effect on the depletion interaction created by a shear gradient.

After studying the depletion behaviour of fd virus, another type of depletant agent is introduced. Platelet induced depletion is investigated on a model system consisting of moderately polydisperse silica coated gibbsite platelets. The platelets are first characterized by TEM measurements. Following TIRF measurements offer the first time a way to measure depletion potentials induced by platelets. To account for the polydispersity of the platelets, a theoretical description for infinitely thin, monodisperse, circular platelets has to be extended. Such modifications make it possible to infer the size distribution by a simple scattering experiment.

Experiments in an applied shear gradient seem to show a reduction of the depletion strength of the platelets with increasing shear rate until the depletion is completely suppressed. For platelet concentrations exceeding the overlap concentration several times, the behaviour is different and corresponds to the observations made with fd virus.

1.2 Motivation

Colloidal systems are prevalent in many commercial and industrial products such as paints, cosmetics, food, lubricants, liquid crystal displays and colored glass. Understanding, characterizing, and tuning the properties of colloidal systems is therefore important for industrial applications. Colloidal systems are not limited to artificial systems as they are also ubiquitous in nature. Blood is a colloidal suspension. Some viruses or bacteria may be modelled by theories developed for colloidal suspensions. Even proteins and the inner workings of cells are colloidal systems in a broader sense. Clays and sandy suspensions are another class of naturally occurring, non biological colloidal systems. Knowledge about non–biological systems is equally important to the biological ones, for example for petroleum production.

Phenomena dealing with Brownian particles of microscopic size are summarized in the field of *soft condensed matter*, which is a subset of *condensed matter physics*. In *condensed matter physics* single atoms and their interplay in solid states are hard to observe and characterize. In contrast, modelling crystals by usage of colloidal particles is comparatively easy and helps to develop a better understanding and extent theoretical concepts in the field of classic solid state physics such as phase transitions in metal alloys or the effect of defects in crystal lattices. The word soft in *soft condensed matter* is coined by the fact that many of the investigated systems are indeed not solid, like gassy dispersions (fog), granular matter (sand), mud or dust.

In order to understand colloidal behaviour, knowledge of the so–called pair interaction potential is crucial. Pair interaction potentials govern the stability and phase behaviour of colloidal suspensions [15]. To infer interaction potentials between colloidal particles, different principle approaches are feasible: observing macroscopic phenomena such as segregation, aggregation, or phase transitions by scattering techniques or by analysing the macroscopic mechanical properties found by rheological measurements, which could yield information about the particle-particle interaction potentials. These indirect observations deliver only an estimate, since a prohibitively large number of factors affect the measured properties. Therefore, these approaches are mostly used to test if some heuristically designed products fulfills the desired expectations [16–18]. Tailoring the properties of new materials requires a more accurate way of determining the interactions between colloidal particles directly. Historically, the only

access to information about pair interaction potentials has been via scattering techniques, like light scattering [19–21]. The resulting structure factor of a colloidal suspension can be related by means of Fourier transformation to the pair correlation function. Here, the pair correlation function is a measure for the pair interaction potentials, which may be inferred with some theoretical input. However, deriving interaction potentials from scattering methods always requires model assumptions, and therefore is prone to misinterpretations, necessitating more direct methods to measure interactions: for instance the surface force apparatus (SFA) [22], optical tweezers [7, 23, 24], atomic force microscopy [25] (AFM) and total internal reflection microscopy (TIRM). Of these, TIRM [26, 27] is the most sensitive, also TIRM has the added benefit of being completely contactless [28] and is especially suited to measure weak interactions. A few examples of the interaction types that have already been investigated by TIRM are van der Waals forces [29], critical casimir forces [30, 31] and colloidal depletion interaction [32–34]. TIRM is an extremely sensitive method to measure sphere–wall interaction potentials, which can be easily connected to the interaction between two colloidal particles. It thereby offers an accurate way to directly study colloidal interaction, otherwise inaccessible by experimental methods. Due to these advantages TIRM is the method of choice in this work.

Depletion forces are of particular interest in biological, and a wide range of technical applications, due to their high degree of tunability [33]. They are used to govern self–organization or to induce phase transitions such as crystallization of proteins [35, 36] and aggregation of colloids [37]. Prominent examples of depletants are spheres and rods [38, 39], because they are theoretically well described [3, 40]. For technical and industrial applications though, a common choice of a depletant is a polymer, such as dextran [41] or polyethylene oxide [42], since they are in comparison much easier to synthesize. Polymers, however, are rather ineffective depletant agents compared to anisotropic colloids such as rod–like or plate–like particles. This ineffectiveness is due to the fact that the depth of the potentials is dictated by the number density and shape of the depleting particle species. In the extreme case of depletion caused by very thin long rods, aside from the number density, only the length governs the strength of the depletion forces. Long rods therefore show very strong depletion effects at low mass concentrations as compared to polymers or other spherical objects of the same size dimension and mass concentration. Depletion interaction potentials caused by colloidal rods have been measured directly [43–47]. As an experimental system, fd virus represents a model for rigid, long, thin, and monodisperse rods [48] with high aspect ratio.

Many studies have focussed on the behaviour of rods. This thesis represents a natural progression in this regard, extending many of these prior studies. In contrast, rigid colloidal platelets have not yet been investigated in a direct depletion study, although platelets are

widely present in nature (clay minerals, red blood cells to name a few) and can be synthesized in a controlled manner in the laboratory (mixed metal hydroxides, gibbsite). The most prominent examples of colloidal platelets are natural clays [49], which are widely used as rheological modifiers for surface coatings, paints, and drilling fluids [50–52]. Their rheological applications are based on their microscopic structural properties originating from the highly anisotropic shape of the colloids and the inter–particle interactions. However, due to the flexibility and the large polydispersity in both size and shape, clay particles are hard to describe theoretically [49]. With the emergence of synthetic systems, analytical theories for plate–like depletant may now be tested.

A further, field of interest is the influence of external force fields on the depletion interaction of colloids. It is known, for instance, that rod–like colloids, such as fd virus may be aligned in strong magnetic field, electrical field or a shear gradient. While experimentally obtainable magnetic fields are usually weak and electrical fields are strongly screened by solvents containing ions, shear is almost always relevant in a colloidal system. As long as a system is not completely quiescent, shear forces provide a mechanism to induce alignment of asymmetrical colloids. These alignments are interesting for meta–stable equilibria or induced phase transitions. Although, it is certainly not trivial to draw conclusions, which are relevant for colloidal ensembles under shear, from potential data obtained with a single particle, the effect of a shear gradient on the depletion potentials of single particles may shed some light on these many body processes.

2 Fundamentals

This chapter will repeat the most basic theoretical concepts needed, in order to explain and understand the measured phenomena. Colloidal interactions between two colloids and a colloid and a wall will be discussed. A simple depletion theory will be derived and the general idea behind depletion interaction will be explained. Furthermore, the fundamental concept of the measurement method will be shown.

2.1 Particle–Wall interactions

In this part some of the most important interactions between a wall and a colloidal particle shall be briefly discussed, as they are essential to understand potentials or rather interaction energies near a surface. During the experiments in general a charged spherical polystyrene particle, floating above a like charged, plane glass surface is observed. Therefore, at not too small separation distances, the forces on the particle are governed by screened electrostatic interaction, so called double layer interaction and the effect of gravitation in combination with light pressure when using optical tweezers. If a particle comes very close to the wall (below 50 nm), usually some effect of van der Waals forces can be found. External force fields or the addition of a depletant agent will have an extra contribution to a measured potential.

2.1.1 Gravitation and light forces

The gravitational force of the earth's gravitational field acts on all colloidal particles. But if particles become too small, usually Brownian motion becomes dominant, so that the particles won't sediment. The probe particles, which are going to be used for the experiments, are in general large enough to be influenced by gravity. Their buoyancy corrected weight force is given by

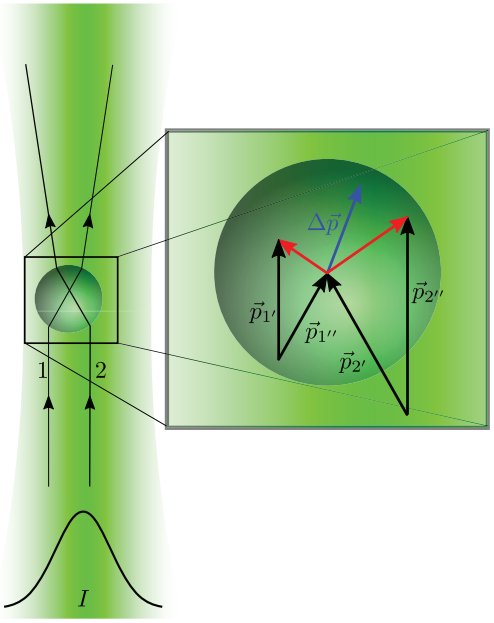

Figure 2.1: *For a particle, which has a higher refractive index than the surrounding medium, the tweezers' laser beam is refracted by a spherical particle in the sketched way. Exemplary two rays (1,2) are picked and the momentum transferred by refraction of these rays onto the sphere is shown. For the case, where the sphere is slightly misaligned with respect to the center of the Gaussian intensity distribution of the tweezers laser, ray 2 impinges with higher intensity and therefore the difference of the momenta $\vec{p}_{2'} - \vec{p}_{2''}$ before and after refraction of a photon is greater than that of ray 1. In this situation the total transfered momentum $\Delta\vec{p}$ has a component pulling the sphere back into the center of the Gaussian beam.*

$$\vec{F}_G = V_p\,(\rho_p - \rho_s)\cdot\vec{g} \tag{2.1}$$

where V_p is the volume of the particle, ρ_p its mass density, ρ_s the mass density of the solvent and $g = 9.81$ m/s^2 the acceleration of gravity. For a bare particle the gravitational force is the only contribution driving the particle to the wall. On the other hand, when working with optical tweezers [53,54], there will be another component pushing it towards the wall, namely the light pressure of the optical trap. Traps used with TIRM employ a low numerical aperture objective, thereby only creating a two dimensional trap. This means there will be no part of the trapping force in perpendicular direction to the wall, dragging the particle into the focal point of the laser beam. The acting forces can be explained by simple ray optics (see Figure 2.1). When the particle is in the center of the light field of the laser beam, which has a Gaussian intensity distribution, it's only propelled in the direction of the Poynting–vector and the exerted light force is proportional to $F_L \propto \mathscr{P}/c$ with $\mathscr{P}$ the power of the tweezers laser and c the speed of light in vacuum. Yet for the case, where the particle is slightly misaligned with respect to the center of the intensity distribution, the momentum transfered onto the particle is different for ray 1 and ray 2 of the light field, being refracted by the sphere (see Figure 2.1). Looking at the difference of the two momenta reveals that the particle is always pulled into the center of the intensity distribution and pushed along the propagation direction. Actually, there will be a second refraction when the beam leaves the particle, but the principle concept stays the

same. A detailed description of low numerical aperture optical tweezers can be found in the pioneering work of A. Ashkin [53]. The tweezers' effect on TIRM measurements has been studied extensively by Walz et al. [54].

As long as the particle is safely trapped in the center of the optical trap, the potential or energy contribution forcing the particle towards the wall is a linear term consisting of the weight force and the radiation pressure.

$$W_{grav}(h) = F_G \cdot h + \mathscr{R}_{sphere} \frac{\mathscr{P}}{c} \cdot h \tag{2.2}$$

The constant $\mathscr{R}_{sphere}$ is a proportionality constant, connected to the Fresnel coefficients for reflection/absorption of the spheres and h the distance from the surface of the wall to the surface of the sphere.

2.1.2 Double layer forces

In order to do experiments the probe particles will need some kind of stabilization to prevent sticking. Here, mainly charge stabilized particles are used. These particles have surface groups, which dissociate ions in a polar solvent, exposing a charged surface, which is repelled by other particles or like charged walls. This prevents the particle from sticking when pushed to the interface by gravitation or the optical tweezers. Furthermore, aggregation of the particles is avoided. In this section the screened Coulomb interaction between a sphere and a wall will be derived to be later used as a model to fit a potential.

2.1.2.1 Screened Coulomb potential of a planar wall

The electrostatic potential, $\psi(x)$, created by an infinitely expanded, charged, planar wall in an electrolyte solution shall be derived. This is somewhat different from the case in vacuum or a solid dielectric, since the ions in solution are allowed to move freely. These conditions necessitate to make some assumptions in order to solve the Poisson equation analytically. One of these assumptions is that the ions of an electrolyte obey a Boltzmann distribution (eq. 2.3). Boltzmann's law combined with the Poisson equation (eq. 2.4) is generally referred to as the Poisson-Boltzmann equation (eq. 2.5).

$$\sum_i \rho^i(x) = \sum_i \rho_0^i e^{-\frac{z_i e \psi(x)}{k_B T}} \tag{2.3}$$

$\rho^i(x)$ is the ion concentration at distance, x, from the wall, ρ_0^i the corresponding bulk ion concentration of ion species i, $\psi(x)$ the potential, e the elementary charge and z_i the valency.

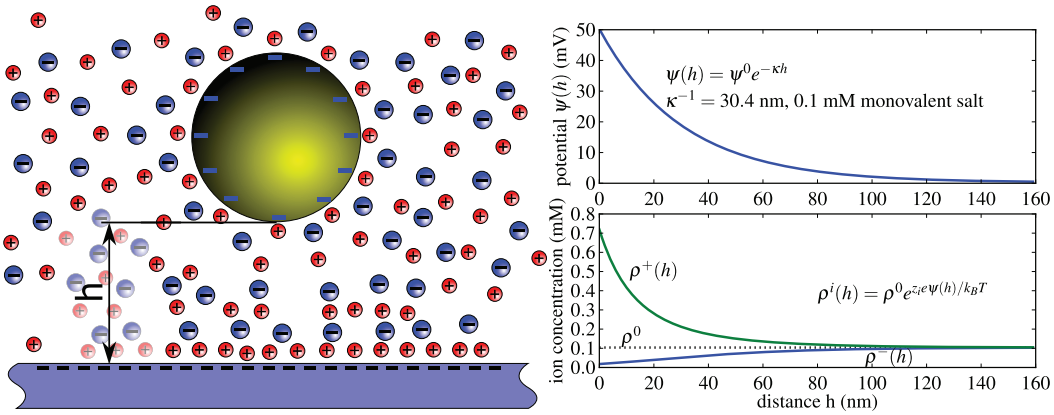

Figure 2.2: *The left picture shows a schematical depiction of a sphere surrounded by counterions and electrolyte ions at a distance, h, from the like charged wall. The right graphs describe the electrostatic potential at distance, h, for a weakly charged system in front of a planar wall for a 0.1 mM 1:1 electrolyte (top), and the corresponding ion density distribution along the surface normal (bottom).*

The potential can be derived by solving the Poisson–Boltzmann equation. In the following summations will be implicitly done when there are indices. For an infinitely expanded wall the problem is one dimensional, so that the Poisson equation becomes

$$\frac{\mathrm{d}^2\psi(x)}{\mathrm{d}x^2} = -\frac{z_i e \rho^i(x)}{\varepsilon_0 \varepsilon}. \tag{2.4}$$

Taking the derivative of eq. 2.3 and substituting with eq. 2.4 yields

$$\begin{aligned}\frac{\mathrm{d}\rho^i(x)}{\mathrm{d}x} &= \underbrace{-\frac{z_i e \rho_0^i}{k_B T} e^{-\frac{z_i e \psi(x)}{k_B T}}}_{-\frac{\varepsilon_0 \varepsilon}{k_B T}\frac{\mathrm{d}^2\psi(x)}{\mathrm{d}x^2}} \frac{\mathrm{d}\psi(x)}{\mathrm{d}x}, \text{ with } \frac{\mathrm{d}^3\psi(x)}{\mathrm{d}x^3} = \frac{1}{2}\frac{\mathrm{d}}{\mathrm{d}x}\left(\frac{\mathrm{d}\psi(x)}{\mathrm{d}x}\right)^2 \\ &= -\frac{\varepsilon_0 \varepsilon}{2 k_B T}\frac{\mathrm{d}}{\mathrm{d}x}\left(\frac{\mathrm{d}\psi(x)}{\mathrm{d}x}\right)^2. \end{aligned} \tag{2.5}$$

Provided that $\psi(\infty) = 0$, integrating this from ∞ to x immediately leads to

$$\rho^i(x) - \rho_0^i = \frac{\varepsilon_0 \varepsilon}{2 k_B T}\left(\frac{\mathrm{d}\psi(x)}{\mathrm{d}x}\right)^2 \tag{2.6}$$

where ρ_0^i is again the bulk density of one electrolyte species at infinite distance. In order to solve eq. 2.6, a concrete situation has to be assumed. The simplest one is a monovalent 1:1

electrolyte, where only two ion species with valency, $z_{+/-} = \pm 1$, and the same bulk density, $\rho^{+/-}(x)$, have to be considered. For this case eq. 2.6 reduces to

$$\begin{aligned}
\rho^-(x) + \rho^+(x) - 2\rho_0 &= \frac{\varepsilon_0 \varepsilon}{2k_B T} \left(\frac{\mathrm{d}\psi(x)}{\mathrm{d}x} \right)^2, \text{ with eq. 2.3} \\
\rho_0 \left(e^{\frac{e\psi(x)}{k_B T}} + e^{\frac{-e\psi(x)}{k_B T}} - 2 \right) &= \frac{\varepsilon_0 \varepsilon}{2k_B T} \left(\frac{\mathrm{d}\psi(x)}{\mathrm{d}x} \right)^2 \\
\rho_0 \left(e^{\frac{-e\psi(x)}{2k_B T}} - e^{\frac{e\psi(x)}{2k_B T}} \right)^2 &= \frac{\varepsilon_0 \varepsilon}{2k_B T} \left(\frac{\mathrm{d}\psi(x)}{\mathrm{d}x} \right)^2 \\
\frac{8\rho_0 k_B T}{\varepsilon_0 \varepsilon} \sinh^2 \left(\frac{e\psi(x)}{2k_B T} \right) &= \left(\frac{\mathrm{d}\psi(x)}{\mathrm{d}x} \right)^2,
\end{aligned}$$

which finally gives

$$\frac{\mathrm{d}\psi(x)}{\mathrm{d}x} = \pm \sqrt{\frac{8\rho_0 k_B T}{\varepsilon_0 \varepsilon}} \sinh \left(\frac{e\psi(x)}{2k_B T} \right). \tag{2.7}$$

The positive solution is unphysical and will be disregarded. Now the only thing left to do is to solve this differential equation. To do so, $y = e\psi(x)/2k_B T$ is substituted, so that

$$\frac{\mathrm{d}y}{\mathrm{d}x} = \frac{e}{2k_B T} \frac{\mathrm{d}\psi(x)}{\mathrm{d}x}. \tag{2.8}$$

Inserting eq. 2.8 in eq. 2.7 results, after some reforming, in

$$\frac{\mathrm{d}y}{\sinh(y)} = -\sqrt{\frac{2e^2 \rho_0}{\varepsilon_0 \varepsilon k_B T}} \mathrm{d}x. \tag{2.9}$$

In eq. 2.9 the inverse Debye length, $\kappa = \sqrt{e^2 \sum_i \rho_0^i / \varepsilon_0 \varepsilon k_B T}$, can be identified. The Debye length is a measure for the range or the screening of the potential in electrolyte solutions. In order to solve the differential equation both sides are integrated.

$$\int_{y_s}^{y} \frac{\mathrm{d}y'}{\sinh(y')} = -\int_0^x \mathrm{d}x' \kappa \tag{2.10}$$

The solution to this differential equation is found by using a tabulated integral:

$$\begin{aligned} \ln\left(\frac{\tanh(y/2)}{\tanh(y_s/2)}\right) &= -x\kappa \\ \tanh(y/2) &= \underbrace{\tanh(y_s/2)}_{\gamma} e^{-\kappa x} \end{aligned} \tag{2.11}$$

where $y_s = y(0)$. For the final steps the inverse of the hyperbolic tangent will be used.

$$\tanh^{-1}(X) = \frac{1}{2}\ln\left(\frac{1+X}{1-X}\right) \tag{2.12}$$

With this inverse function and the use of the Taylor expansion ($\gamma e^{-\kappa x} \ll 1$) to the first order eq. 2.11 further simplifies to

$$y = \ln\left(\frac{1+\gamma e^{-\kappa x}}{1-\gamma e^{-\kappa x}}\right) \approx \ln\left(1+2\gamma e^{-\kappa x}\right) \approx 2\gamma e^{-\kappa x}. \tag{2.13}$$

Lastly, this gives the electrostatic potential at distance, x, for an infinitely extended plate in a monovalent 1:1 electrolyte.

$$\psi(x) = \frac{4k_BT}{e}\tanh\left(\frac{e}{2k_BT}\psi_0\right)e^{-\kappa x} \tag{2.14}$$

If the surface potential, ψ_0, is smaller than k_BT, the term may even be further approximated by expanding the tanh into a Taylor series, leaving only eq. 2.15.

$$\psi(x) \approx \psi_0 e^{-\kappa x} \tag{2.15}$$

This so called Debye–Hückel limit is a good approximation for low potentials ($\psi_0 \leq 25$ mV), respectively weakly charged systems at high temperatures. Further, it is the model used to calculate the potential in Figure 2.2. The term electric double layer actually stems from more elaborate theories [55, 56], where ions of opposite charge are predicted to condense on a charged surface, thereby creating two layers. For the data gathered in this thesis, the model, presented here, is more than sufficient.

In order to establish a connection to the surface charge of the wall, the boundary condition of electroneutrality is utilized. The following relation is known as the Grahame equation. The charge on the surface of the wall has to cancel out with the charge in solution:

$$\sigma = -\int_0^\infty \mathrm{d}x' z_i e \rho^i(x') \overset{(2.4)}{=} \varepsilon\varepsilon_0 \int_0^\infty \mathrm{d}x' \frac{\mathrm{d}^2\psi(x')}{\mathrm{d}x'^2} = -\varepsilon\varepsilon_0 \left.\frac{\mathrm{d}\psi(x)}{\mathrm{d}x}\right|_{x=0} \tag{2.16}$$

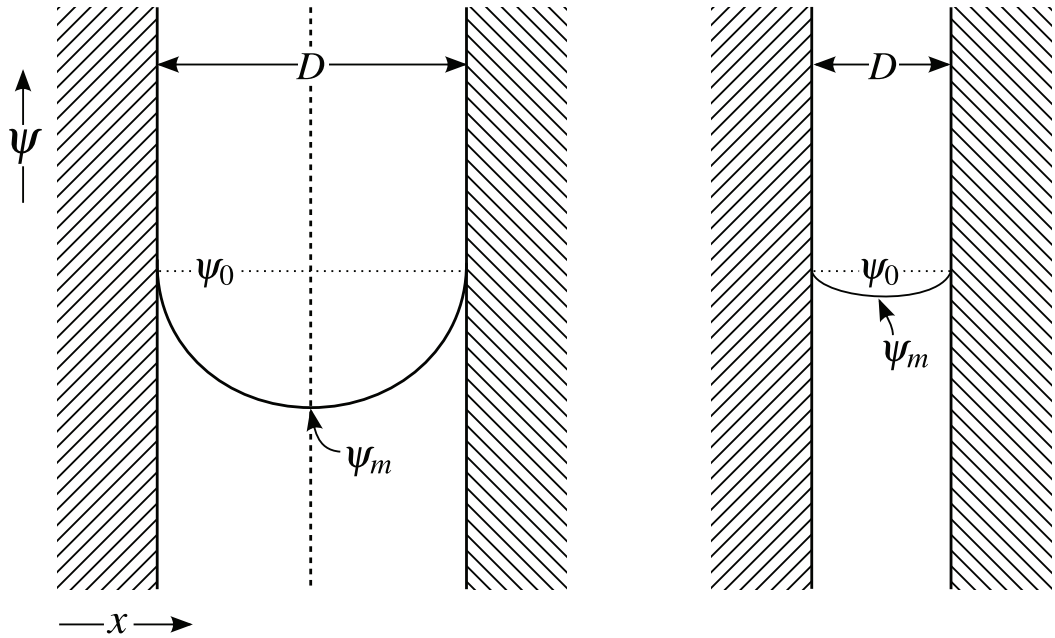

Figure 2.3: *Change of the electrostatic potential in a gap between two plates, surrounded by an electrolyte solution when the gap–width is decreased. Boundary conditions have always to be met, which causes the potential derivation to become zero in the middle of the gap. The surface potential, ψ_0, stays constant and is independent of the gap–width*

In the case of a monovalent 1:1 electrolyte the derivation of the potential is already known (eq. 2.7), so the surface charge, σ, becomes

$$\sigma = \varepsilon\varepsilon_0 \sqrt{\frac{8\rho_0 k_B T}{\varepsilon_0 \varepsilon}} \sinh\left(\frac{e\psi_0}{2k_B T}\right) \tag{2.17}$$

and for low potentials this may be further simplified to

$$\sigma = \varepsilon\varepsilon_0 \kappa \psi_0. \tag{2.18}$$

For further details, it is referred to standard literature [57, 58].

2.1.2.2 Interaction energy between two planar walls

Now that an expression for the electrostatic potential of a planar wall in an electrolyte solution is known, the energy required, bringing two plates within a distance, D, can be calculated. The ions will be regarded as an ideal gas and they are thought to exert a pressure on the plates. This

pressure will be different in the gap between the plates than it is outside, therefore resulting in a pressure difference or osmotic pressure, Π_i, leading to a net repulsion or attraction of the plates. An expression for the osmotic pressure can be constructed from the Gibbs–Duhem relation (eq. 2.19) and the chemical potential, μ, for electrolyte solutions [57] (eq. 2.20). Throughout the derivation, it is assumed that the charge on the surfaces of the plates doesn't change at any time and the system is in thermodynamic equilibrium.

$$\mu_i N_i = U_i + \Pi_i V_i - T S_i \tag{2.19}$$

$$\mu_i = z_i e \psi(x) + k_B T \ln \rho^i(x) \tag{2.20}$$

Here, N_i is the number of ions of species i, z_i the ion valency, U_i the internal energy, T the temperature of the system, S_i its entropy and $\rho_i(x)$ the ion density. Provided that the temperature is constant, the total differential of the chemical potential is given by eq. 2.19, leaving for $\mathrm{d}U = 0$ and $\mathrm{d}T = 0$ only eq. 2.21.

$$\mathrm{d}\mu_i = \mathrm{d}\Pi_i \underbrace{\frac{V_i}{N_i}}_{1/\rho^i} \tag{2.21}$$

In combination with the total differential of eq. 2.20 this leads to

$$\begin{aligned} \mathrm{d}\mu_i &= z_i e \mathrm{d}\psi(x) + k_B T \frac{\mathrm{d}\rho^i(x)}{\rho(x)} \Rightarrow \\ \mathrm{d}\Pi_i &= \rho^i(x) \left[z_i e \mathrm{d}\psi(x) + k_B T \frac{\mathrm{d}\rho^i(x)}{\rho^i(x)} \right]. \end{aligned} \tag{2.22}$$

In order to find the pressure on one of the plates, eq. 2.22 is integrated. The pressure in the gap between the two plates is given by integrating the right hand side from infinity to $D/2$.

$$\int_\infty^D \mathrm{d}x' \frac{\mathrm{d}\Pi_i(x')}{\mathrm{d}x'} = \int_\infty^{D/2} \mathrm{d}x' \rho^i(x') z_i e \frac{\mathrm{d}\psi(x)}{\mathrm{d}x'} + k_B T \int_\infty^{D/2} \mathrm{d}x' \frac{\mathrm{d}\rho^i(x')}{\mathrm{d}x'} \tag{2.23}$$

Inserting eq. 2.4 here and defining that $\Pi(\infty) = 0$, this results in:

$$\Pi_i(D) = -\frac{\varepsilon\varepsilon_0}{2} \left(\frac{\mathrm{d}\psi(x)}{\mathrm{d}x} \right)^2 \Bigg|_{x=D/2} + k_B T \left(\rho^i(D/2) - \rho_0^i \right) \tag{2.24}$$

In equilibrium, the boundary conditions dictate that the osmotic pressure is the same everywhere. In order to exploit the symmetry (see Figure 2.3), the middle of the gap is chosen to determine the osmotic pressure, where $\mathrm{d}\psi(x = D/2)/\mathrm{d}x = 0$, so that at distance, D, of the plates the pressure becomes

$$\Pi_i(D) = k_B T \left(\rho^i(D/2) - \rho_0^i\right). \tag{2.25}$$

For a monovalent 1:1 electrolyte eq. 2.6 and eq. 2.7 are compared to yield

$$\left(\rho^i(x) - \rho_0^i\right) = 4\rho_0 \sinh^2\left(\frac{e\psi(x)}{2k_B T}\right) \approx \rho_0 \left(\frac{e\psi(x)}{k_B T}\right)^2. \tag{2.26}$$

Inserting this into eq. 2.25 gives

$$\Pi(D) = \frac{\rho_0 e^2 \psi(D/2)^2}{k_B T}. \tag{2.27}$$

Having already calculated the potential, $\tilde{\psi}(x)$, for a single infinitely expanded wall (eq. 2.14), that can be inserted in eq. 2.27, realizing that $\psi(D/2) = 2\tilde{\psi}(D/2)$ and provided that linear superposition of potentials holds for not too small gap widths D.

$$\Pi(D) = 64 k_B T \rho_0 \tanh^2\left(\frac{e\psi_0}{2k_B T}\right) e^{-\kappa D} \tag{2.28}$$

Up to now only the osmotic pressure acting on the plates is known. In order to calculate the energy per surface area an integration over D has to be performed.

$$w_{el}^{WW}(D) = \int_{\infty}^{D} \mathrm{d}D' \Pi(D') = -\frac{64 k_B T \rho_0}{\kappa} \tanh^2\left(\frac{e\psi_0}{2k_B T}\right) e^{-\kappa D} \tag{2.29}$$

To transfer this result to the interaction energy of a sphere and a wall, the Derjaguin approximation (eq. 2.30) is applied [59, 60].

$$F^{SW}(D) \approx 2\pi R w^{WW}(D) \tag{2.30}$$

with

$$F^{SW}(h) = -\frac{\partial W^{SW}(h)}{\partial h} \tag{2.31}$$

The approximation holds for distances $D = h \ll R$ and $\kappa^{-1} \ll R$, where R is the radius of the sphere. By integration the interaction energy between a sphere and a wall is found to be

$$W_{el}^{SW}(h) = \frac{128\pi R k_B T \rho_0}{\kappa^2} \tanh^2\left(\frac{e\psi_0}{2k_B T}\right) e^{-\kappa h} \tag{2.32}$$

which will usually will be applied in a simplified form.

$$W_{el}^{SW}(h) = Be^{-\kappa h} \tag{2.33}$$

2.1.3 van der Waals forces

Van der Waals forces will only play a negligible role in the experiments, performed in the course of this work. Yet they are ubiquitous and dominating colloidal interactions at short separation distances. Van der Waals forces stem from interactions between dipoles and are present in any kind of material. Generally three types of dipolar interaction are distinguished: forces between permanent dipoles, forces between induced dipoles and dispersion forces. Dispersion forces are found to exist everywhere and are the dominating type. They are the result of quantum mechanical fluctuations within the dipole moment of individual molecules. Although most elements or compounds carry no permanent dipole moment, only their time averaged dipole moments are zero. In the event that two molecules come close enough to each other, the fluctuating dipole moments may start to influence each other, giving rise to a non vanishing dipole moment of the two molecules. In turn this results in an interaction force between the molecules. These forces are usually short ranged, but will show different distance dependencies between macroscopic bodies with respect to the chosen geometry.

2.1.3.1 Dipole forces between a sphere and a wall

To calculate van der Waals interaction in colloidal systems, the interfaces and particles are thought to be assembled of infinitesimal units each obeying the attractive power law expected to be valid for a single molecule [57] (eq. 2.34).

$$w(r) = -\frac{C}{r^6} \tag{2.34}$$

here C is some proportionality constant, which depends on the physical properties of the molecule and r the distance between two molecules. In the following, the interaction between a sphere and a wall shall be derived. First, the potential of all dipoles of an infinitely expanded planar wall at distance, D, acting on a single dipole is calculated (see Figure 2.4). In order to do so, the implicit assumption of pair–wise additivity has to be made. Integration over the whole wall volume is done by dividing the wall into infinitesimal ring volumes $\mathrm{d}V = 2\pi x \mathrm{d}x \mathrm{d}z$

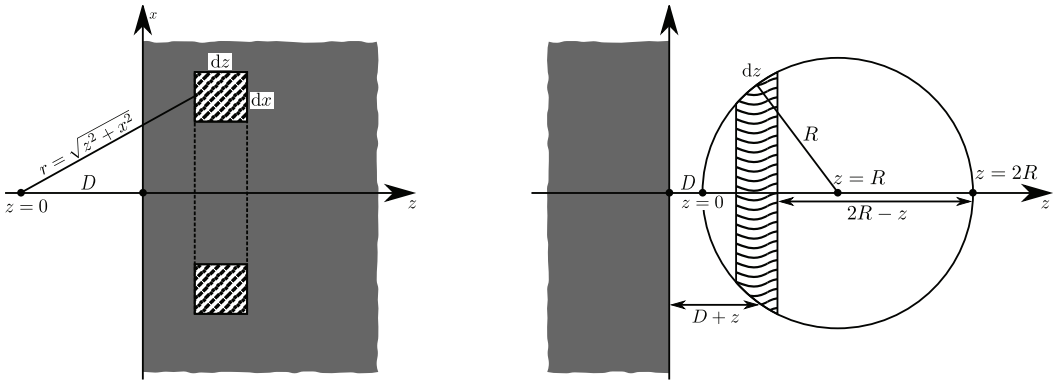

Figure 2.4: *Illustration of integrations used to sum up all single molecule contributions. The left picture shows the chosen integration to find the contribution of an infinitely extended wall by integrating over ring volumes, while the right geometry shows the situation, where the interaction energy of a large sphere with a wall is derived by integration.*

(see Figure 2.4). In each volume $dN = \mathrm{d}V\rho$ molecules have to be considered, where ρ is the molecules' number density.

$$\begin{aligned}
\tilde{w}(D) &= -\int_V \mathrm{d}V \frac{C}{r^6} \\
&= -2\pi C\rho \int_D^\infty \mathrm{d}z \int_0^\infty \mathrm{d}x \frac{x}{(x^2+z^2)^3} \\
&= \frac{2\pi C\rho}{4} \int_D^\infty \mathrm{d}z \, \frac{1}{(x^2+z^2)^2}\Bigg|_0^\infty \\
&= -\frac{2\pi C\rho}{4} \int_D^\infty \mathrm{d}z \frac{1}{z^4} \\
&= -\frac{\pi C\rho}{6D^3}
\end{aligned} \tag{2.35}$$

Eq. 2.35 describes the potential energy a single molecule experiences at a distance, D, from the wall. To extend this to the potential energy for a whole sphere with radius R, an integration over all molecules within the sphere at distance, D, has to be done. To keep the integration simple, only large spheres will be regarded ($D \ll R$). When doing the integration the sphere is viewed as being composed of infinitesimal thin discs with thickness $\mathrm{d}z$, which gives for the volume element $\mathrm{d}V = \pi x^2 \mathrm{d}z = \pi(2R - z)z\mathrm{d}z \approx 2Rz\mathrm{d}z$ (see Figure 2.4). This assumes that only the dipoles at $z \ll R$ contribute significantly to W_{vdw}^{SW}, which is justified by the $1/D^3$ dependence.

$$\begin{aligned} W_{vdw}^{WS}(D) &= \rho \int_0^\infty \mathrm{d}z \tilde{w}(D+z) 2Rz \\ &= -\frac{\pi C \rho^2}{6} \int_0^\infty \mathrm{d}z \frac{2Rz}{(D+z)^3} \\ &= \frac{-\pi^2 \rho^2 CR}{6D} \end{aligned} \tag{2.36}$$

To get the result, a tabulated integral is used. It can be seen that the distance dependence goes with $1/D$, which is quite different from the case of single molecules. The only unknown left is the proportionality constant C.

For brevity's sake $A_H = \pi^2 C \rho_1 \rho_2$ is identified as the Hamaker constant [61], named after H. C. Hamaker. It turns out that pair–wise additivity, which was assumed for the integrations, is generally not fulfilled, because a third dipole close to two others normally alters the interaction drastically, so that only very diluted gases may interact in the described way. Furthermore, the outlined model would only be valid in vacuum and not for interactions within a dielectric medium like a solvent. However, a more thorough derivation shows that the functional form of the interaction (eq. 2.36) is retained and the Hamaker constant can be derived by Lifshitz theory, a continuum theory, avoiding the problem of additivity altogether. In this case, the dielectric properties of the media are used to infer the Hamaker constant. To avoid the quite extensive derivation only an approximate result of Lifshitz theory is given here. For a more rigorous treatment it shall be referred to the book of Isrealachivilly and other works [57,58,61].

$$\begin{aligned} A_H \approx & \frac{3}{4} k_B T \left(\frac{\varepsilon_1 - \varepsilon_3}{\varepsilon_1 + \varepsilon_3} \right) \left(\frac{\varepsilon_2 - \varepsilon_3}{\varepsilon_2 + \varepsilon_3} \right) + \frac{3h\nu_e}{8\sqrt{2}} \\ & \frac{\left(n_1^2 - n_3^2\right) \left((n_2^2 - n_3^2) \right)}{\left(n_1^2 + n_3^2\right)^{1/2} \left(n_2^2 + n_3^2\right)^{1/2} \left[\left(n_1^2 + n_3^2\right)^{1/2} + \left(n_2^2 + n_3^2\right)^{1/2} \right]} \end{aligned} \tag{2.37}$$

The Hamaker constant is composed of two terms: The first one containing ε_1, ε_2, the static dielectric constants of two objects and ε_3 the static dielectric constant of the surrounding medium, representing the contribution of static dipoles. The second term describes the influence of fluctuation forces or dispersion forces, which are dominant in most cases except for materials with a strong permanent dipole moment. In the second term the refractive indices are given by $n_i = \sqrt{\frac{\varepsilon_i}{\varepsilon_0}}$ (ε_0 vacuum permittivity). For metals the quantity, ν_e, is the so called plasma or Langmuir frequency of the material, above which the metal becomes transparent:

$$\nu_e = \sqrt{\frac{n_e e^2}{\varepsilon_0 m_e}} \tag{2.38}$$

where n_e is the electron density and e the elementary charge. It also has to be noted that the mass m_e is not necessarily the mass of a free electron, but an effective mass. For typical dielectric materials the frequency ν_e is attributed to the dominant absorption in the UV region of the electromagnetic spectrum and is of the order of 10^{15} Hz. With the knowledge of the Hamaker constant the van der Waals potential is completely defined. For most materials the Hamaker constant is very small ($A_H = 10^{-20}$ J ≈ 3 kT), which explains the negligible contribution of van der Waals forces at higher distances. As a final remark, it has to be said that the result is only a crude approximation and the Hamaker constant is not really a constant, but rather depends on the distance, too. For the performed experiments van der Waals forces do no contribute significantly for distances greater than 50 nm, while being difficult to quantify with TIRM for lower distances [29].

2.1.4 Depletion forces

Depletion forces arise when two or more types of particles are mixed in a suspension. For the sake of simplicity only a binary mixture of small and large particles, interacting solely by hard body interaction will be considered. Due to purely geometric reasons the smaller particle species (depletant) will be expelled from a volume around the larger particles and the walls of the container. This volume is called depletion zone. If two of the large particles approach each other or such a particle approaches a wall and comes within a distance, which is of the dimension of the smaller particle size, the depletion zones of the two objects start to overlap. As a consequence the total volume accessible to the smaller particles increases, thereby increasing the entropy of the whole system. This increase in entropy leads to an attractive force acting on the larger particles, the so called depletion force, which is limited in range to the size of the depletant. There is also another way to look at depletion forces, which provides a more intuitive picture of the phenomenon. When two of the larger particles come close to each other, the smaller particles are expelled from the created gap. The lower depletant agent number density in the gap creates an imbalance of momentum transfered onto the larger particles, caused by constant collisions between depletant and large particles. Due to the lower particle density in the gap the large particles are pushed towards each other.

2.1.4.1 Depletion caused by rigid rods

In order to calculate the entropic forces caused by a rod–like depletant, in the simplest model the rod system is approximated by an ideal gas. In this picture rod–rod interactions are disregarded, which is justified for dilute suspensions. As soon as the depletion zones of two objects overlap, the total excluded volume shrinks, which is connected only to a change of Helmholtz free energy, ΔF, attributed to an ideal gas.

$$\Delta U = \Delta Q + \Delta W = T\Delta S - \Pi\Delta V = 0 \tag{2.39}$$

The internal energy shall be constant, so that the pressure is connected to the entropy.

$$\Delta F = \Delta U - T\Delta S = \frac{3}{2}\rho k_B \Delta T - \rho k_B T \Delta V \tag{2.40}$$

Actually, the pressure is viewed as an osmotic pressure, $\Pi = N/V k_B T$, while ΔV is the difference in excluded volume. With the assumption that the system has a fixed temperature, T, this simplifies to

$$\Delta F = -\rho k_B T \Delta V \Leftrightarrow W_{dep}^{WW}(D) = \rho k_B T \left(V_{ex}(D) - V_{ex}(D=\infty)\right) \tag{2.41}$$

In the following, the change of the Helmholtz free energy will be identified as the depletion potential $W_{dep}^{WW}(D)$ or rather the interaction energy. A geometry has to be chosen to specifically calculate the depletion potential. The mathematically easiest case are two infinite walls, which are brought close to each other. For this situation the potential depends on the separation distance, D, of the plates (walls) and the bulk depletant density $\rho = N/V$. The range of the potential is given by the rod length. For distances larger than the rod length, L, no force on the plates is exerted.

In a first step the excluded volume for a rod caused by a wall at infinite distance to the other wall will be calculated. Here, the excluded volume is the volume prohibited to a rod's center of mass, given a certain orientation of the rod. Thus, this is synonymous to a reduction of the rod's rotational freedom when the rod approaches a wall. In order to find the volume, inaccessible to a rod near a wall, the rod's center of mass is moved towards the wall, while successively more volume is blocked by the wall as the rod tries to sample all possible angles around its center of mass. For each step, $\mathrm{d}z$, towards the wall an infinitesimal volume, $\mathrm{d}V = (L/2)^2 \sin(\theta)\,\mathrm{d}\theta\mathrm{d}z$, with the shape of a spherical shell becomes inaccessible to the rod (see Figure 2.5). The total excluded volume at infinite wall separation distance is given by an

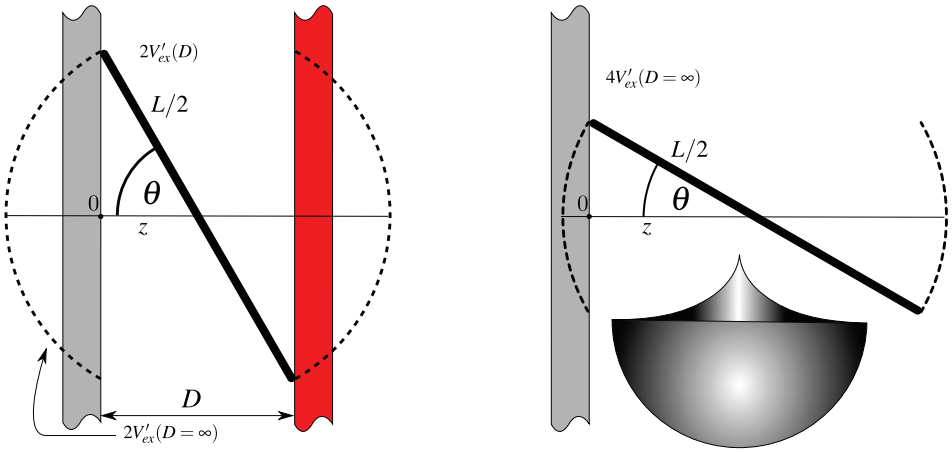

Figure 2.5: *Illustrative sketch to derive the depletion potential caused by rigid rods. The right picture shows the integration limits for deriving the excluded volume caused for a rigid thin rod by a single wall. Any other interface shall be infinitely far away. The total excluded volume is four times the volume found by the integration [two rod ends, two wall surfaces] (mushroom like shape below the picture). The left picture shows what changes when a second wall is present. The two walls restrict the motion of one rod in the same way, at the same time, so that the total excluded volume actually becomes smaller, compared to the single wall case, as the walls get closer.*

integration over z from 0 to $L/2$ with the angle, θ, limited by the points where the rod touches the wall ($\cos\theta = 2z/L$).

$$\begin{aligned} V'_{ex}(D=\infty) &= \frac{L^2}{4}\int_0^{L/2} \mathrm{d}z \int_0^{\arccos(2z/L)} d\theta \sin(\theta) \int_0^{2\pi} d\varphi \\ &= \frac{\pi L^2}{2}\int_0^{L/2} \mathrm{d}z \left(1-\frac{2z}{L}\right) \\ &= \frac{\pi L^2}{8}\cdot L \end{aligned} \tag{2.42}$$

The integral only accounts for one side of a single plate, while the rod will be stopped from entering the excluded volume at both its ends. This means the calculated volume has to be multiplied by four (two sides, two ends) to yield the full excluded volume due to one wall at infinite separation distance.

$$V_{ex}(D=\infty) = 4V'_{ex}(D=\infty) \tag{2.43}$$

If two plates come within a distance $D < L$ the excluded volumes of the two plates overlap.

Because the motion of a rod is already restricted by one of the two plates, the overlapping volume is effectively subtracted from the total excluded volume. The total excluded volume caused by one of the walls inside the gap shrinks upon approach of the plates until it completely vanishes, as soon as the walls touch (because the interface disappears). Its value for one plate may be inferred from a rod confined in the gap. For each distance, D, the rod will be prohibited to enter a distinct volume. The calculation is performed in the same way as in the case of infinite distance, but the upper integration limit for z is set to $D/2$, which accounts for the overlap.

$$\begin{aligned} V'_{ex}(D) &= \frac{L^2}{4}\int_0^{D/2} \mathrm{d}z \int_0^{\arccos(2z/L)} d\theta \sin(\theta) \int_0^{2\pi} d\varphi \\ &= \frac{\pi L^2}{2}\int_0^{D/2} \mathrm{d}z \left(1-\frac{2z}{L}\right) \\ &= \frac{\pi L^2}{2}\left(\frac{D}{2}-\frac{D^2}{4L}\right) \end{aligned} \tag{2.44}$$

The total volume of one thin plate, with another close to itself, is described by

$$V_{ex}(D) = 2V'_{ex}(D=\infty) + 2V'_{ex}(D)\,. \tag{2.45}$$

This can be understood by looking at Figure 2.5. The side without a second wall stays unchanged, so that the contribution here still is $2V_{ex}(D=\infty)$. While the volume caused by the interface facing the other wall is diminished, but still has to be accounted twice because of the two ends of a rod. Now, by having an expression for the excluded volume of one wall at infinite separation, while overlapping with another depletion zone, the difference in excluded volume can be written down for each distance D.

$$\begin{aligned} V_{ex}(D) - V_{ex}(D=\infty) &= 2V'_{ex}(D) - 2V'_{ex}(D=\infty) \\ &= \pi L^2\left(\frac{D}{2}-\frac{D^2}{4L}-\frac{L}{4}\right) \end{aligned} \tag{2.46}$$

Knowing the volume difference (eq. 2.46), eq. 2.41 may be rewritten as follows:

$$W^{WW}_{dep}(D) = \rho k_B T \frac{\pi L^2}{4}\left(2D-\frac{D^2}{L}-L\right) \tag{2.47}$$

Generally the energy per surface area, γ_{dep}^{WW}, is given in literature. To get this eq. 2.47 is divided by the area maximally covered by a rod when rotating $\left(A = \frac{\pi L^2}{4}\right)$.

$$\gamma_{dep}^{WW}(D) = \frac{1}{2}\rho k_B T \left(2D - \frac{D^2}{L} - L\right) \tag{2.48}$$

For practical purposes the interaction energy between two plates is often not very useful. Fortunately, the result can be transfered to the case of depletion between a sphere and wall by use of the Derjaguin approximation (eq. 2.30).

$$\begin{aligned} W_{dep}^{SW}(h) &= -\pi R\rho k_B T \int_h^L \mathrm{d}h \left(2h - \frac{h^2}{L} - L\right) \\ &= -\pi R\rho k_B T \left(h^2 - \frac{h^3}{3L} - Lh + \frac{L^2}{3}\right) \\ &= -\frac{\pi}{3} RL^2 \rho k_B T \left(\frac{3h^2}{L^2} - \frac{h^3}{L^3} - \frac{3h}{L} + 1\right) \\ &= -\frac{\pi}{3} RL^2 \rho k_B T \left(1 - \frac{h}{L}\right)^3 \end{aligned} \tag{2.49}$$

The final expression may be rewritten to describe the sphere–wall depletion potential in dependence of the mass concentration $c = \frac{\rho M_{rod}}{N_A}$. Here N_A is Avogadro's number and M_{rod} is the molar mass of a rod.

$$\frac{W_{dep}^{SW}(h)}{k_B T} = -\frac{\pi}{3}\frac{cN_A}{M_{rod}} RL^2 \left(1 - \frac{h}{L}\right)^3 \tag{2.50}$$

2.1.4.2 Depletion caused by infinitely thin platelets

For platelets the derivation of the depletion potential would require extensive calculation. The principle though is the same as for the rods. Only the result for infinitely thin, circular discs of diameter, d, worked out by Piech and Waltz [62], shall be given here. The expression is more complicated than that for the rods, but still analytical. As for the rods, it is strictly valid only for monodisperse particles, which is a criterion virtually impossible to meet for real platelets. Later on it will be shown how to extend eq. 2.51 to apply also for polydisperse systems.

$$-\frac{W_{dep}^{SW}(h)}{kT} = \begin{cases} \frac{2}{3}\pi\rho_N R d^2 f(h,d) & \text{for } h \le d \\ 0 & \text{for } h > d \end{cases} \tag{2.51}$$

$$\rho_N = \frac{c_{plate} N_A}{M_{plate}}$$

$$f(h,d) = \left[\frac{3}{2}\frac{h}{d} \arcsin\frac{h}{d} - \frac{3}{4}\pi\frac{h}{d} + \left(1 + \frac{1}{2}\left(\frac{h}{d}\right)^2\right)\sqrt{1-\left(\frac{h}{d}\right)^2} \right]$$

here d is the diameter of the discs, R the radius of the probe sphere, c_{plate} the mass concentration of the platelets and M_{plate} their molar mass. In contrast to rods, platelets are a less effective depeltant, since the number density is lower at the same mass density and comparable size.

2.1.5 Total interaction energy between a sphere and a wall

When measuring the interaction energy of a sphere in front of a wall, the total potential or interaction energy is given as a superposition of the acting forces, which were discussed earlier. The full potential is therefore the sum of all those single contributions and may be written as

$$\begin{aligned} W_{tot}^{SW} &= W_{el}^{SW}(h) + W_{vdw}^{SW}(h) + W_{grav}(h) + W_{dep}^{SW}(h) \\ &= Be^{-\kappa h} - \frac{A_H R}{h} - \left[\frac{4\pi}{3}R^3(\rho_p - \rho_s)|\vec{g}| + \mathscr{R}_{sphere}\frac{\mathscr{P}}{c}\right]h + W_{dep}^{SW}(h). \end{aligned} \quad (2.52)$$

As long as the distances of the sphere from the wall is larger as 50 nm van der Waals forces do not have to be accounted for in detail [63]. For a bare sphere the interaction potential is described very well by a superposition of electrostatics and gravitation. When depletants are added, they always cause an attractive, range–limited potential. A description in a closed analytical form is only possible if the depletant has a distinct shape, such as spheres, rods or platelets.

2.2 Total internal reflection

Total reflection happens when an electromagnetic wave hits the interface between two media, which are generally transparent to the radiation, above a critical angle θ_c. Medium 1 has to have a higher refractive index, n_1, than medium 2, n_2, for total reflection to occur. Total reflection may be described as a form of refraction and thereby be explained by Snell's law (eq. 2.53).

$$n_1 \sin\theta_1 = n_2 \sin\theta_2 \quad (2.53)$$

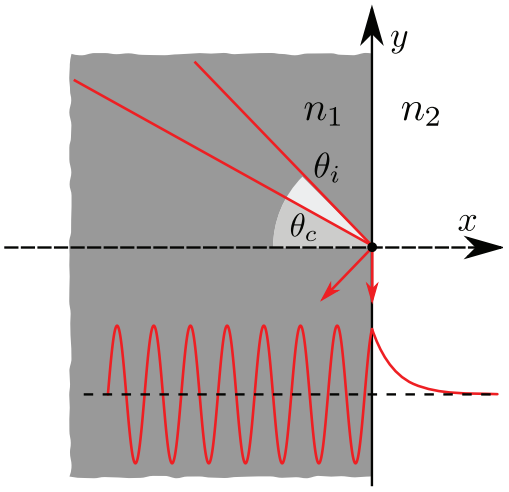

Figure 2.6: *The sketch shows two totally reflected light beams. The one, which comes in just under the critical angle, θ_c, propagates only along the interface. For higher angles the beams show typical specular reflection, where the angle of incident is equal to the angle of the reflected beam. Although the beams are reflected and do not propagate in the medium with the lower refractive index, n_2, there is still an exponentially decaying evanescent field. The propagating sinusoidal wave and the exponentially decaying field are depicted in the lower part of the figure.*

where θ_1 is the angle between surface normal and ray before refraction, respectively θ_2 after refraction. As a criterion for total reflection θ_2 has to be larger than $\pi/2$ respectively $\sin\theta_2$ has to become zero when $\theta_2 = \theta_c$.

$$\sin\theta_c = \frac{n2}{n1} \tag{2.54}$$

The general solution to the wave equation for an electromagnetic wave shall stay unchanged, so that a plane wave is sufficient to describe the reflection. Above the critical angle the wave is no longer refracted, but reflected. Yet the Maxwell equations do not allow an abrupt end of the wave field at the interface, so that the electromagnetic field reaches into medium 2 in form of an evanescent wave. As pointed out, the field should still be described by a plane wave, which is given by

$$\vec{E}(\vec{r},t) = \vec{E}_0 e^{-i\left(\omega t - \vec{k}\cdot\vec{r}\right)} \tag{2.55}$$

where $\vec{k} = 2\pi n/\lambda \cdot \hat{e}_k$ is the so called wave vector and ω the angular frequency of the light wave. Here a two dimensional scenario will be analysed, in which $\vec{k}$ has only two components, given by $\vec{k}_i = \left|\vec{k}\right| \cos\theta_i \hat{e}_x + \left|\vec{k}\right| \sin\theta_i \hat{e}_y$. In order to find the wave vector after traversing into the optically less dense medium, Snell's law is used.

$$\cos\theta_2 = \sqrt{\left(1-\sin^2\theta_2\right)} = \sqrt{\left(1-\left(\frac{n_1}{n_2}\right)^2 \sin^2\theta_1\right)} = iZ \tag{2.56}$$

If the angle of incident is higher than the critical angle, the square root assumes an imaginary value. Now it is possible to write down the wave function in medium 2.

$$\vec{E}_2(\vec{r},t) = \vec{E}_{02}e^{-i\omega t}e^{ik(\cos\theta_2 x+\sin\theta_2 y)} = \vec{E}_{02}e^{-i\omega t}e^{-kZx+ik\frac{n_1}{n_2}\sin\theta_1 y} \tag{2.57}$$

Since electrical fields are hard to measure the field intensity is calculated.

$$I_2(x) = \left|\vec{E}_2(x,t)\right|^2 = I_{02}e^{-2kZx} = I_{02}e^{-\beta x} \tag{2.58}$$

Here, β, which is called the inverse penetration depth, can be identified.

$$\beta = 2kZ = \frac{4\pi n_2}{\lambda_0}\sqrt{\left(\left(\frac{n_1}{n_2}\right)^2\sin^2\theta_1 - 1\right)} = \frac{4\pi}{\lambda_0}\sqrt{\left({n_1}^2\sin^2\theta_1 - {n_2}^2\right)} \tag{2.59}$$

The penetration depth, β^{-1}, is the distance where the field intensity has dropped to $1/e$ of its initial value. This simple derivation shows that the light field no longer propagates in medium 2, but decays exponentially as an evanescent field when the light beam is shone onto the interface at an angle, higher than the critical angle (see Figure 2.6).

3 Experimental methods

This chapter will line out the fundamentals of the experimental methods. Starting with a description and explanation of the total internal reflection microscopy (TIRM) setup with all its components. Introducing the basic measurement principle, showing how evanescent illumination is utilized to gather information about sphere–wall interaction energies and giving a sketch of the data analysis and data handling. Further presenting modifications made in order to measure in a shear field and offer further automation.

Sources of measurement errors will be discussed and analysed, pointing out that it is rather difficult to find a good estimate for the prevalent measurement errors, since the measurement method relies on the measurement of probability distributions and not mean values. Lastly, sample preparation and sample properties are discussed.

3.1 TIRM and data analysis

Total internal reflection microscopy (TIRM) is conceptually a simple microscopy technique employing a special kind of illumination. It has been pioneered by Prieve et al. [26] and is one of the most sensitive ways to measure sphere–wall interaction forces. The force resolution is within the fN regime. Instead of looking at particles in bright field or any other kind of established illumination, an evanescent wave (see section 2.2) is used. In contrast to standard microscopy methods, where one is interested in the shape or structure of objects, with TIRM scattering intensities are observed. Due to the evanescent nature of the illumination only particles very close to the surface (within a few hundred nano metres) will scatter light from the evanescent wave and therefore be visible. Different from the evanescent wave, used to illuminate the particle, the light scattered by the particle will propagate through the solution, creating a bright scattering point in front of a dark background. The particles' scattering

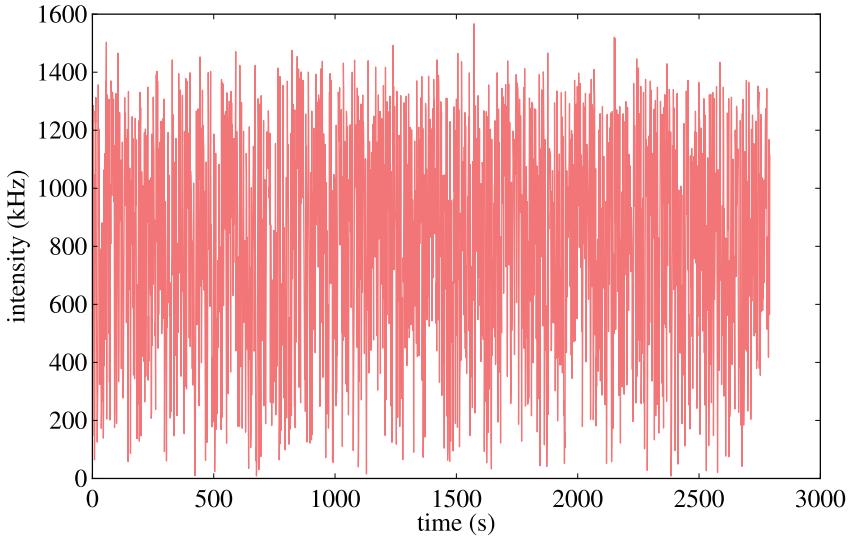

Figure 3.1: *Typical intensity trace recorded by a PMT and tweezers trapping a R = 1.5* µm *polystyrene particle. The chosen sampling time is 2 ms with a total of 1 400 000 data points.*

properties can be described by modified version of Mie scattering theory [64, 65]. In the evanescent illumination field the scattered intensity of a particle, $I^S(h)$, decays exponentially with increasing distance to the glass–liquid interface, provided that the evanescent field decay can be described by an exponential [66–68] (see section 3.2.1).

$$I^S \propto I^{ill} \tag{3.1}$$

An expression for the intensity of the evanescent field has already been derived in section 2.2. In consequence, the scattered intensity can be written, according to eq. 2.58 and 3.1, as

$$I^S(h) = I_0^S e^{-\beta h} \tag{3.2}$$

where h is the distance from the wall to the sphere surface and I_0^S is the intensity of a particle in direct contact with the wall. In other words, the intensity of a particle, which sticks irreversibly to the wall. Evidently, eq. 3.2 is based on the assumption that the properties of the probe particle do not change when it comes into contact with the wall. Namely, that it does not deform and that there will be no coupling of dipole moments of sphere and wall, creating averaged dielectric properties of the particle.

When doing a standard TIRM experiment, the intensity scattered by a single particle, undergoing thermally induced motion normal to the wall and thereby sampling randomly all

accessible energy states, expressed by the probability to attain a certain height, is measured over a period of time. Usually a total of 500 000 intensities are recorded with a sampling rate of generally 200 Hz or 500 Hz (see Figure 3.1) . During a measurement the particles' lateral diffusion is inhibited by the use of two dimensional optical tweezers (see sections 2.1.1 and 3.2.3). The gathered intensities can be transfered to height information if I_0^S is known.

$$h = \frac{1}{\beta} \ln \frac{I_0^S}{I^S} \tag{3.3}$$

Information about the interaction energy can be gained by exploiting the fact that under equilibrium conditions the heights, and for that matter the intensities, have to follow a probability distribution. That means that a certain elevation corresponds to a specific energy or state of the probe particle. By virtue of an inversion of the probability distribution, the interaction energy may be inferred by simply counting intensities. It has to be noted that the terms interaction energy and interaction potential are often used synonymously, which is slightly misleading. In thermal equilibrium one can utilize the fact that the particles perform their motion according to Boltzmann statistics. The probability density, $p(h)$, of finding a particle at an elevation, h, can be written as,

$$p(h) = C \exp\left(-\frac{W^{SW}(h)}{k_B T}\right) \tag{3.4}$$

where $W^{SW}(h)$ is the sphere–wall interaction energy and C a normalization factor. Following the analysis of Prieve [26], it is assumed that the probability of observing a given intensity is equal to the probability of finding a particle at the corresponding elevation, i. e. $p(h)dh = p(I^S)dI^S$. Together with eq. (3.2) this leads to,

$$p(h) = -\beta\, p(I^S) I^S(h). \tag{3.5}$$

The probability density, $p(I^S)$, is determined experimentally as the histogram of the intensity trace, assuming that the histogram (see Figure 3.2) of measured intensities, $N(I^S)$, converges to $p(I^S)$ for small enough bins and a sufficiently large number of events. Dividing the resulting probability density of heights $p(h)$ by $p(h_0)$ one obtains,

$$\Delta W^{SW}(h) = \ln\left(\frac{N_{max} I^S_{max}}{N(I^S) I^S}\right). \tag{3.6}$$

Here N_{max} is the number of counts in the histogram maximum, I^S_{max} is the corresponding intensity, $\Delta W^{SW}(h) = W^{SW}(h) - W^{SW}(h_0)$ and $W^{SW}(h_0)$ is an arbitrarily defined value of the

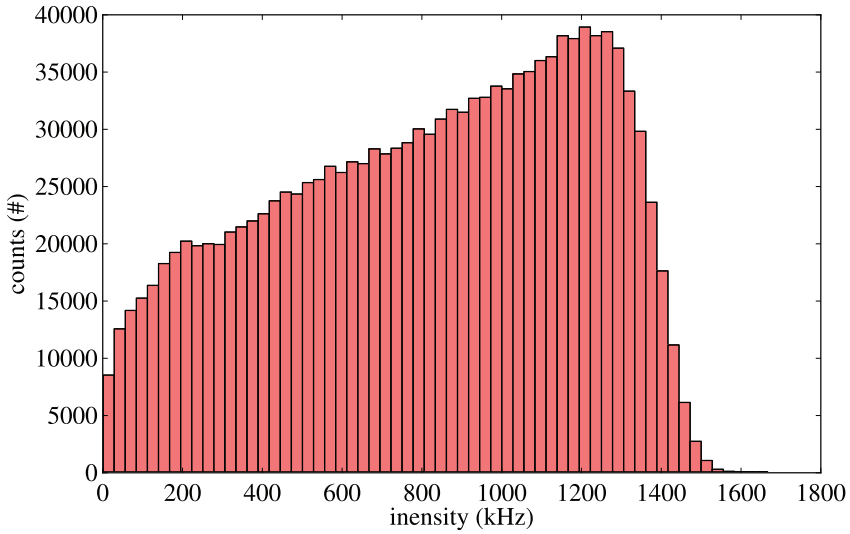

Figure 3.2: *The recorded intensity trace is histogramized yielding a distinct distribution. In this particular case the number of bins is set to n_{bin} = 50.*

potential minimum, which is located at h_0. Up to this point no specification of the sphere–wall potential's functional form has been made. The only constraint of the method is that the measured probe particles have to be in thermodynamic equilibrium. A point, which has to be emphasized is that no absolute energies are accessible without defining a point of reference. In the plots usually W^{SW} instead of ΔW^{SW} is written. A typical potential of a polystyrene sphere with a diameter of D = 3 μm is shown in Figure 3.3. The potential is composed of a superposition of an electrostatic potential and gravitational plus light contributions.

3.2 Setup

The TIR microscope (see Figure 3.4, components referenced in the text) is self–built from standard microscopy components (Olympus), which are mounted on a X-95 rail system (Linos). It consists of an infinity corrected 40x Olympus SLCPlanFl objective (6) with a focal length of f = 6.5 – 8.3 mm and a numerical aperture, NA=0.55, followed by a dichroic mirror (7) to couple in the 532 nm tweezers laser (Coherent Verdi V2) (4). A 50/50 beam splitter (8) equally distributes the light from the sample cell to a camera (Photometrics Cascade 1 K) (16) and a photomultiplier tube (PMT) (Hamamatsu H7421-40) (17). In front of the PMT the parallel light rays from the objective are focussed on a pinhole (11) of 1 mm diameter by a tube lens (13) with a focal length f = 150 mm. The pinhole is used as spatial filter. After

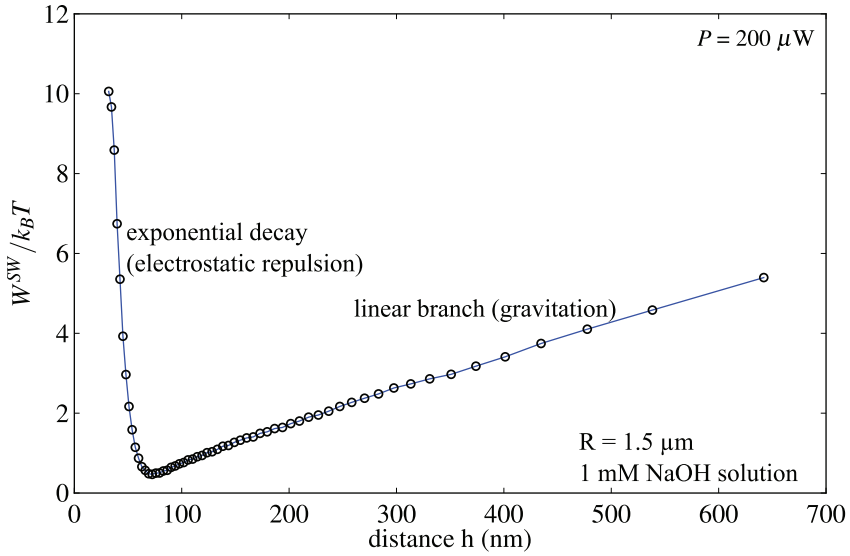

Figure 3.3: *Following the presented analysis, the histogram can be converted into a potential. The data was taken from a D = 3* µm *polystyrene sphere in 1 mM NaOH solution, trapped at a tweezering power of 200 µW. The potential comprises electrostatic repulsion plus an attractive, linear branch caused by gravitation and light pressure. The full line is just a guide to the eye.*

passing the pinhole a beam expander (12) widens the beam to supply homogeneous illumination of the photo cathode. In the light path to camera and the PMT band pass filters (9),(15) (λ_{pass} = 633 nm) help to increase the signal to noise ratio ($S/N > 100$). These filters can be exchanged depending on the illumination wavelength and if the measurement will be performed by recording scattered or fluorescent light. The sample cell is a quartz glass flow cell (QS137) (5) from Hellma with a volume of 520 µL or 26 µL . Since it is completely made of glass, it is very inert and contaminations of the cell are unlikely. For exchanging liquids during a measurement series the cell is connected to a glass syringe equipped with a valve by highly chemically resistive tubing (Tygon 2075 from Saint Gobain). The cell itself is mounted in a copper holder, which may be connected to a thermostat to keep the cell at a desired, constant temperature. The holder is moved by two linear micro meter tables (coherent) in order to find a suitable particle inside the cell.

The illumination source (1) is a 15 mW HeNe laser (λ_{ill} = 632.8 nm, noise RMS < 0.20 %) or a 10 mW diode laser (λ_{ill} = 440 nm, RMS < 0.5 %) depending on the mode of operation (scattering/fluorescence). The beam shape is not altered before hitting the interface, so a stretched Gaussian illumination spot is expected at the reflecting interface. By use of a polar-

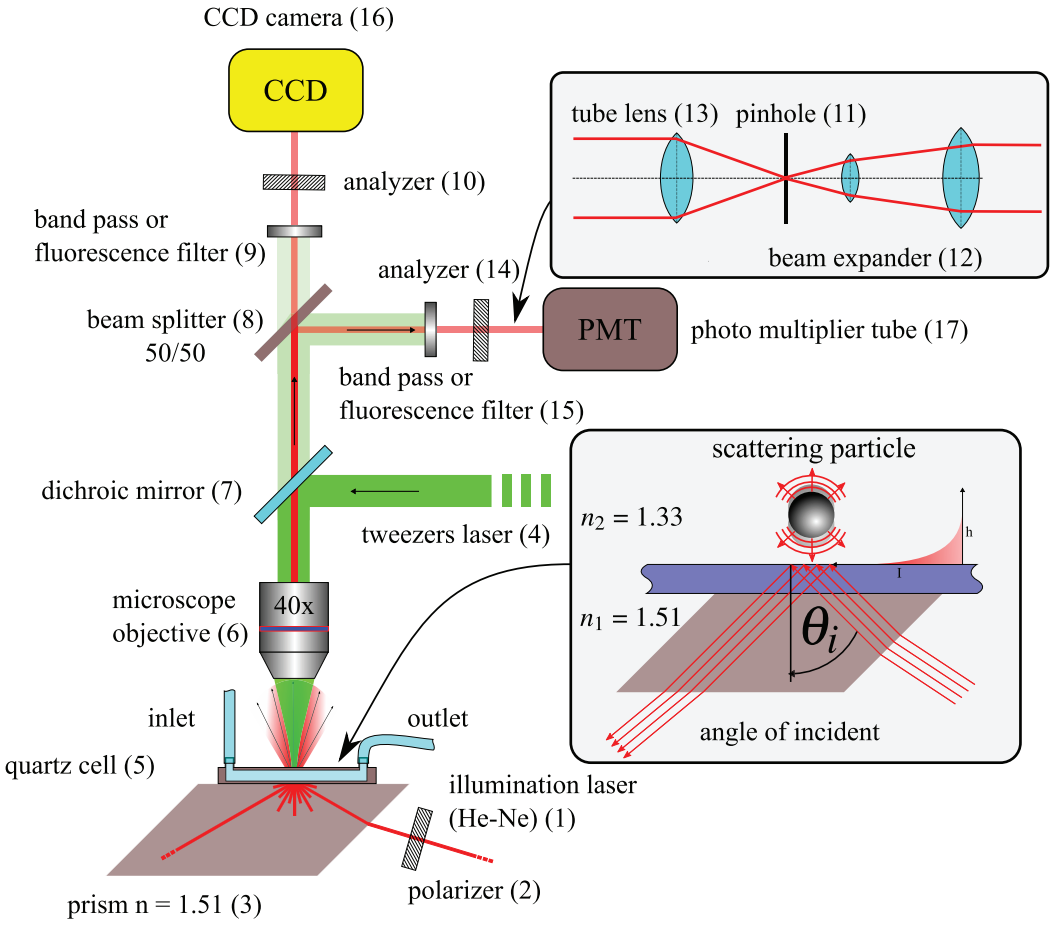

Figure 3.4: *Schematic picture of the TIRM/TIRF setup. The components are annotated and described in the text. Cell and illumination principle are highlighted, as is the beam expander used to improve the signal quality by helping to illuminate a larger portion of the PMT cathode. Particles with a distance of a few hundred nano meters from the surface are able to extract energy from the evanescent wave and reemit it in form of a scattered light wave (or as fluorescent light). This wave propagates in contrast to the evanescent field and is collected by the microscope objective. The intensity of the scattered light has an exponential dependence on the particle–wall distance.*

izer (2) it is assured that the laser light is p–polarized with respect to the glass–liquid interface. As an additional measure, analyzers (10), (14) are placed in front of the detectors, so that only p–polarized light can be detected. The lasers are mounted on a goniometer, which is driven by a linear stepper motor. The linear motion of the stepping motor is transfered into an angular motion by an excenter. The goniometer allows the angle of incidence, θ_i, to be set with high accuracy and reproducibility. A prism (3) of BK7 glass from Edmond optics is attached to the cell to enable total reflection conditions and the creation of an evanescent wave. A thin film of immersion oil index matches possible gaps between prism and cell. The angle, θ_i, cannot be set directly due to the shape of the prism, which causes an refraction at the prism air interface. The deviation is corrected by a simple geometrical construction.

3.2.1 Polarized illumination

Fixing the polarization to a p–polarized state with respect to the reflecting surface ensures that the reflectivity of the interface is minimal and therefore the illumination profile is really given by an exponentially decaying evanescent wave. In order to exclude light, of which the polarization might have been shifted in the light path, an analyzer in front of each detector is used. The Fresnel coefficient for reflection of p–polarized light is considerably smaller than that of s–polarized light. Therefore, polarizing helps to prevent reflections at the interface originating from scattered light. The reflections might result in interferences between scattered light of a particle and reflected light from the surface. Essentially, standing waves would form between the probing particle and the wall, giving rise to constructive or destructive interference with regard to the perpendicular particle position. Such an effect would then show as an undulation in the potential, which would distort the real potential shape [66]. With p–polarized light and the used penetrations depths it is unlikely for interference effects to play a role [69].

When doing fluorescent measurements, interferences are also less likely to have an influence, because fluorescence does not emit coherent light. Nevertheless, the particle scatters light at the same time, so that there may still be an influence on the illumination profile and through this on the fluorescence intensity, which is detected.

3.2.2 Detectors

In standard TIRM setups the acquisition of intensity traces is realized with the PMT (photo multiplier tube). In the current setup the device produces TTL pulses according to the number of photons registered in a given time interval (sampling rate), so that an intensity is measured in form of a photon rate. The TTL pulses are recored by a digital counter card (National

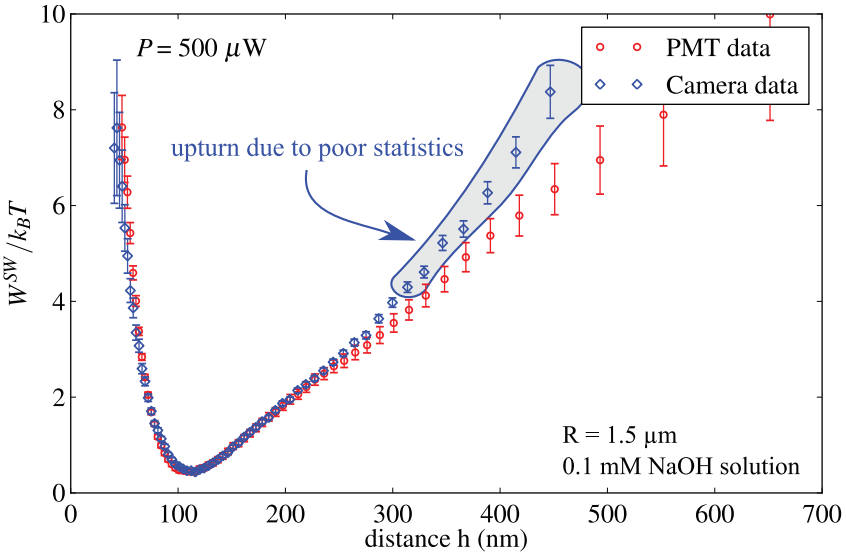

Figure 3.5: *The interaction potential of a R = 1.5* μm *polystyrene bead in 10^{-4} M NaOH is measured simultaneously with the CCD–camera and the PMT. It is obvious that the potentials are effectively identical. The shown errors are underestimated at higher distances, which will be discussed in section 3.3. Even more, the error estimation is not entirely valid for the measurement done with the CCD (the errors are underestimated).*

Instruments NI-6602) and then processed by self made acquisition software. The software allows to automate whole measurement series. With the employed PMT and the counter card sampling rates up to 100 000 Hz can be reached. One drawback is that only an integrated intensity is measured, which means that multiple particles present in the field of view will result in a false potential. As pointed out, the problem is alleviated by the use of a pinhole as spatial filter. Due to the spatial filtering, the PMT always requires optical tweezers to limit the particle movement. This imposes a lot of restrictions, i.e. only one particle can be measured at a time and no information about lateral diffusion can be gained. In order to remove these restrictions, a highly sensitive EM-gain CCD (the EM-layer allows pre amplification of the signals) is used in parallel to measure intensity fluctuations. The filter in front of the camera can easily be removed and reinserted without disturbing the measurement process. In this way it is possible to use the camera for adjustments and measurements without the need of changing the setup. Potential measurements done with the camera agree very well with those measured using the PMT (see Figure 3.5). The figure shows a slight upturn at higher distances in the energy values for the measurement made with the CCD–camera. This is an effect of poorer statistics, which is a result of the main drawback when using the camera – the lack of

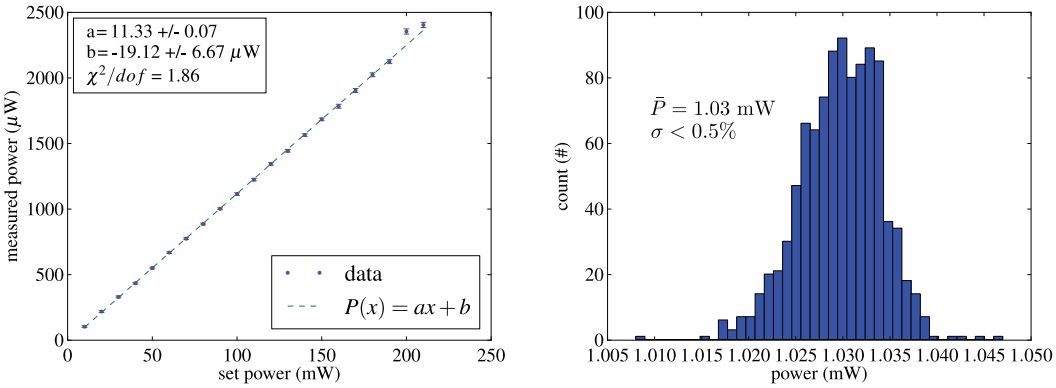

Figure 3.6: *The power of the optical tweezers is measured after leaving the objective with a simple power meter. Of course this doesn't yield absolute power values due to various losses, but delivers an estimate for the power of the tweezers. The stability of the tweezers is determined by a long term measurement (more than 1 h) of the power. The power values are histogramized showing a Gaussian distribution as expected. Mean value and standard deviation are given.*

acquisition speed. The data was taken simultaneously with the camera and the PMT, while trapping only one particle with the optical tweezers. The camera can take pictures with a minimum illumination time of 2 ms, but the readout time decreases the sampling rate to about 20 Hz. For the comparison an illumination time of 10 ms is chosen. The camera's lack of speed is made up for by the possibility of doing ensemble measurements (see section 3.2.5), i.e. measurements with more than one particle in the field of view at the same time. For the sake of clarity and to make the comparison as convincing as possible, the potentials shown are based on data taken only from one particle, instead from multiple particles simultaneously. A general point concerning the detectors is that overexposure has to be avoided. In case of the PMT this leads to non linear amplification of the signal. And in the case of the CCD-camera the pixels will give false values if the charge accumulation becomes to high (overfull electron wells). In order to always operate in the optimal dynamic range of the camera or PMT, neutral density filters can be placed in front of the illumination laser to attenuate the intensity. For the camera also the illumination time can be decreased or the EM-gain turned off.

3.2.3 Optical tweezers

The realization of the optical tweezers shall be briefly discussed, since it will be later important to understand as to why they cannot be used when measuring under shear flow. The physical principle of optical tweezers has already been discussed in section 2.1.1. The laser light neces-

sary for the optical tweezers is produced by a Coherent Verdi V2 frequency doubled solid state Nd:Yag laser (λ = 532 nm). For this particular laser the available output powers tend to be much higher than needed to operate optical tweezers. To overcome this problem the laser beam is attenuated with a polarizer by exploiting Malus' law (note the that the laser is pre–polarized) prior to being used. After having been attenuated the laser is coupled into a high power, polarisation maintaining mono mode fiber (OZ optics: QPMJ-3AF3A-488-2.5/125-3AS-1), which leads to the setup. Once the beam exits the fiber through a second fiber coupler, which reconstitutes a Gaussian beam, it is slightly widened to overfill the back–aperture of the objective. Power stability of the tweezer is crucial, since instabilities have a direct influence on a potential measurement. Therefore, the power behind the objective is measured once, after setting up the tweezers as a check with a power meter. Also the beam shape is checked for any deviation from a Gaussian profile by looking at the reflection respectively the interference rings caused by the reflected laser light in the camera picture. Admittedly, this is a rather crude way to make sure ideal conditions are provided. First of all it is impossible to measure the absolute power of the tweezers with the power meter alone, due to reflections and losses. But it is more than sufficient to describe the change in power for the selected output powers or check the power stability. Moreover, the performed checks are good enough for the rather simple type of tweezers needed to hold a large colloidal particle. Still possible misalignment of the focus of the tweezers has to be corrected. The position and shape of the tweezers' focus point can be adjusted by two linear micro meter tables, on which the fiber coupler, used to couple out the light is mounted. Tilting this fiber coupler offers a further way to adjust the alignment of the optical tweezers. The position of the laser spot in the field of view has to coincide with the pinhole in front of the PMT to enable measurements. Power stability and power calibration of the tweezers laser are performed after alignment and some exemplary results are shown in Figure 3.6. The power stability is better than 0.5 % and the coupling through the fiber retains the linear power dependence perfectly.

Power output is controlled by the measurement software via a RS232 link to the laser. This has the advantage of being able to make scripted measurements, removing the requirement of manually setting the output power.

If everything is set up in the correct way, the prediction of a linear potential contribution should be fulfilled. Furthermore, the effective weight force should increase linearly with the applied light power. As can be seen in Figure 3.7 the prediction is met. Indeed the weight increases linearly for the shown measurement series. While looking at the weight force over power dependency, one might be tempted to determine the real weight of the probe particle by finding the intersection with the ordinate. But the found particle weight force of 12 fN is

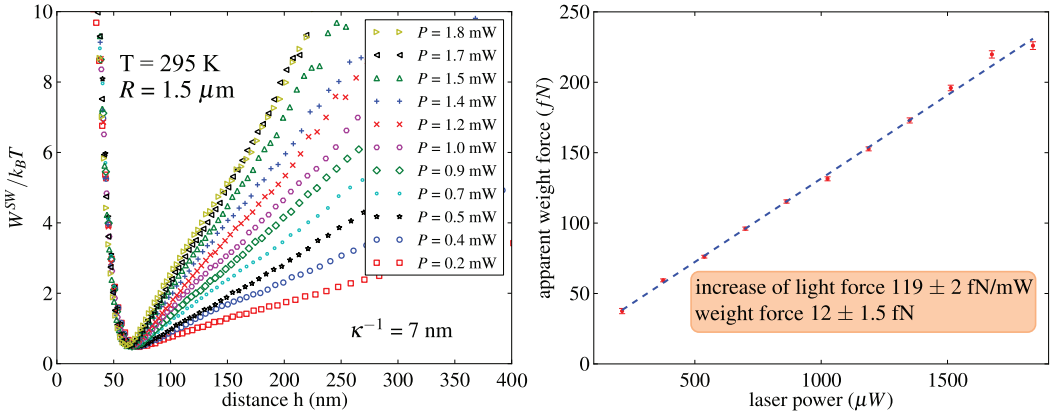

Figure 3.7: *The interaction energy of $R = 1.5$ µm probe sphere with a glass wall in a 1 mmol/l NaOH solution at room temperature is measured for various intensities of the tweezers (left picture). With increasing power the particle seems to become heavier due to radiation pressure. The weight force increases linearly with the applied power (right picture). In principle it is possible to determine the real weight of the particle by finding the intersection with the ordinate.*

almost twice as high as expected (7 fN for a $R = 1.5$ µm polystyrene particle with a buoyancy corrected mass density $\rho_{eff} = 55$ kg/m^3). The mismatch is due to the high uncertainty when determining an intersection. While the slope of the fit has a realistic error the error on the intersection is underestimated. Overall the stability of the measured potentials is very good with the tweezers turned on. Keeping the particle in one place enables the use of a spatial filter and suppresses lateral diffusion. Although spatial filtering and tweezering will have to be abandoned in later measurements, the tweezers are a good tool when it comes to precise single particle measurements (see section 4.2). When discussing measurement under flow, it will be shown that having optical tweezers is only advantageous if no shear field is applied.

3.2.4 Realization of flow

One of the goals of this work was to integrate the ability to generate shear fields into the TIRM setup. Most commonly shear is realised by using mechanical shear cells of various geometries [70]. While the shear cell approach is well suited for rheological experiments, it tends to be not precise enough when doing very sensitive force measurements such as TIRM experiments. To achieve maximum accuracy and precision a very simple approach is chosen. The general idea is to use earth's gravitational field to generate a pressure difference between in– and outlet of a flow cell. For moderate flow rates a laminar flow inside a flow cell with a

defined geometry can be created. In the setup a glass flow cell is connected to a reservoir by highly chemically resistive tubes. This reservoir is a syringe or burette filled with the sample solution. They are also equipped with a valve to shut down the flow completely. If the valve is opened the suspension will flow through the cell creating the desired flow field. At the end of the tubes the flow is regulated by an electronic flow mass controller (Bronkhorst mini Cori Flow) (see Figure 3.8).

The device is a combination of Coriolis flow meter, measuring the flow by looking at a torque created due to Coriolis forces with a torsion balance, and an electronic valve. The method of measuring the flow is insensitive to changes in viscosity or turbidity. The only properties, which have to be known are the mass density of the liquid and its temperature. The device is calibrated to the density of water (at 20°C), which is close enough to all suspensions used in the course of this work. But even correcting for solvents with a mass density different to that of water is a trivial tasks. The inner electronic and logic of the device stabilizes the flow with a magnetic needle valve. The flow through the flow meter can be monitored by a computer connected to the device. The computer is also utilized for setting the flow rate and checking if the flow has stabilized, which might take up to one minute. Using a computer controlled valve allows the measurements to be further automated.

The current calibration of the flow controller offers to vary the flow rate from 0.02 g/min to 2 g/min. As long as the flow inside the cell is laminar, the flow profile has a parabolic shape and resembles a Poisseuille flow. The shear gradient close to the wall is approximately linear and the shear rate thereby constant. Of course probe particles, which have a diameter of several microns perturb the flow field, but it is expected that caused variations in the flow profile are small and can be neglected. With this assumption the shear rate may be calculated. Experimentally the mass flow rate is always given by the flow meter and the geometry of the cell is known.

A one dimensional Poisseuille flow [71] is given by

$$v(z) = \frac{1}{2\eta} \overbrace{\frac{\mathrm{d}p}{\mathrm{d}x}}^{\Delta p/L} \left(\frac{d^2}{4} - z^2 \right) \tag{3.7}$$

where $v(z)$ is the flow velocity, z the distance from the cell center to the wall, Δp the pressure difference between cell's in– and outlet, L the distance between in– and outlet, d the cell thickness and η the zero shear viscosity of the liquid. With

$$v(z=0) = v_0 = \frac{1}{8\eta L} \Delta p d^2 \tag{3.8}$$

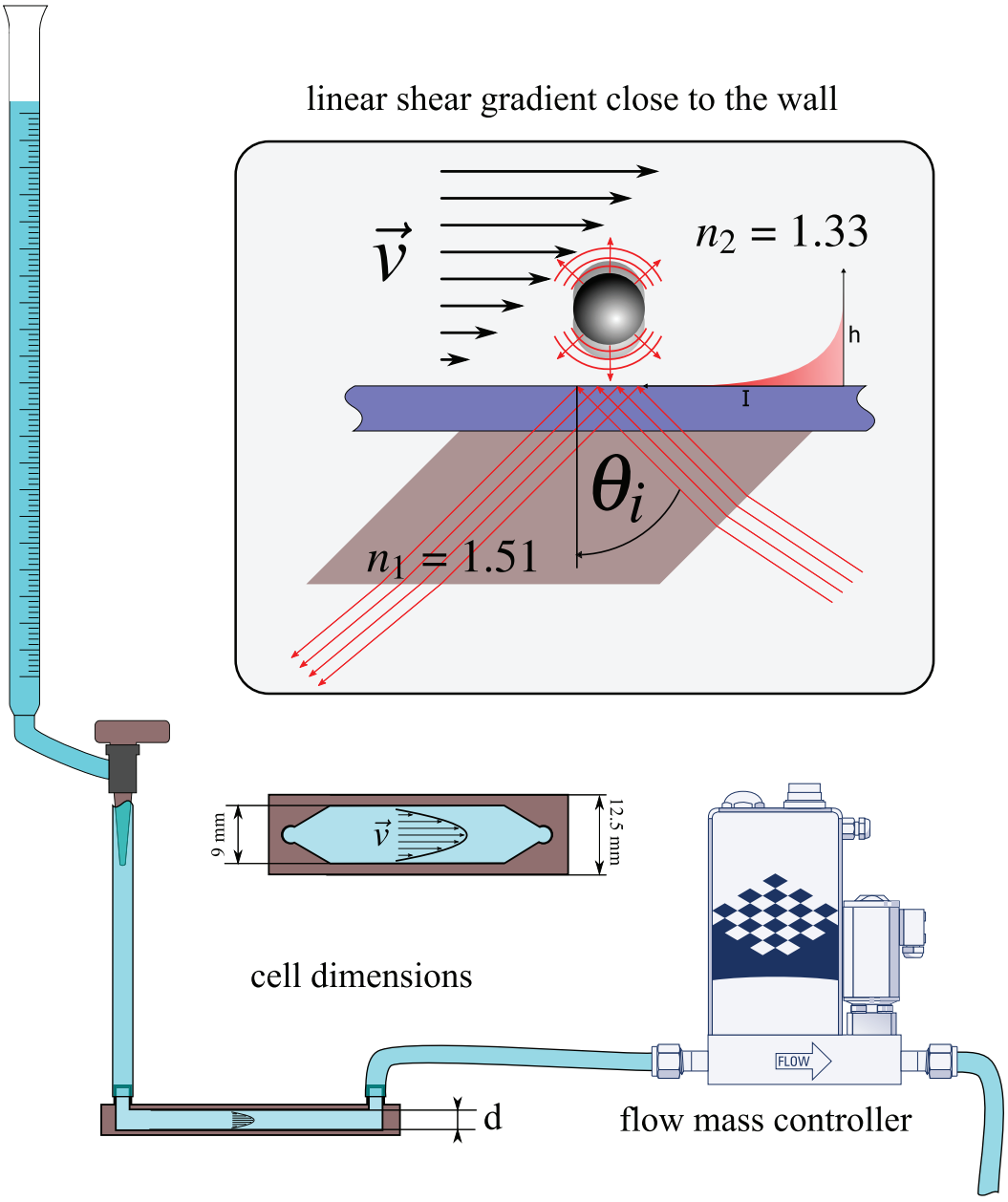

Figure 3.8: *A laminar flow is produced by using the gravitational field of the earth. The reservoir with the sample solution is placed at a sufficiently higher point (about 1 m) to create the necessary pressure. The reservoir is connected to a flow cell with a thickness d = 0.1 mm or 2 mm depending on the performed measurement. The shear rate scales approximately with* $1/d^2$ *in the vicinity of the wall. The mass flow is measured by a Coriolis flow mass controller, which regulates the flow with an electronic needle valve. Inside the cell, close to the wall, the created shear rate will be linear.*

eq. 3.7 can be simplified to

$$v(x) = v_0 \left(1 - \frac{4z^2}{d^2}\right). \tag{3.9}$$

From the experiments only the mass flow, Φ_M, through the cell is known, which can readily be connected to the velocity in the cell by

$$\Phi_M = \rho \int_A v(z) \mathrm{d}A = 2\rho v_0 \int_0^b \int_0^{d/2} \left(1 - \frac{4z^2}{d^2}\right) \mathrm{d}x\mathrm{d}z = \frac{2}{3} bd\rho v_0 = \frac{2}{3} A\rho v_0 \tag{3.10}$$

where b is the width of a cell (9 mm) and ρ the mass density of the liquid. Now the shear rate, $\dot{\gamma}$, inside the cell in dependence of the distance from the wall can be derived.

$$\dot{\gamma} = \frac{\mathrm{d}v(z)}{\mathrm{d}z} = -v_0 \frac{8z}{d^2} = -8v_0 \left(\frac{d/2 - h}{d^2}\right) \tag{3.11}$$

Of course this is only an approximation, because the flow profile changes not only with the distance to the interface, but also with the lateral position inside the cell. Under the assumption that the field of view is sufficiently far away from the cell walls, this effect should be small and negligible. Furthermore, the particle is not considered and an undisturbed flow field is assumed. But as to how the particle interferes with the profile is hard to determine.

Nevertheless, perturbation of the flow field by the probe particles is inevitable. Even with standard shear cells this would be an issue. Compared to the shear cells, generating a shear gradient in a flow cell by virtue of gravitation offers an easy, stable and precise way to change the shear rate close to the wall. Using different cells opens the possibility to change the accessible shear rate over a very wide range, while the setup has no sensitive moving, mechanical parts.

3.2.5 Ensemble measurements

As already discussed (see section 3.2.2), the CCD camera allows to observe multiple particles at the same time. More than that, it opens the possibility to measure at higher flow rates than with tweezers. Using the optical tweezers, there is a limit to the force caused by a shear field, which is allowed to act laterally on the particle before it is literally pushed out of the trap. Measuring many particles simultaneously over a period of time will be called an "ensemble measurement" of particles (this is different from the term used for thermodynamic ensembles). To infer the sphere–wall interaction potential, the intensity traces of all particles in the field of view are needed. The camera can record a movie respectively a series of images. Yet this only yields images with the intensity of the particles encoded in the pixel's contrast values. In order

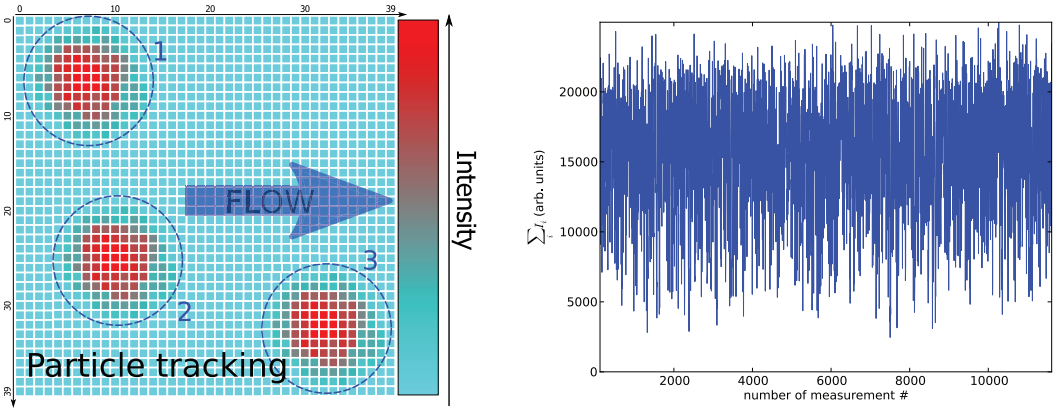

Figure 3.9: *When measuring with the camera particle tracking is performed to acquire the individual intensity traces of the particles. To process the data and convert them into an interaction potential, the single particle intensity traces are summed up to give an effective single particle trace.*

to gain information about the single particles, a way to discriminate between the individual particles and convert the contrast values to some meaningful pseudo intensity has to be found. Furthermore, to analyze the data gathered by TIRM or TIRF, it is necessary to define an effective intensity trace. Treating a number of particles as effectively one particle implies that the trace over time of the scattering intensity of one particle and the sum of the intensity traces of many individual particles over a defined period of time are interchangeable. Essentially, this assumes that all particles are identical or at least very similar in their behaviour, undergoing uncorrelated movement.

For the purpose of calculating this effective single particle intensity trace and discriminating between single particles in the pictures, all particles, i, in the field of view are tracked with a particle tracking algorithm developed by John Crocker and David Grier [72] (see Figure 3.9). The code not only yields the position on the CCD–chip, but also the intensity at any given time. To compute an effective intensity trace the recorded particle traces are put through an exclusion filter to remove false hits by checking the mean value and the variance of each individual intensity trace. A selection window for the filter based on the most likely average mean intensity of an individual trace, observed during an experiment is defined, allowing a variation of 5 percent. The filtering helps to exclude particle close to each other or traces distorted by particles stacked onto each other. Once the filter process is performed, all selected intensity traces are summed up, $I_{tot} = \sum_i I_i$, to make up an effective single particle intensity trace. Combining a number of particles into one effective particle, makes it possible to use the standard method, described in section 3.1 to calculate the potential. Of course this method

represents a form of averaging over many particles. Averaging leads to a higher uncertainty when measuring a potential. In spite of that, the filtering ensures a reproducible potential measurement. Naturally, one limitation of this method is that the polydispersity of probing particles has to be low. Another point, which has to be noted, is that the illumination is not completely homogeneous, but describes a stretched Gaussian intensity distribution on the liquid–glass interface.

In spite of alle these points, it turns out that potential measurements with many particles are feasible. Potentials do not change when a high number of particles is observed (see section 4.2.4). The probe particles should of course be as monodisperse in their properties as possible. Otherwise only a fraction of particles would enter the analysis due to the filtering. For flow measurements the number of particles, which has to be tacked is quite high (up to a few thousand particles). The solution flows through the cell, particles enter the field of view, their trajectory together with their intensity fluctuation are recorded by the camera and the data is processed in the described way.

Nevertheless, when doing measurements under flow, it is not immediately obvious that the inversion of probability distribution, used to infer the sphere–wall interaction potential still works. Strictly speaking, particles in a shear gradient respectively in a flow field are no longer in a thermal equilibrium. Yet a free particle close to a wall does not experience any force normal to a wall if a flow field is applied. The argument for this reasoning works as follows: if the particle experienced a normal force, it would describe a trajectory $\Delta\vec{r} = \vec{r}(t_0+t) - \vec{r}(t_0)$, which is influenced by the component normal to the wall. When inverting the direction of time, meaning going from t to t_0, the particle should return to its origin $\vec{r}(t_0)$. But the acting normal force would point in the same direction due to symmetry reasons in both time directions, so that the particle would not return to its original position. This is a violation of time inversion, showing that there cannot be any normal force for a free particle in a flow field. Without a normal force the probability distribution in z direction is not affected by the flow field. Essentially, leaving the particle in thermal equilibrium when only looking at the motion perpendicular to the wall. With this argument the standard method to calculate a potential is still valid and can be applied to intensity traces acquired with a shear gradient applied to the probe particles.

3.2.6 TIRF measurements

TIRF (total internal reflection fluorescence microscopy) is only a minor modification modification to the standard TIRM method. Instead of normal polystyrene beads, fluorescent ones are used. The illumination source (1) is exchanged with a laser of suitable wavelength, here

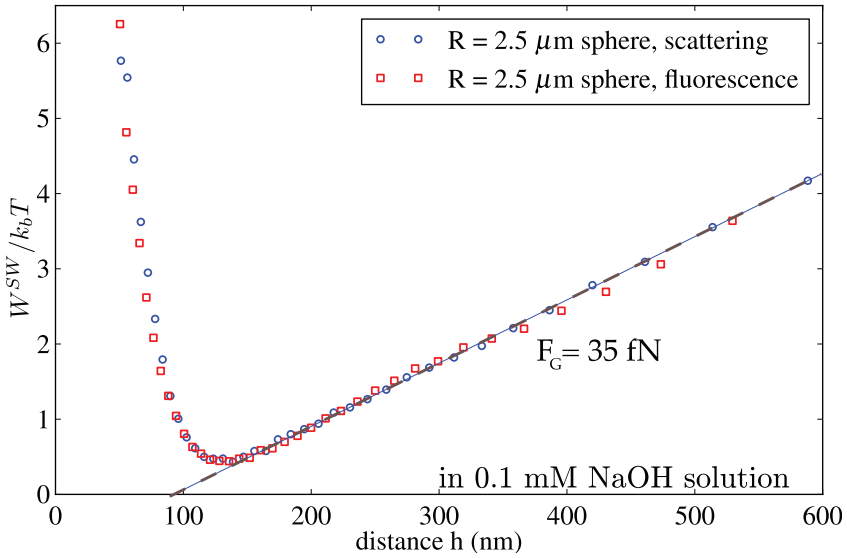

Figure 3.10: *Interaction potentials of green fluorescing R = 2.5* µm *polystyrene beads in 10^{-4} M NaOH solution. The measurements are done successively with the camera by changing the used filter. In case of the scattering measurement the fluorescence light is blocked by using a band filter only allowing the laser wavelength to pass. The two potentials agree very well. No sign of bleaching or saturation can be seen.*

a 440 nm diode laser (see section 3.2). In addition, the band pass filter (14) (λ_{pass} = 633 nm) is exchanged with an edge pass filter (chroma E515LPv2, λ_{pass} > 515 nm) blocking the excitation wavelength. For detection the camera has to be used, because the optical tweezering would lead to bleaching of the particles. In Figure 3.10 a comparison for a single R = 2.5 µm green fluorescing polystyrene sphere (thermo scientific, G0500), between fluorescence and scattering is given. It is obvious that the two measured potentials are virtually identical. There are no signs of bleaching, which would manifest in a deformation of the potential. A crucial requirement is that the fluorophore should never be completely saturated, because then the exponential distance dependency of the intensity signal would no longer be valid. The data shown in the example potentials are successively measured on one and the same sphere. Here, only one particle is observed to yield a better comparability, but the observation of multiple particles at the same time is possible as well. Measuring fluorescently offers the advantage of being less dependent on the particle size as in the case of Mie–scatterers and it further increases the signal to noise ratio (SN > 4000). The increase in signal to noise ratio is owed to the simple fact that dirt or other particles in the solution won't contribute to the signal when

fluorescence light is detected. This will also be used later on to measure potentials in turbid solutions.

3.3 Measurement errors and limitations

To account for the uncertainty inevitably attached to every measurement some reasonable estimates for the occurring errors have to be made. Since effectively a probability distribution is measured, an error is hard to define. One source of error is certainly the fact that the histogram does not properly converge to the actual probability distribution for intensities or heights, which are not properly sampled due to deep potential wells. The PMT itself produces an intrinsic error (background noise) on the measured photon frequency, ΔI_S, which is estimated to be 1 kHz. Furthermore, the histogram is only a discrete approximation of the real probability distribution. That means that a greater bin width, ΔI_{bin}, results in a higher error.

$$\sigma_I = \sqrt{\left(\frac{\Delta {I_{bin}}^2}{N}\right) + {\Delta I_s}^2} \tag{3.12}$$

Via Gaussian error propagation and eq. 3.3 this can be transferred to an error of the measured distance, h, of the particle.

$$\sigma_h = \frac{1}{\beta}\sqrt{\left(\frac{\sigma_I}{I_S}\right)^2 + \left(\frac{\sigma_{I_0^S}}{I_0^S}\right)} \tag{3.13}$$

Here I_0^S is the intensity of a sphere sticking to the glass interface. The error on this value is rather large but of systematic nature. For the energy (eq. 3.6) the error is found in the exact same way by error propagation. The error on the counts in the histogram bins is assumed to be $\sigma_N \propto 1/\sqrt{N}$.

$$\sigma_{W^{SW}} = \sqrt{\left(\frac{\sigma_I}{I_S}\right)^2 + \left(\frac{\sigma_N}{N}\right)^2} = \sqrt{\left(\frac{\sigma_I}{I_S}\right)^2 + \left(\frac{1}{N^{\frac{2}{3}}}\right)^2} \tag{3.14}$$

The error on I_0^S is not taken into account for the total error on the energy value. The most prominent effect of this error is a deviation from the real absolute distance, but not the relative distances (systematic error). While the interaction energy is influenced by the systematic uncertainty of I_0^S, this only becomes important when more than one particle is used to measure a series of potentials. In this case it has an influence on the comparability. As already discussed when measuring a potential, no mean values are acquired, but a probability distribution. There is no simple way to determine the error on the convergence of the intensity distribution. In

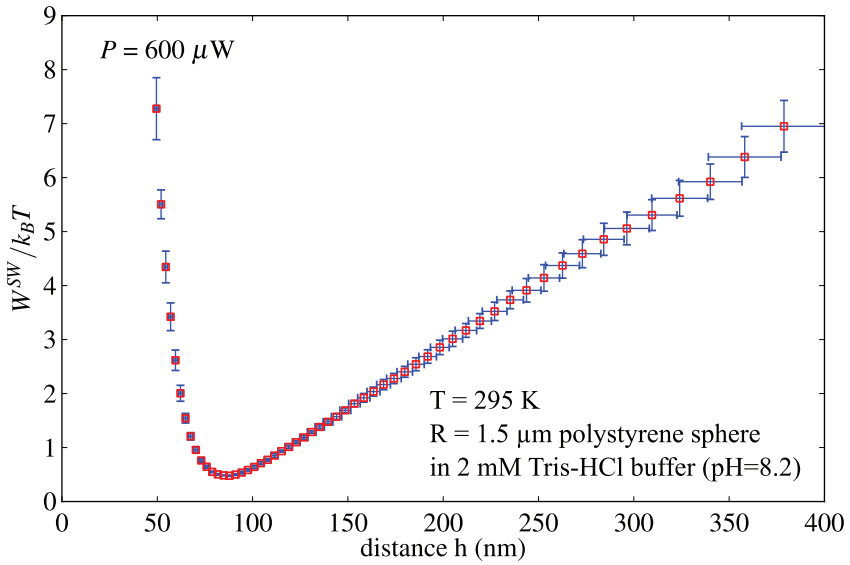

Figure 3.11: *The errors on a potential measurement are experimentally determined by repeating a measurement on one and the same $R = 1.5$ μm polystyrene sphere, trapped by optical tweezers at $P = 600$ μW, six times and averaging the resulting potentials. The errors are only of statistical nature, giving no hint to the size of the systematic error on the absolute distance.*

addition, there is no reliable way to determine the error on the intensity of a sticking sphere or errors caused by other unforeseen influences on the measurement (non perfectly spherical beads, contamination of the solvent).

To compare the theoretically assumed errors with the real uncertainty of an experiment, the potential stability of a trapped ($P = 600$ μW) $R = 1.5$ μm polystyrene probe sphere in 2 mM Tris–HCl buffer (pH = 8.2) is checked by repeating the measurement six times and averaging the result. The averaged potential with corresponding errors is shown in Figure 3.11. The single potentials were recorded by acquiring a total of 250 000 intensity values for each potential and using a total number of 60 bins in the histogram in order to calculate a potential. As predicted, the error increases with decreasing events. Moreover, the error for large separation distances is more pronounced. While the error on the energy seems reasonable, the one on the distance is significantly higher than predicted by the error analysis when compared to the example PMT measurement in Figure 3.5. The experiment does not offer any information about systematic error sources such as non exponential illumination, non-perfect reference when sedimenting the particle etc. Performing longer measurements would reduce the errors.

Leaving the measurement errors aside, there are also principle limitations to the method. First of all the accessible energy range is limited by the thermal energy k_BT. For deep po-

tentials that means that a particle is practically immobilized at one position. Also there is an upper limit to the forces (1 pN), which can be measured by TIRM, as well as the lower limit, which is approximately few femto Newton. Second, one of the biggest limitations is that the method only allows to measure in liquids and that the probe particles have to be stabilized to prevent sticking and enable Brownian motion in the potential well. Non spherical probe particles are also something hard to model and therefore uncommon. The choice of the solvent for the colloids is limited, too. The solvent's refractive index has to be smaller than n = 1.45 in order to create an evanescent wave with the used quartz glass cell (n = 1.51). Of course high refractive index glass cell shift this limit a bit, but the principal restriction to (semi) transparent interfaces remains. Furthermore, the probe particles have to be large enough to scatter a large enough amount of light to be registered by the detector. The scattering cross section shrinks with decreasing volume. For particles in the nano meter regime such as proteins or small colloids the intensity is two low to be detected. Here, the fluorescent approach might help. Nevertheless, the particles also become so light that they will not be trapped inside a potential anymore or in other words they won't stay close to the wall, where they can be measured.

3.4 Near wall diffusion

Beside the static potential data, dynamic information can be gained from the raw TIRM data by looking at the intensity time auto correlation function $g(\tau)$.

$$g(\tau) = \lim_{T\to\infty} \frac{1}{T} \int_0^T I^S(t)\, I^S(t+\tau)\, \mathrm{d}t \tag{3.15}$$

here τ is the lag time between two events and T the total measurement time. Since the measurements are discrete, the integral is replaced by a sum. The formalism to calculate the intensity auto correlation function out of the discrete intensity values of a recorded intensity trace becomes

$$g_j = \frac{1}{n-j} \sum_{i=1}^{n-j} I_i^S I_{i+j}^S. \tag{3.16}$$

The minimal lag time is set by the sampling time chosen to measure the intensities. In order to increase the available amount of data, the auto correlation function calculation is done in a gliding way. Here, actually only a small time window is analysed, effectively shifting this window over the raw data to calculate the correlation function. The values of the auto correlation function for high lag times would be inaccessible anyway, because the probe sphere is trapped inside a potential and usually does not escape. Typical intensity time auto correlation functions

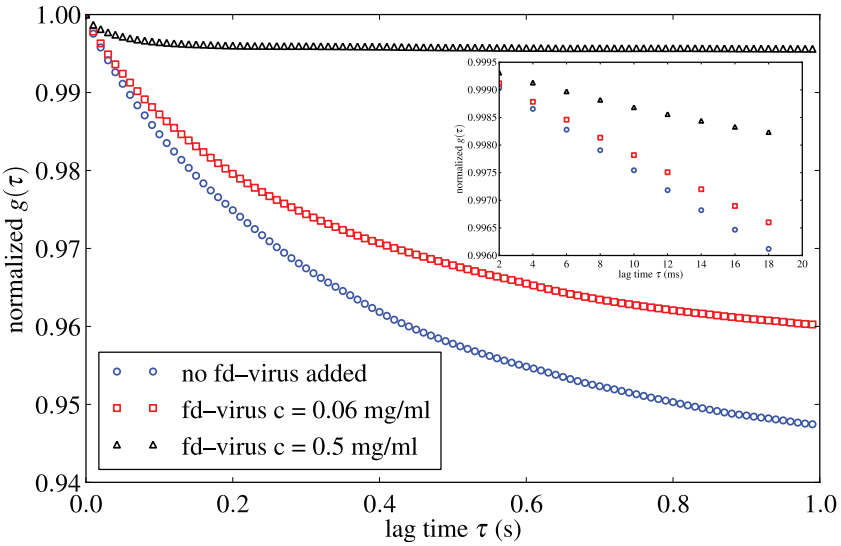

Figure 3.12: *Auto correlation functions calculated from raw TIRM intensity traces of R = 1.5 µm polystyrene spheres in 2mM Tris–HCl buffer, pH=8.2. The data had to be collected with the PMT to supply high enough sampling rates and is normalized to $g(\tau = 0)$. Addition of a depletant, here fd virus, deepens the potential. The time auto correlation functions of confined particles do not decay to zero. With increasing confinement strength the base line of the correlation function increases. The initial slope in the inset is approximately linear and delivers an estimate for the diffusion constant close to the wall.*

for different potential depths are given in Figure 3.12. These are recored with a R = 1.5 µm polystyrene bead trapped by optical tweezers and using a time window of one second. The correlation data is normalized to $g(\tau = 0)$. It is apparent that the values do not decay to zero as would be expected for a free particle (free meaning without any potential restricting the particles motion). With increasing potential depth, here realized by adding fd virus, a rod–like depletant, the decay becomes more and more shallow. The reason for this is that the particle becomes more and more confined in the potential well. By this the motion of the particle is dominated by the potential, which causes a correlation between two possible states of motion (the state of motion is determined by the position inside the potential). At short time scales the motion is truly Brownian, because it essentially does not feel the potential. So only the initial slope of the correlation function yields a physically meaningful estimate for the diffusion coefficient close to the wall. According to works by Bevan et al. [73,74] the diffusion coefficient can be extracted raw TIRM–data by the following relation.

$$D = \beta^{-2} \frac{\mathrm{d}g(\tau \approx 0)}{\mathrm{d}\tau} \tag{3.17}$$

$g'(\tau \approx 0)$ is the initial slope of the correlation function, while β is the inverse penetration depth of the evanescent field. Diffusion close to the wall is drastically slowed down due to lubrication forces. Theoretical predictions for this slow down have already been confirmed by TIRM experiments with a high degree of agreement [74]. But those predictions are only valid for particles in a solvent without any depletant added. The correlation functions show that the depletant causes additional friction, lowering the diffusion constant. The diffusion coefficient of particles in pure solvents can be used to infer the particle's distance to the wall without sedimenting it [73,75]. This won't be done in the course of this work, because the results have the tendency to be less accurate than those attained by sedimentation. The correlation function corresponding to the deepest potential in Figure 3.12 has an almost constant value. This means for really steep potential wells it is not possible to record information about dynamics of the particle. The most extreme case here would be an immobilized particle, where would not be any change of the correlation function at all.

3.5 Sample cell preparation

Actually, there are two kind of cells available for use with the presented setup. The mentioned full glass flow cells and a type supported by a frame. The framed cells consist of two standard microscopy slides mounted onto a black PTFE frame, which acts as a spacer. The microscopy slides are disposable and therefore less prone to wear. Furthermore, microscopy slides and cell frames are easily cleaned by successively sonicating them in acetone, ethanol and water and then blown dry with a jet of dried nitrogen. In this way the surfaces are cleaned from organic and inorganic contaminations. Another advantage over the full glass cells is that the surfaces of the microscopy slides may be coated in order to modify the surface. Yet for the sandwiched cells the PTFE and the glass have to be sealed tightly, which is done with a thin film of vacuum grease, while clipping the glass slide to the frame. This may lead to unintentional contamination of the measurement solution, which is avoided with full glass cells. Also the larger volume of the framed cells becomes unpractical for valuable sample solutions.

For the full glass cells, the fact that they cannot be disassembled means that they are harder to clean. For example, they may not be exposed to ultra sonic sound, since the joints and the connection pieces tend to break. In order to be able to reuse the glass cells, they are thoroughly cleaned by immersion in a mixture of 1:1 H_2O_2 (30 vol%) and H_2SO_4 (99 vol%) for over one hour. Afterwards the cells are rinsed with pure water (ρ_R =18 MΩcm) and blown dry with dried N_2. This procedure delivers very clean surfaces of the sample cells, free of any residual contamination. Nevertheless, it is rather aggressive. Although the glass is not severely

attacked by the acid it wears on them. That's why for simple contaminations a special basic soap is used to clean the cell (Hellmanex III). This is completely sufficient for all measurements with charge stabilized particles. The cells are left in the soap solution for several hours, rinsed clean with ultra pure water and blown dry with nitrogen.

Glass Syringes, burettes and tubes are cleaned in the same way as the microscopy slides by sonicating them successively in acetone, ethanol and pure water for approximately half an hour, each step. For the flow experiments or experiments, where the liquid is exchanged during the measurement, the already mounted cells may be rinsed with pure water and then with pure solvent to remove dust inside the cell, tubes and syringe. The tubes leading to the cell are attached by widening the tube ends to fit over the glass connecting piece of the cell. To seal it the tube is shrunk with a heat gun so that it sticks to the connection piece. With this procedure no glue or grease is needed.

3.6 Sample preparation

3.6.1 fd virus suspensions

Fd virus represents an unsurpassed model for rigid and monodisperse rods [48] with high aspect ratio. The wild type variant has a contour length of $L = 880$ nm, a diameter $D = 6.7$ nm, a molar mass $M_{fd} = 1.64 \times 10^7$ g/mol [76] and a persistence length of $L_p = 2.8$ µm [77]. Because of a persistence length of about three times its own length, it is commonly regarded as long, stiff rod. However, recent force-extension on M13 bactriophage (a virus virtually identical to wild type) and earlier laser tweezers experiments on wild type indicate that the persistence length might be much smaller, i. e. $L_p \approx 0.7$–1.2 µm. [78, 79]. Furthermore, fd viruses are highly uniform, which is owed to their biological origin. All viruses are almost identical due to the fact that viruses clone themselves by exploiting cells of host organisms. In the case of fd, those are e-coli bacteria [80]. In order to approximate the ideal of completely stiff, slender rods even closer, while maintaining the aspect ratio, a genetic mutant [81] of fd-virus is used, namely Y21M [82], in addition to wild type. These viruses have a persistence length of L_p =9.9 µm [81] through the alteration of a protein in the virus shell.

The greater stiffness of the mutant has already been confirmed qualitatively by determining the nematic–isotropic phase transition, which occurs at lower rod densities for Y21M as compared to wild type [48, 81]. Quantitative data for the Y21M persistence length were obtained from the analysis of the viruses' twisting and bending motion as observed by video

microscopy [81]. Apart from the increased persistence length, L_p, Y21M has the same properties as wild type.

Both fd virus variants are grown, following standard procedures described elsewhere [80, 83]. The viruses are then transferred to a 2 mM Tris-HCl buffer (pH = 8.2) with 15 % ethanol content by centrifuging them at 108 800 G for 8 hours five times, exchanging the solvent each time. The buffer is prepared with highly purified water with a resistivity of ρ = 18 MΩcm and a total organic carbon content of less than 2 ppb, while adding highly purified ethanol (Sigma Aldrich 99.6 vol%). The ethanol is added to the pure buffer before setting the pH or buffer concentration to suppress bacteria growth during the experiments. After having prepared the pure buffer the pH is set by adding HCl (Sigma Aldrich 1 M), while monitoring the pH value with a pH–meter. The concentrations of the fd stock solutions are determined by ultraviolet–visible (UV-vis) spectroscopy with an accuracy better than 1 % using Lambert-Beer's law at λ_{ext} = 269 nm with α_{ext} = 3.84 cm^2/mg [76,83]. The absorption coefficient is strictly only valid for wild type fd, but is expected to vary only slightly for Y21M [81]. For the measurements the stock solution is diluted to the required concentrations.

3.6.2 Gibbsite platelet suspensions

Platelets are widely present in nature (clay minerals, red blood cells, etc.) and can now be synthesized in a controlled manner in the laboratory (mixed metal hydroxides, gibbsite, etc.). The most prominent examples of colloidal platelets are natural clays [49], which are often used as rheological modifiers for surface coatings, paints, and drilling fluids [50–52]. Their rheological applications are based on the microscopic structural properties, originating from the highly anisotropic shape of the colloids and the inter–particle interactions. However, due to the flexibility and the large polydispersity in both size and shape, clay particles are hard to describe theoretically [49]. In the present work therefore a synthetic platelet type is chosen, which was developed in the van't Hoff laboratory in Utrecht. The colloidal particles are composed of gibbsite (γ–Al(OH)$_3$) and resemble platelets with a hexagonal shape and a thickness significantly smaller than the diameter of the circle enclosing them. Their synthesis is described in detail elsewhere [84]. Being of inorganic origin facilitates sample handling of the platelets, in contrast to biological samples such as fd virus [44, 85], since the particles require almost no special solvent conditions and offer stability in a broad spectrum of solvents [86]

The gibbsite platelets used here, with diameter $\bar{D}$ = 212 ± 56 nm and thickness L = 6 ± 10 nm, as determined by TEM, synthesized according to the standard procedure described elsewhere [87] were a gift from Debye Research Institute, Utrecht University. The platelets are coated with silica [87] to give them a negative surface charge and thereby avoid

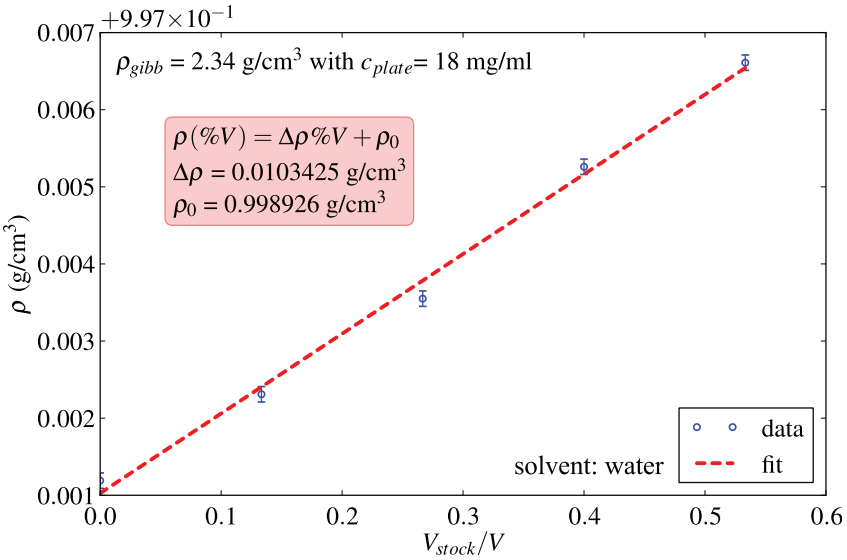

Figure 3.13: *Determining the mass density of silica coated gibbsite platelets by successively increasing their concentration in the solution. For gibbsite volume conservation is fulfilled and the determined mass density agrees reasonably well with the literature value.*

adhesion to the glass cells. The mass concentration of the stock solution is found to be c = 18 mg/ml by drying a small amount of suspension and weighing the remaining solid. For the measurement the solution is diluted with purified water (ρ_R = 18 MΩcm, total organic contents less than 2 ppb) to the desired concentration, while the ionic strength is set by adding NaOH (Sigma Aldrich 0.1 M) during dilution, so that the final platelet suspension contains 1 mM NaOH. Also fluorescent polystyrene micro spheres (R = 2.5 µm, thermo scientific G0500) or simple polystyrene beads (R = 3 µm, thermo scientific 4206A) are mixed with the sample, while diluting to supply probes for the measurement.

The density of the platelets is checked (see Figure 3.13) with a density meter (Anton Paar DMA 4500). For this purpose a dilution series is prepared and the density of each suspension is measured. This measurement yields the density of the platelets if the concentration, c, of the stock solution is known. Of course the density of the platelets is not allowed change when diluting the sample. But this requirement is well warranted, considering inorganic, non soluble material. In this case, the mean mass density, ρ, of the solution at a certain volume fraction of stock solution is given by

$$\rho = \frac{(1-x)V\rho_0 + Vx\rho_{stock}}{V} = \rho_0 + x\underbrace{(\rho_{stock} - \rho_0)}_{\Delta\rho} \tag{3.18}$$

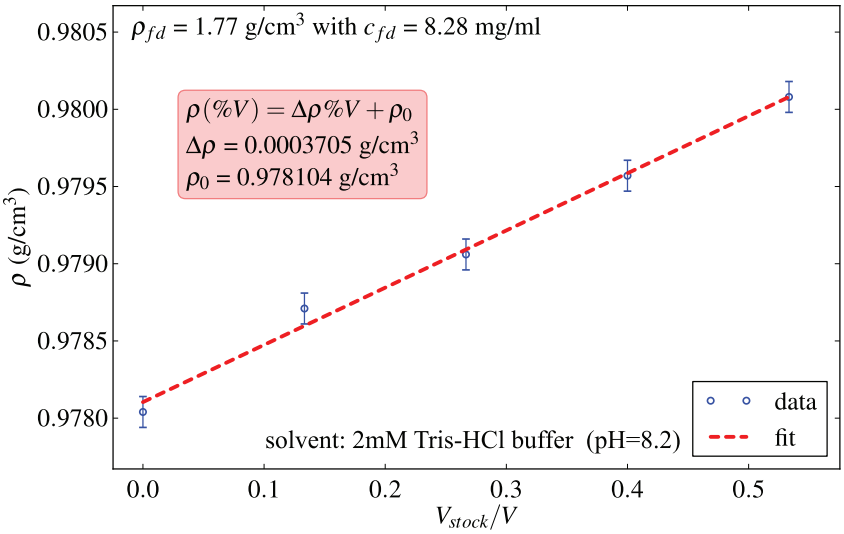

Figure 3.14: *Mass density of fd mutant Y21M, measured by successively increasing the mass concentration of fd virus. The density may not be a real density, since it is not clear if volume conservation is fulfilled for fd virus.*

This means that the measured density should increase with the fraction of stock solution in the measurement solution. Exploiting this, $\Delta\rho$ will be given by the slope if ρ is plotted against $x = V_{stock}/V$. Knowing the mass concentration of the stock solution, the total mass density of the stock solution is given by

$$\rho_{stock} = \frac{(V - V_{col})\,\rho_0 + V \cdot c}{V} = \left(1 - \frac{c}{\rho_{col}}\right)\rho_0 + c \tag{3.19}$$

where V_{col} is the volume of the insoluble colloid, V the total volume, ρ_{col} the mass density of the colloid and ρ_0 the mass density of the solvent. With eq. 3.19 $\Delta\rho$ becomes

$$\rho_{stock} - \rho_0 = \Delta\rho = c\left(1 - \frac{\rho_0}{\rho_{col}}\right) \tag{3.20}$$

so that the density of the colloid is

$$\rho_{col} = \frac{\rho_0}{\left(1 - \frac{\Delta\rho}{c}\right)}. \tag{3.21}$$

The actual measured value of the gibbsite platelets' mass density ρ_{gibb} = 2.34g/cm^3 agrees reasonably well with the literature value for the mass density of gibbsite, which is

ρ_{gibb} = 2.4g/cm^3 [88]. Of course volume conservation is a limiting factor when using this method.

The same technique may also be applied to the afore mentioned fd viruses. But the protein shell of the virus is relatively complex and it is hard to determine if the virus's shell doesn't bind water molecules and thus changes its volume. Furthermore, water can penetrate the virus body, because the virus shell is a hollow structure. This fact might even increase the number possible binding sites to protein shell. The result of the fd measurement is shown in Figure 3.14. The value for the density is reasonable, but should not be compared to the density of the dry protein. The fd measurement serves just as an example that the method is actually quite sensitive, because the change of density with increasing concentration is much smaller for the fd viruses than for the platelets. Checking the density can be seen as a complimentary method to determine the concentration of colloids if their mass density is known.

4 Results and Discussion

This chapter deals with sphere–wall interactions influenced by addition of different depletants and the effect of shear fields or light forces. It will be shown that using optical tweezers is helpful when doing measurements at rest, i.e. measurements without flow fields. In particular, tweezers will be used in a comparison of two types of fd virus, namely wild type fd and the stiffer mutant Y21M, which have been introduced in section 3.6.1. The viruses, being essentially long slender rods, follow the theoretical prediction for depletion interaction for infinitely thin rods well up to a certain concentration. For higher concentrations the model seems to break down and the depth of the potentials becomes greater than predicted by depletion alone.

The presented shear experiments lead to the conclusion that tweezering a particle, while applying a shear flow results in a significant influence on the interaction potential. This effect is strong enough to hide possible effects of shear fields on deplentant agents. Based on this fact the use of optical tweezers is abandoned when investigating the effect of shear flow on depletion potentials. A direct measurement of depletion caused by rigid, hard platelets is done for the first time using the CCD–camera as a detector. For these experiments the tweezers have only limited use, even for measurements without flow, since the platelets create turbid solutions, which interfere with the optical tweezers.

Shear measurements with the intend to shear align the deplentants are performed. It is expected that an alignment of the depleting particle species leads to an alteration of the depletion behaviour. When exposing fd virus to a shear gradient almost no effect is observed. Experiments with platelets display a decrease of depletion interaction with increasing shear rates, but only below a certain mass concentration of platelets.

4.1 Tweezers and shear flow

This part will present some of the first ideas to measure sphere–wall interaction in a shear field. Tentative experiments with the optical tweezers keeping the particle in place, while flowing liquid through the sample cell are performed. In addition to the fundamental problem of being restricted to low flow rates, which do not exceed the trapping strength, some unexpected effects such as an increased apparent weight on the measured potential make the approach unfeasible, as will be seen in the following experiments.

4.1.1 Measuring with spatial filtering

As described in section 3.2, the standard configuration uses a pinhole as spatial filter when detecting intensities with the PMT (penetration depth β^{-1} = 150 nm, HeNe laser source). The setup is left in its original state, while a flow field of unknown magnitude is generated by opening the valve on the reservoir. The flow mass controller is not yet used, since these following experiments only serve as a simple way to test if any influence of a flow field might be observed.

During the experiments, interaction potentials between a glass wall and a $R = 3$ μm charge stabilized polystyrene sphere (thermo scientific, 4206A) in a 0.1 mM NaOH solution are recorded with and without flow using the standard setup. The particle is trapped with the tweezers and a reference potential (no flow) is recored at a laser power of $P = 380$ μW. After this, the cell is rinsed with pure solvent, while keeping the particle in place with high setting of the laser tweezers. This is done in order to decrease the chance of other particles entering the field of view. Having disposed of excess spheres inside the cell a flow, here of an unspecified magnitude, is induced by letting liquid flow through the cell. In the presented case, a cell with a thickness of $d = 2$ mm is used, which means that the actual shear rates will be quite low (see section 3.2.4). The three potential minima in Figure 4.1 seem to have different distances from the wall depending on the magnitude of the flow. In particular, for the case where the particle is exposed to a high flow field, the minimum seems to be farther away from the wall as compared to the quiescent state. Yet the potential shape appears to be unchanged. It is obvious that the distance of the minimum cannot change without any kind of force acting on particle, which would alter the potential shape. Also, for a particle in front of a wall, no normal forces are expected to occur in shear fields (see section 3.2.5). The only conclusion is that this is some kind of measurement artifact. The question is, what would change the distance without actually changing the distribution of intensities or heights. The only way to achieve this is to attenuate or increase the intensity of the illumination or the detected light, so that the relative

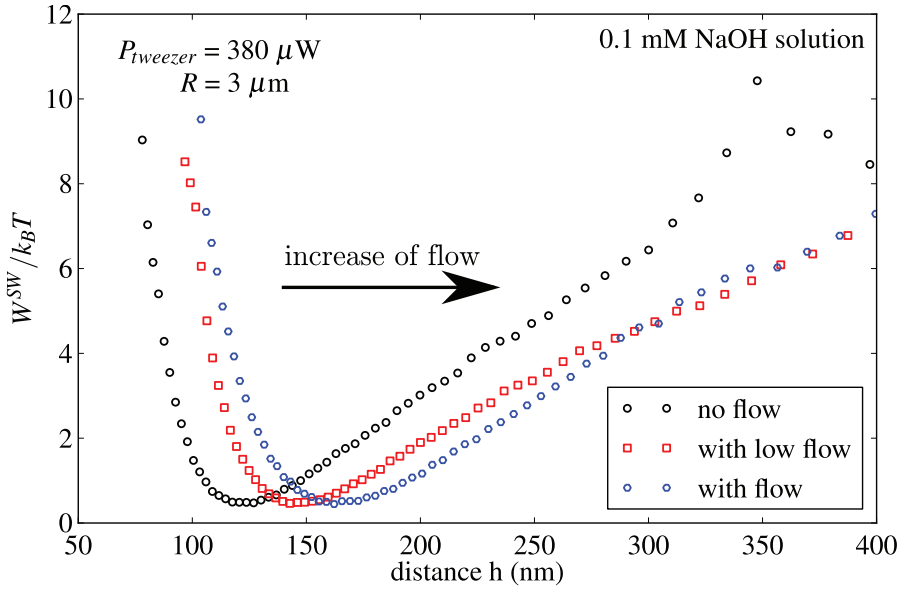

Figure 4.1: *Different potentials for a R = 3* µm *polystyrene sphere in 0.1* m*M NaOH solution, which is trapped by optical tweezers at P = 380* µ*W, are measured at different flow rates. The sampling time for the measurement is 5 ms and a total of 250 000 intensity values is measured for each potential. The minimum position of the potential apparently shifts to higher distances with increasing flow. But this is just a measurement artifact caused by a displacement of the particle in the flow field and an attenuation of the absolute intensity caused by the pinhole in front of the PMT*

changes are preserved, but the absolute intensity is decreased. The illumination laser is certainly not influenced by the flow field. Observing the particle on the camera picture reveals that the particle is pushed into the direction of the flow. This is expected because the 2D-trap, created by the optical tweezers, doesn't have an infinitely deep potential well. The trap can be thought of as a spring attached to the particle. In this case it is clear that the particle is displaced by an external force. The higher the flow or the friction force caused by the flowing liquid the greater the displacement. The reason for the smaller detected intensity values is that the spatial filter in front of the PMT cuts away part of the particle's airy disc, which has laterally a non homogeneous, radially decreasing intensity distribution (see Figure 4.2). By shifting the position of the pinhole it can be seen that the intensity is increased again, having previously been decreased by applying a shear field. It turns out, that it is also possible to decrease the distance by deliberately misaligning the pinhole prior to the measurements. In this scenario the particle is pushed into the optimal or a better detection position by the flow.

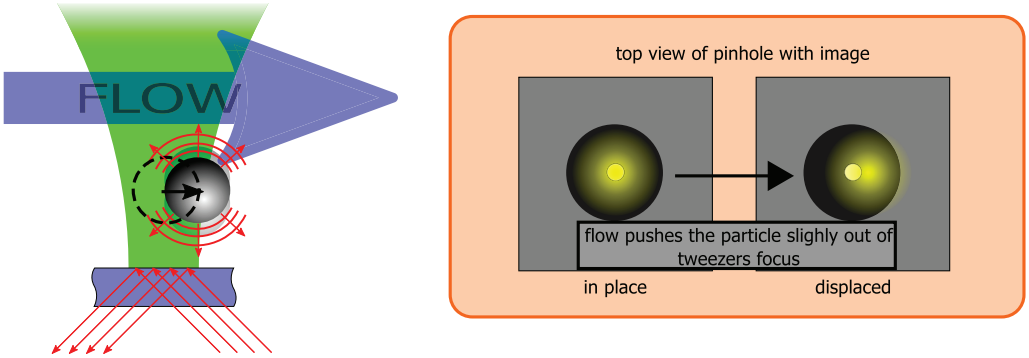

Figure 4.2: *When a flow is applied the particle moves inside the trap and also the projection or the image on the pinhole is moved. The airy disc of the scattering point does not have a homogeneous intensity distribution. If the illumination spot was centered with respected to the pinhole in a quiescent state, the shift causes less light to pass through the pinhole, which decreases the overall intensity registered by the PMT.*

Conclusion

In further experiments the pinhole will have to be removed when measuring under flow in order to avoid the shift and enable to measure absolute distances by sedimenting the particle. Of course this is done at the cost of signal to noise ratio, since the likelihood of collecting stray light without a pinhole increases. Even if no particles are visible in the field of view with the camera, the picture observed by the PMT might differ.

4.1.2 Measuring without spatial filtering

The next logical step is to try a measurement without the pinhole in place. Once removed great care has to be taken that there is not more than one particle in the field of view when recording an intensity trace. The following series of experiments will utilize a charge stabilized R = 1.5 µm polystyrene sphere (thermo scientific, 4203A). It is suspended in a 2 mM Tris–HCl buffer at pH = 8.2 with no depletant or other additive added to the solution. The measurements are performed at room temperature (T = 295 K). For illumination the HeNe laser is used, impinging under an angle of incident, supplying a penetration depth of β^{-1} = 150 nm. First, a sphere is trapped by the optical tweezers and then the cell is rinsed with pure buffer several times in order to flush other spheres out of the cell. This reduces the chance of second sphere entering the field of view when a flow is applied. The flow is regulated and controlled by the flow mass controller via the computer. During the experiments, it is important that the flow does not become too high, otherwise the particle is pushed out of the trap and escapes.

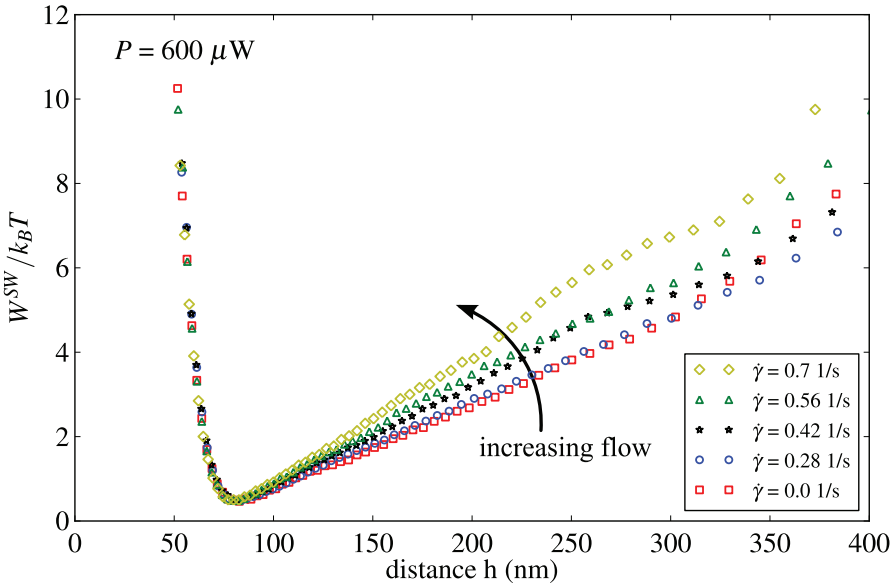

Figure 4.3: *The figure shows potentials measured at various flow rates at a trapping strength of 600 μW. The linear branch of the potential becomes steeper with increasing flow. The sample was at room temperature during the measurement.*

For moderate enough flows, it is expected that the flow won't change the potential profile. This assumption stems from the case of a completely free sphere, where no normal forces should act on it in a shear field (see section 3.2.5). To check this expectation, potential measurements are performed at different power settings of the tweezers and flow rates, respectively shear rates. For each potential 500 000 data points with a sampling time of 2 ms are recorded. Before applying a flow, a reference is recorded without any flow present. The shear rate is calculated from the mass flow through the cell according to the discussion in section 3.2.4. The first tweezering power is 600 μW. The recorded potentials for this case are shown in Figure 4.3.

It is apparent that the potential seems to deepen with increasing flow. Of course speaking about the potential depth is only meaningful with regard to an absolute potential value. As discussed in section 3.1 it is impossible to measure an absolute potential without some kind of reference. But in the presented case there is no physically meaningful point of reference. So when saying the potential becomes deeper, this means that some artificial reference had to be defined. Here, all potentials are superimposed with respect to energy, implicitly demanding that the energy value at h_0 (spatial position of the potential minimum) is equal for all potentials.

Specifically this means that the only indicator for a deeper potential is that the slope value of

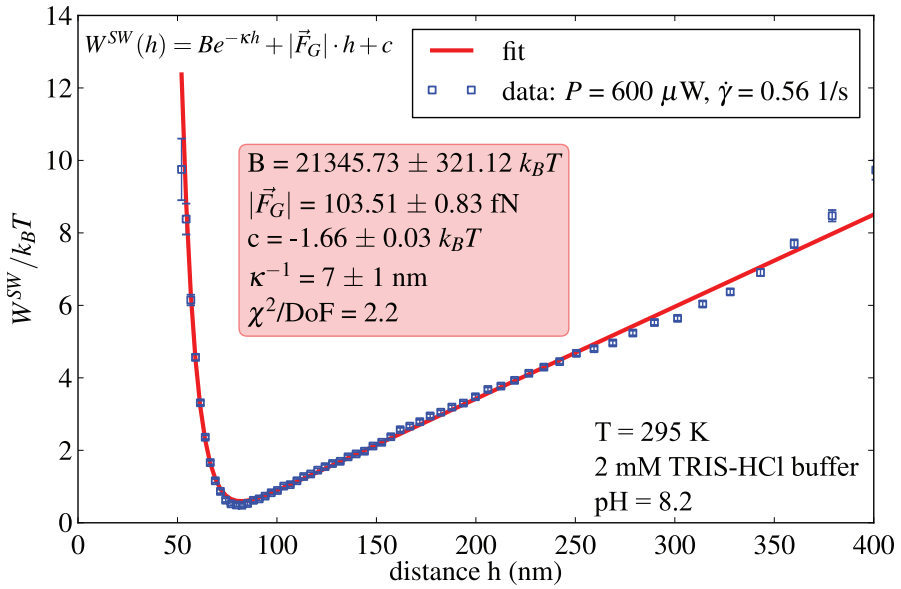

Figure 4.4: *Comparison of interaction energy data and fit for a R = 1.5* µm *polystyrene sphere in 2 mM Tris–HCl (pH = 8.2) buffer exposed to a weak shear field. It is obvious that data and fit are in very good agreement. This means that the overall nature of the potential is not changed by the flow field.*

the linear branch becomes higher with increasing flow. For the highest flow rate the apparent weight of the particle appears to have increased by 50 %. This is a quite large effect and somehow unexpected. To quantify the change of the potential induced by a shear flow, a potential model is fitted to all the curves with a Levenberg–Marquardt non–linear least square fitting algorithm. One example fit is shown in Figure 4.4. The used model (shown in the figure) is actually a superposition of eq. 2.33 and 2.2. But the weight force here is an apparent weight force, combining the contribution of the radiation pressure and the buoyancy corrected mass of the particle. Van der Waals attraction is completely neglected. Comparing model and data shows that both are in good agreement, which justifies the assumption of no or non perceivable van der Waals forces. Fitting the model B, $|\vec{F}_G|$ and c are chosen as free fitting parameters. The parameter c has no physical meaning and is just a simple additive constant in order to shift the model curve along the energy axis. The Debye length, κ^{-1}, is not a free fit parameter and is kept constant after once choosing a suitable value for the fit to the reference data. The value of 7 nm for the Debye length is slightly lower than the value of 9.6 nm, expected for a 2 mM Tris puffer at pH = 8.2. This may be attributed to errors during the pH measurements. Or in other words, the buffer may contain a little higher amount of HCl than

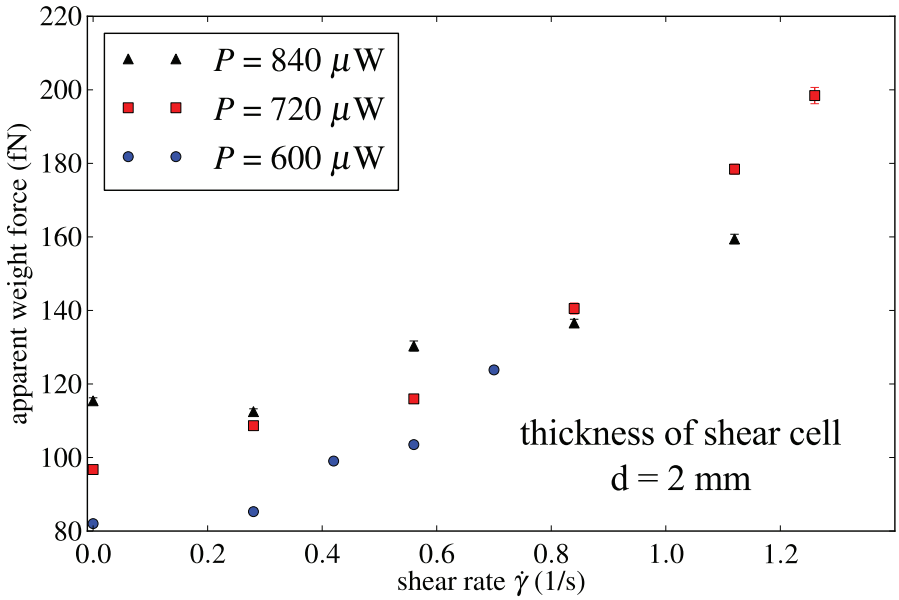

Figure 4.5: *The overview shows the apparent weight forces, extracted from fits to the potentials, plotted against the applied shear rate. For higher laser powers it appears to get harder to achieve the same relative increase in apparent weight.*

anticipated, because probably the pH–electrode was not perfectly calibrated or the temperature of the buffer was not the same as for the given pKa value of the buffer. Nevertheless, for all measurements data and model agree well, despite the fact that the potentials are altered by an imposed flow field. Furthermore, the mean sphere–wall distance of the particle is not changed in a perceivable fashion when it is exposed to a flow field. Maybe there is a minor shift towards the wall due to the higher weight force, but this cannot be resolved by TIRM. The electrostatic part of the interaction does not seem to be affected by the flow at all. In order to further investigate the effect, two more powers of the tweezers are set and different flow strengths are applied. For this the experiment is repeated for higher settings of the tweezers: P = 720 µW and P = 840 µW (see Figures 4.6(a), 4.6(b)).

Yet the picture stays the same. With increasing flow the particle seemingly becomes heavier, but it gets harder to achieve the same magnitude of increase for higher trappings strengths. The fitted apparent weight forces, extracted by the fits to the potential data, are plotted against the shear rate in Figure 4.5 for the different laser powers. The apparent weight force grows with increasing laser power and applied shear rate. For higher trapping strengths, it takes larger flow rates to see a comparable increase in weight force. This already gives a hint to an explanation for the observed phenomena. After the force starts to rise as soon as a certain

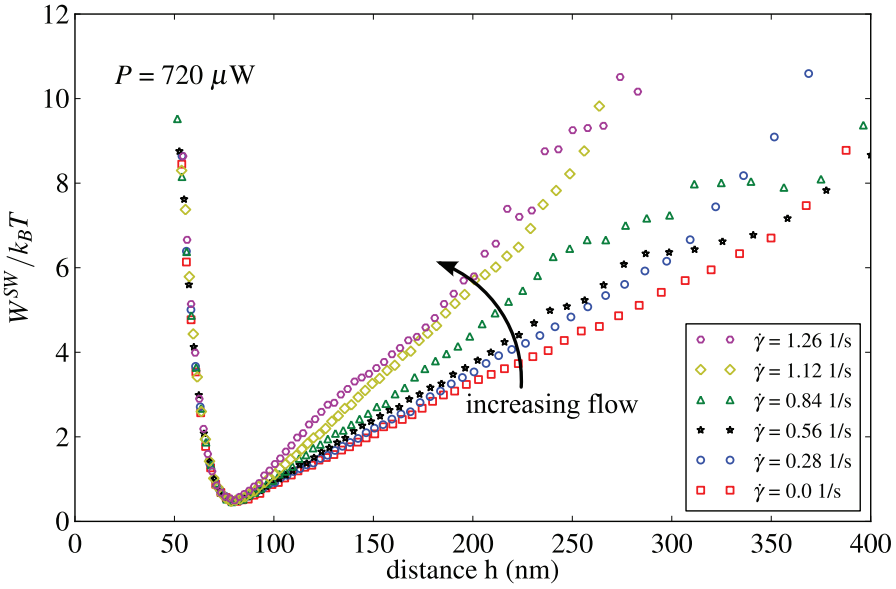

(a) Effect of flow, $P = 720$ μW

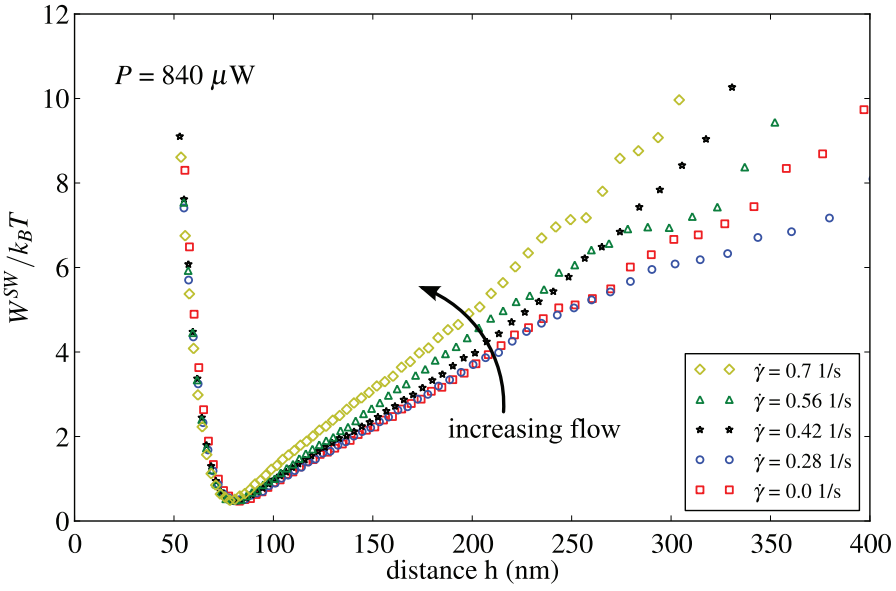

(b) Effect of flow, $P = 840$ μW

Figure 4.6: *The two plots in (a) and (b) show the change of the interaction potential by increasing shear at the two higher laser powers. The linear branch of the potential still increases with increasing shear flow.*

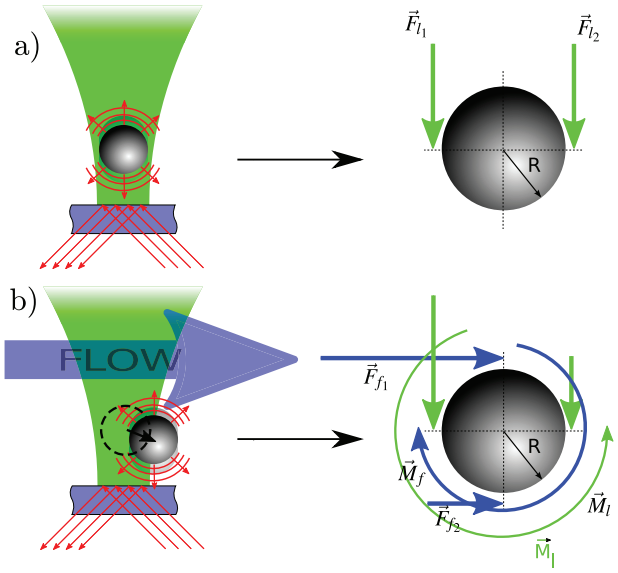

Figure 4.7: *Case a) shows the situation without flow: the sphere is in the middle of the trap and the forces acting on the sphere at both sides of the meridian are equally large. b) the sphere has been shifted by a flow field. Light forces and the shear field both exert a torque on the sphere. Both torques are counteracting each other, which leads to an additional force contribution normal to the wall.*

threshold is passed, it increases approximately linear with the applied shear rate or flow. Other than that, there seems to be no identifiable trend to the data. Just to stress this again, due to the finite tapping strength only a limited range of flow rates is accessible, therefore for low laser powers less data could be collected. Too high flow rates result in a loss of the particle, which necessitates to redo the whole measurement series.

Conclusion

The fact that there is an increase of the force at all is kind of unexpected when assuming free particles. Yet of course the particle in the current case is not entirely free. Its motion is restricted to one dimension. According to the discussion in section 2.1.1, the trapping potential is created by a force imbalance of the acting light forces, as soon as the particle moves out of the focus or the center of the Gaussian beam. But this is exactly what happens when a flow field is applied. Watching the camera picture, one can see that the particle moves slightly into the direction of the flow. By itself this should not increase the normal forces acting on the particle. At most, it could even decrease the light pressure, because the intensity impinging on the particle could decrease. However, this decrease would only occur if the laser focus were larger than the particle. In the experiment the laser focus is of the order of sub micro meter, while the particle has a diameter of 3 µm. So a slight shift of position does not decrease the radiation pressure on the particle. In order to see the full picture, also the properties of the flow field have to be considered.

In a shear gradient the velocities and thus the friction forces exerted on the particle are asymmetric in the direction normal to the wall (see Figure 4.7). In consequence, a free particle being dragged along in a shear flow would start to rotate, so that no force towards the wall could be induced by the shear flow. A linear shear flow can be imagined to be composed of a superposition of a purely rotational flow and a purely translational flow, what immediately illustrates why the particle starts to rotate if there is nothing to restrict the rotational motion. Trapping the particle with optical tweezers and applying a flow field slightly misaligns the particle with respect to the focus of the laser beam. This causes the acting light forces on both sides of the meridian to attain different magnitudes (see Figure 4.7). Thus the tweezers exert a torque on the particle and thereby also start a rotation. If there is nothing counteracting the momentum on the particle, it will be accelerated all the time. Naturally, there is the friction of the liquid, so that the rotation speed will always be finite. Yet in a shear flow there is another torque imposed on the sphere.

Looking at the illustration in Figure 4.7 reveals that the shear forces and the light forces will always oppose each other, creating an effective torque. This torque is lower than the one caused solely by the shear field. This means the particle is slowed down by the tweezers. To slow down the particle there has to be some kind of breaking or friction force. Other than the friction caused by the liquid, this friction acts mainly on one side of the probing sphere (the side with the higher tweezers intensity). This results in an extra force contribution pushing the particle towards the surface. This can be envisioned as follows: the light forces become unequal as the particle is pushed out of the tweezers' beam center. The momentum transfered by the light alone is perceived as friction, which causes the particle to slow down its spin. This is very much like a rotating wheel, where a force is applied to one side, in order to slow it down. The fact that the particle is propelled towards the surface has some implication if the sketched naive picture is really true. First of all, the particle will start to rotate, with or without the tweezers. The rotation is expected, but generally hard to measure [89] for small particles. The observed increase in weight connected to the torque on the sphere would allow a pretty accurate way to measure the shear induced rotation of the sphere and by that the shear gradient.

On the other hand, from the view point of realizing a shear experiment this effect is somewhat undesirable. It is strong enough to hide most other contributions to the particle–wall interactions, so that adding depletant and observing the effect of flow on the depletant agent becomes unfeasible. Actually, experiments with tweezers, flow and fd virus have been performed in the course of this work, but were a failure. An idea of making a reference for every applied shear rate without depletant, which could later be subtracted form the measurement

with depletant turned out to be extremely cumbersome. The particle escaped most of the time and the referencing didn't work properly. In short, the measurement were highly unreliable. This means that doing a shear experiment, while trapping the particle by optical tweezers is virtually impossible to realize – at least with the setup, which is used here. In effect, the whole idea of measuring under shear flow, while using the PMT has to be abandoned. With the PMT only one particle may be observed at a time, so that the statistics would always be very poor, considering the sojourn time of a particle in the field of view when a flow is applied (for moderate flows this is a time of several seconds). From now on for measurements under flow a different method, employing the camera, described in section 3.2.5, is used to measure interaction energies.

4.2 Depletion caused by fd virus

This section will cover the measurements of near wall interaction potentials influenced by a rod–like depletant, namely fd virus. In a first step, measurements in quiescent solutions will be performed, comparing wild type fd and the stiffer mutant Y21M (see section 3.6.1). The two variants differ only in persistence length. It turns out that, concerning depletion potentials, there is no discernible different between the two variants. The difference in stiffness seems to be negligible for depletion. Yet for higher mass concentration of fd virus the theoretical model describing depletion for infinitely thin rods appears to break down. It doesn't matter if the stiffer or the wild variant is used, the behaviour stays the same. Depletion measurements are conducted using different probing sphere sizes, showing that the transition concentration, above which the model breaks down, depends on the choice of the sphere size. Up to this point only some vague speculations aiming to explain the observed deeper potentials can be made. In particular the comparison to earlier results of Lin et al. [45] on the depletion behaviour of fd virus is confusing. Those authors measure much weaker attractive interaction than expected, while in this work good agreement with the theory for depletion at low concentration is found and the rods cause a stronger attraction than predicted above a certain transition concentration. Complementary to the potential measurements the short time diffusion of the probing spheres is derived from the raw intensity traces, as sketched out in section 3.4. The short time diffusion does not show any transition form one regime to another one. In order to better understand the behaviour at higher concentrations, more data is reanalyzed with a slightly modified model function. To extend the measurement, complementary experiments with fd virus under flow are performed, with the aim to align the rods in a shear gradient, giving rise to a change of the depletion potential.

4.2.1 Comparison of wild type fd and Y21M

When using fd as a depletant it us usually modelled as a long slender, perfectly rigid rod. However, this is a drastic over idealization of real fd virus. The virus shell of the wild type variant, while quite rigid, having a persistence length of L_p = 2.8 µm [77] compared to its length of L = 880 nm, still has a finite flexibility. In terms of rigidity there exist better alternatives for rod–like depletants such as bohemite rods [90] or tobacco mosaic virus [91]. Yet when it comes to monodispersity and high aspect ration, fd virus is unsurpassed, due to its biological origin (see section 3.6.1). One issue is, whether the finite flexibility of wild type fd virus has an influence on its depletion properties at all. To investigate this point an fd mutant, namely Y21M [82] is used. It has a three times higher persistence length, L_p = 9.9 µm [81], than wild type fd, as determined by light microscopy, but otherwise unchanged properties. Another way to confirm the higher stiffness of Y21M is to determine the isotropic–nematic phase transition [92, 93], which is shifted to lower mass concentrations as compared to wild type fd. This check was actually performed for the used stock solutions in order to make sure, the results were not affected by mixed or contaminated samples.

For the investigation of the influence of stiffness on the depletion behaviour, the virus samples are both prepared as discussed in section 3.6.1. As solvent for the virus suspension a 2 mM Tris–HCl buffer with an ethanol content of 15 % to suppress bacteria growth at pH = 8.2 is used. While the virus stays unaffected by the ethanol, the viscosity of the buffer is increased to η = 1.66 mPas (this is strongly dependent on the ethanol content) compared to that of purely water based buffer (η = 0.98 mPas). But this fact shouldn't have any influence on simple depletion interaction. The virus concentration is set prior to a measurement by diluting the stock solution (already in Tris–buffer) with pure buffer. The measurements are performed in a glass flow cell with a thickness of d = 2 mm. The cell is connected by tubing to a reservoir in form of a 5 ml glass syringe with a nickel valve. The experiment is started by inserting pure buffer with R = 1.5 µm polystyrene spheres (thermo scientific, 4203A) into the measurement cell. A suitable sphere has to be found and trapped by the optical tweezers. Usually the spheres concentration is low enough to only have one sphere in the field of view. If for any reason there are too many spheres, a particle is trapped with a high tweezers intensity and the cell rinsed with pure buffer to remove the excess spheres.

The angle of incident of the HeNe illumination laser is chosen to yield a penetration depth of β^{-1} = 150 nm. The pinhole is kept in place for the following measurements to exploit the better signal to noise ratio. Since no flow will be applied, this won't have any effect on the measurement. Once it is certain that only one sphere is in the field of view, the tweezers laser intensity is decreased to the lowest possible value, in order to have the shallowest reference

potential possible. This is done to supply the highest measurement range, since the range is restricted by the thermal energy of the particle.

Once a reference potential in pure solvent is recorded, the solution surrounding the particle is exchanged with one containing a defined concentration of depletant. To avoid unintended dilution the cell is rinsed with 5 ml of the new measurement solution with a given fd concentration, while keeping the particle trapped at a high setting of the laser tweezers. After a series is completed, the cell is rinsed again with pure buffer and it is checked if the original reference potential agrees with it. Succeeding this, 0.1 M NaCl solution is inserted into the cell, to suppress all electrostatic interaction and stick the particle to the glass wall to record the contact intensity. For comparison, measurements on wild type and Y21M are performed at the same concentrations, yet in separate measurement series. The resulting total potentialds of these two measurement series are shown in Figures 4.8(a), 4.8(b). The potentials are shifted to lower energy values to illustrate the increasing potential depth with growing fd concentration. Except for a variation at lower distances, the fit curves, describing a superposition of reference and depletion potential, agree with the measured potentials. The employed potential model for the reference is the same as discussed in section 4.1.2 – a superposition of electrostatics and the apparent weight of the particle. For the data with depletant present, the reference fit is subtracted from the data points to yield a pure depletion potential. Of course this implies that the conditions of the solvent do not change and the potential is not influenced in any other way than by depletion. The pure depletion potentials at a given concentration are fitted with the theoretical description derived in section 2.1.4.1. The final result for depletion caused by dilute rod suspensions was given by

$$\frac{W_{dep}^{SW}(h)}{k_B T} = -\frac{\pi}{3}\frac{cN_A}{M_{rod}} RL^2 \left(1 - \frac{h}{L}\right)^3 - W_{dep}^{+} \tag{4.1}$$

except for the additive constant $W_{dep}^{+} = W_{dep}^{SW}(h = 880\text{nm})$, which needs to be subtracted in order to have the potential level out to zero for distances greater than the rod length $L = 880$ nm. The additive constant is necessary, because no absolute energy values can be measured and the depletion potentials go to W_{dep}^{+} instead of zero. The value W_{dep}^{+} is also the value used to shift the potentials in order to show the real potential depth. This means that the end of the depletion range is used as reference point for the measured full potentials. For the fits the concentration, c_{fit}, and the additive constant W_{dep}^{+} are the only free parameters. Rod length, L, molar mass M_{rod}, sphere radius R and temperature T are assumed to be known and kept constant during the fit at independently determined values. Full depletion potentials cannot be mapped out due to the limitations of the method, so that there are no data points describing

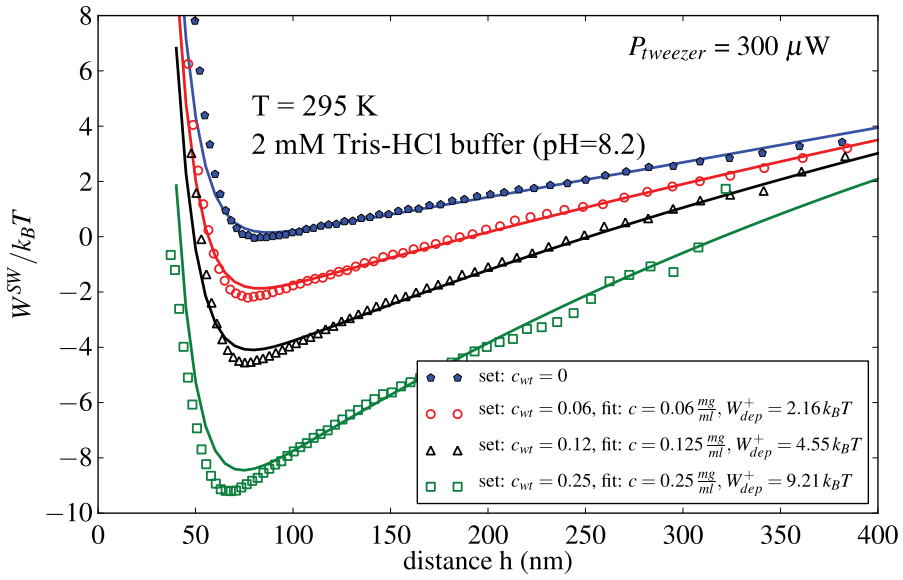

(a) Effect of wild type fd on a full potential

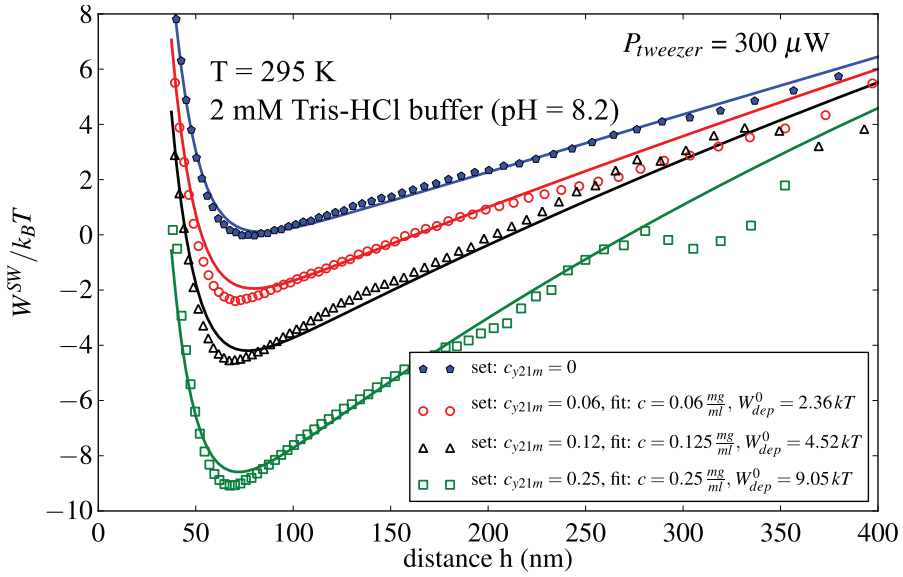

(b) Effect of the stiffer Y21M mutant on a full potential

Figure 4.8: *The potentials in (a), (b) show the effect of increasing fd concentration. The potentials become deeper the more fd virus is present. This is shown by shifting the potentials by W^{+}_{dep}. The fits to the total potentials are given by the solid lines. The agreement between model and data is sufficient. There is some deviation between data and fit for distances smaller than 80 nm.*

the region where W_{dep}^{+} is located. That is why the constant is determined by the fit and a consequence of the boundary condition that there is no depletion for distances greater than the rod length.

In order to give a better overview, the depletion potentials for all measured concentrations are normalized to the so called contact value $W_{dep}^{SW}(h = 0\text{nm}) = W_{dep}^{0}$. They are shown in Figure 4.9(a). The presented data are limited to a small range of separations. Distances over 300 nm have too poor statistics to be comparable (deep potentials). At distances below 80 nm there seems to be some kind of deviation from theory, which is not fully understood (see section 4.2.3). One possible explanation for this deviation is non perfect referencing. Nevertheless, as will be seen later on, it is present in virtually all measurements. This could either mean that the solvent conditions are changed by an increase of the fd concentration or some other effect is present, which is not accounted for. In spite of the discrepancies, the agreement between theory and data is quite good in the separation range between 80 and 300 nm. No discernible difference of the caused depletion of Y21M and wild type is seen in the presented measurements.

Yet the measurement still have a weak point. The series were performed with different probe spheres, meaning that a small effect might be covered by the error caused through polydispersity. To redeem this flaw a show case experiment is performed. In this, again, a R = 1.5 μm polystyrene bead is used and the rest of the conditions are kept the same. After recording the reference potential of the bare sphere, a suspension with c = 0.24 mg/ml wild type fd is inserted into the cell and a measurement is performed. Then the cell is rinsed with pure buffer to remove the solution inside the cell and finally the cell is filled with a Y21M solution of the same concentration as for the wild type measurement. The direct comparison is shown in Figure 4.10. There is almost a perfect match between the depletion potential caused by the two fd variants. So if there is any effect of flexibility, it cannot be resolved by TIRM measurements.

It is important to note that most potentials were recorded at rod concentrations above the overlap concentration $c^* = 6M/\pi L^3 N_A = 0.076$ mg/ml. Nevertheless, a first order density approximation is used as a theoretical model to fit the data, which implies dilute suspensions.

In order to validate this approach, numerical calculations of the depletion potentials according to Mao et al. [40,94] are performed. This is done to proof that even for regions, where there is already overlap between the rods the simple theory is still valid. The overlap concentration is defined by the concentration, at which the volume of a sphere with a radius, $r = L/2$, is occupied by exactly one rod in the suspension. The results of the numerical calculations are displayed in Figure 4.9(b), where depletion potentials induced by perfect rods versus elevations

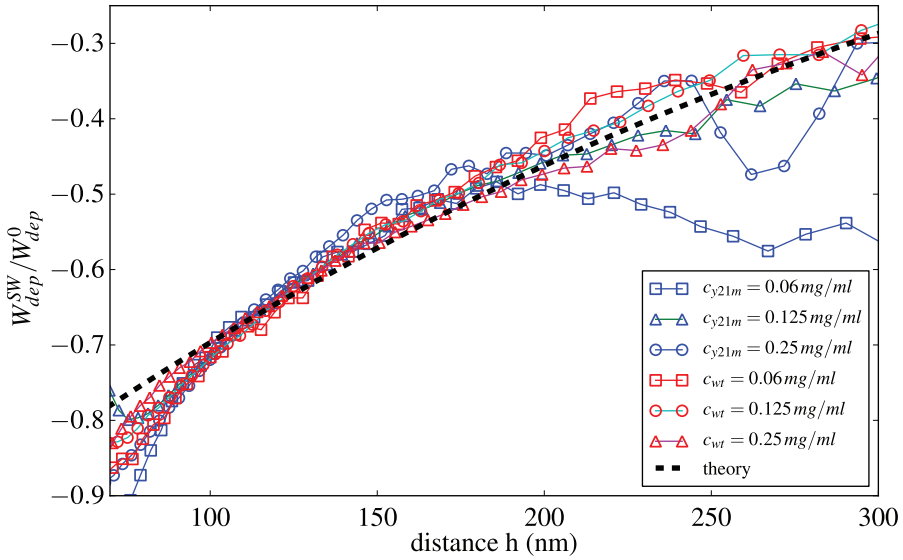

(a) pure depletion potential caused by wild type and Y21M fd in comparison

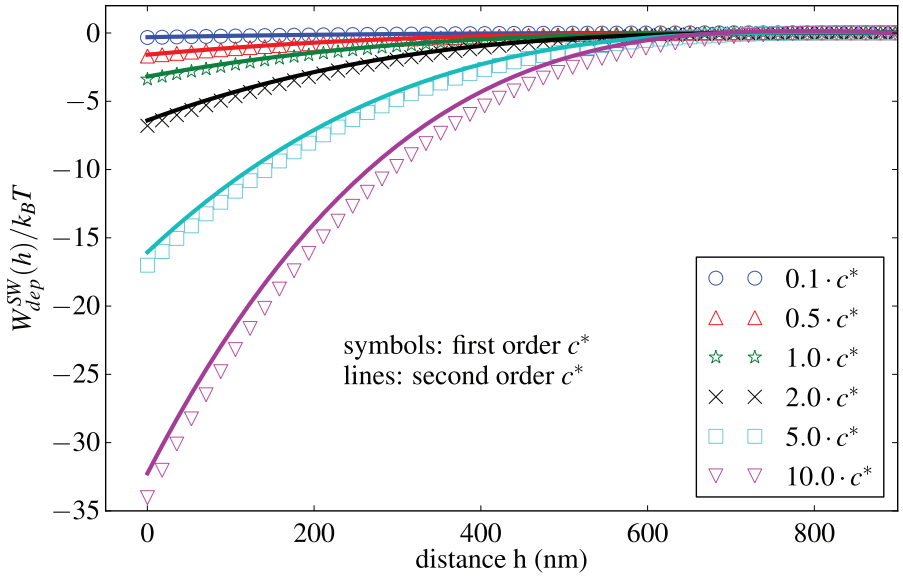

(b) Numerical calculations to verify first order approximation

Figure 4.9: *In (a) a direct comparison between wt fd and Y21M is shown. The depletion potential is normalized to the contact value, so that all curves collapse onto one. (b) verifies the use of the fist order theoretical description. The deviation only becomes perceivable at much higher concentration compared to those measured here.*

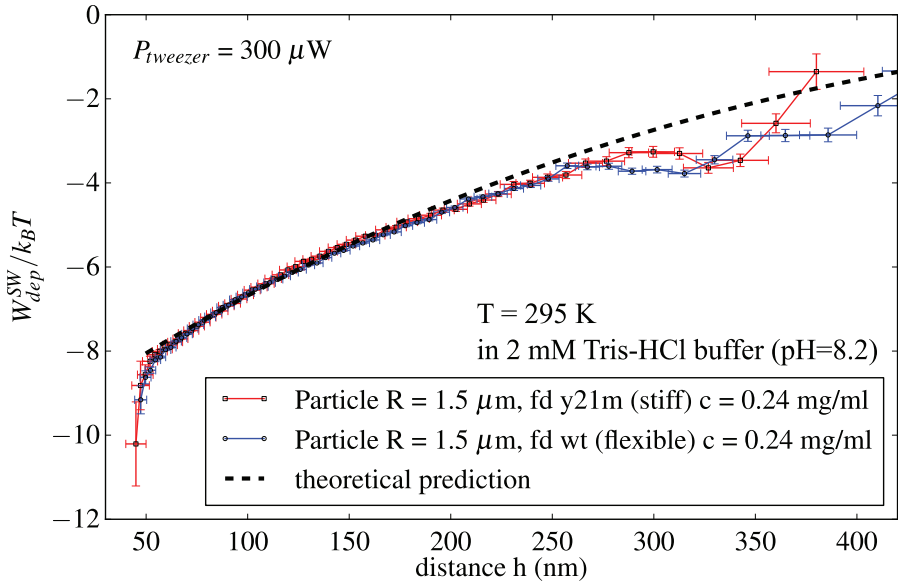

Figure 4.10: *Direct comparison between the two virus variants. Measurements were performed on one and the same sphere in one spot, keeping all experimental influences constant. There is no visible difference between the two fd species in terms of depletion interaction.*

for different rod concentrations are plotted. The symbols are calculated with eq. 4.1 using rod length, $L = 880$ nm, sphere radius $R = 1.5$ µm, molar mass $M_{rod} = 1.64 \times 10^7$ g/mol [76]. The full lines represent second order density calculations, which have to be performed by multi-dimensional numerical integration. It is clear that the deviation for the viewed concentration range is maximally 10 % (10 c^* at small distances from the wall). This is of the same order as the total measurement error on the concentration and would hard to be resolved by a TIRM measurement.

Conclusion

A relatively good agreement between theory and experiment is achieved with the data delivered by the measurements. Still the system suffers from a fundamental flaw, the rods, sphere and wall have to interact via charge in order to do TIRM measurements. Yet the applied theory is strictly only valid for non charged system, not accounting possible influences of charge interaction. This might also be a reason why no effect of stiffness is visible. The electric double layer might be of the same order as the change caused by flexibility. On the other hand, the isotropic–nematic phase transition is still shifted drastically to lower concentrations for Y21M suspensions even at a low salt content. When comparing the TIRM results to earlier mea-

surements performed with line scanning tweezers by Lin et al. [45], these results cannot be reproduced. Lin et al. suggest a drastic difference between the theoretical description and the data, respectively a decrease in depletion, which is not found. The mismatch was attributed to flexibility of the rods and the measured potentials were only in agreement with a model describing rods incorporating flexible joints [78]. They also reported partial adhesion of rods at hight salt concentrations, which are inaccessible here.

4.2.2 Behaviour at higher fd concentrations

According to the numerical calculations seen in Figure 4.9(b) the simple model used to fit the depletion potential should hold for concentrations approximately up to 0.76 mg/ml. Doing measurements with the same experimental parameters as in the last section at fd virus concentrations over 0.25 mg/ml still shows an increase of the potential depth. But while a fit of the model function (eq. 4.1) still describes the data points well, the resulting concentrations are roughly twice as high as those determined by UV–Vis spectroscopy. This actually means that the potential is deeper than predicted by the theory. Surprisingly, this change of behaviour is rather discreet or so it seems. One hypothesis to explain this behaviour is the formation of a lose network of the rods, which would lead to some hybrid state of depletion and viscoelastic behaviour of the network, giving rise to a different potential.

In order to check for the possibility of the presence of a network, in addition to $R = 1.5$ μm spheres, two more sphere sizes are used and measurements at various fd concentrations are performed. The conditions are chosen to be equal to the already performed experiments, namely 2 mM Tris-HCl buffer at pH = 8.2, room temperature, small trapping strengths and charge stabilized polystyrene beads of the same brand, but smaller size. In Figure 4.11(a) the results of all potential measurement fits for $R = 1.5$ μm, $R = 1$ μm and $R = 0.5$ μm are shown. There the fitted concentrations are plotted against the actual concentrations of the fd virus solution, as determined by UV–Vis spectroscopy. Under ideal conditions the slope should be one or in other words the fitted concentrations should agree with independently determined ones. But the fit concentrations for the smaller sphere sizes seem to be generally overestimated. This is a result of the Derjaguin approximation. The rods have to be considerably smaller than the sphere diameter in order for the approximation to work properly. As soon as $D \approx L$ (sphere diameter becomes comparable/smaller than the rod length) there are actually fewer excluded orientations for a rod near a sphere than for a rod near a wall, effectively overestimating the entropy gain and thereby the potential depth, respectively the concentration [95]. But as can be seen, this is only a minor issue. Above a certain concentration, i. e. 0.25 mg/ml for the $R = 1.5$ μm spheres, there seems to be some kind of jump, increasing the fitted concentration

to values which can no longer be explained by a violation of the Derjaguin approximation. The jump is shifted to higher concentrations for the R = 1 μm spheres and is not visible anymore for the smallest investigated sphere size (R = 0.5 μm). The smallest sphere size may display the same transition at a concentration, which is no longer accessible by TIRM, because the interaction forces are already too high. Most of the measurements are performed with the stiffer Y21M virus. To show once again that there is no discernible difference, even at higher mass concentrations, between the wild type and Y21M virus, there are also some points for wild type fd given in Figure 4.11(a). The dependence of the transition concentration, above which the model starts to fail, on the sphere diameter may be seen as an indication that there is indeed some kind of network formed, which influences the depletion interaction, as soon as the mesh size becomes of the order of the sphere diameter. This is different from what was reported by Helden et al. for charged bohemite rods [46]. Helden et al. state an increase of the potential depth in charged rod systems by decreasing the salt concentration, but no change of behaviour above a certain number density of the employed silica coated bohemite rods is mentioned. The bohemite rods, having a length of L = 203 $\pm$ 93nm and a diameter D =18 $\pm$ 3 nm, are also much thicker and shorter than fd virus. For such depletants it is clear that changing the salt concentration has a more profound effect on the depletion interaction. The growth of the rods' double layer with decreasing salt concentration causes the shape of the rods to become elliptical, changing the depletion behaviour.

If the hypothesis of a rod network would be true, the diffusion of the sphere would be expected to be slowed down considerably, once the jump concentration is exceeded. One way to determine diffusion near a wall from TIRM data has been described in section 3.4. Following the given procedure and choosing a time window of one second, while using a sampling time of 2 ms, the short time diffusion may be calculated. The results of the diffusion measurements are presented in Figure 4.11(b) and the actual values given in table 4.1 together with the results of the potential fits. The values in the plot are normalized to D_0, the diffusion coefficient of the corresponding sphere size at zero fd concentration. According to the Stokes–Einstein relation $D = k_B T/6\pi\eta R$, the diffusion will only depend on an increase of viscosity, η, for purely viscose solutions when normalized to the diffusion without fd. This means all curves should fall onto each other, except the particles stop interacting only via friction/collisions, thereby violating the Stokes–Einstein relation. In the plots no violation is visible, presenting a purely viscose behaviour. There is some variation, but this is due to the error on the data and the calculation of the diffusion coefficient. Only a few points of the actual correlation function can be used, which makes the method less than perfect. But even for high concentrations, there is no sign of a network. All spheres show essentially the same diffusion behaviour – in contrast

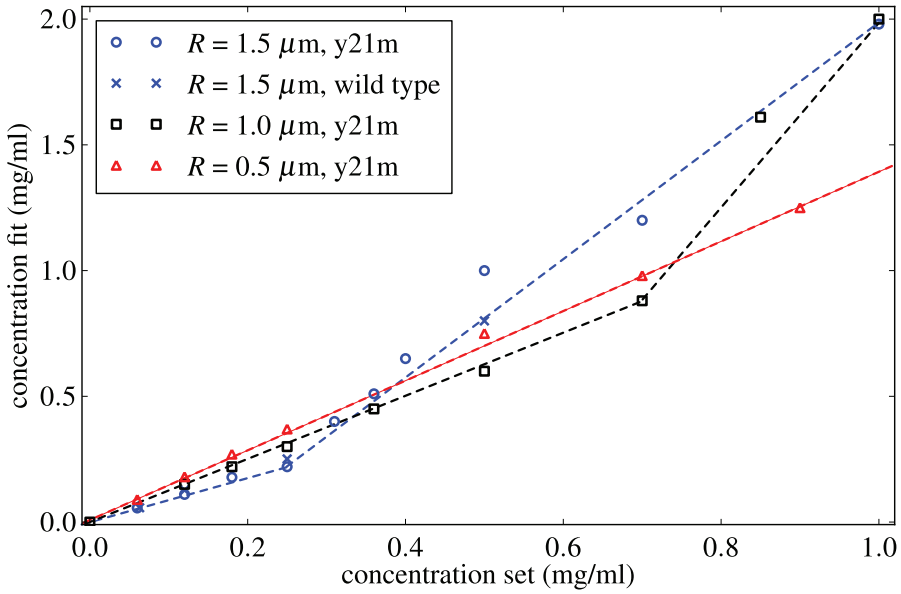

(a) summary of all fitted concentration determined for various real concentrations

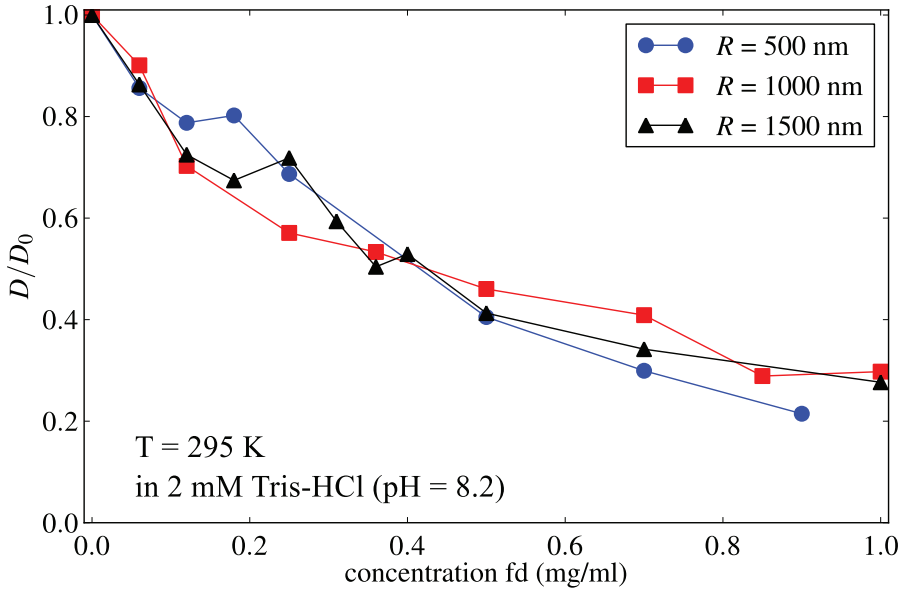

(b) near wall diffusion coefficients calculated from TIRM data for different spheres sizes

Figure 4.11: *(a) shows all fitted concentrations against those determined by UV–vis spectroscopy. The Derjaguin approximation causes the concentrations to be generally overestimated for sphere sizes of the order of the rod length and below. Above a certain concentration there seems to be a change of behaviour, yielding too high concentrations for the fits (too deep potentials, no effect of a violation of the Derjaguin approximation). (b) shows near wall diffusion normalized to the diffusion coefficient without fd virus. No change of behaviour can be seen over the whole concentration range.*

$2R$ (μm)	c_{set} (g/l)	c_{fit} (g/l)	D (m^2/s)
3	0.06	0.056	4.31×10^{-15}
3	0.12	0.11	3.72×10^{-15}
3	0.18	0.178	3.13×10^{-15}
3	0.25	0.22	2.91×10^{-15}
3	0.31	0.4	3.10×10^{-15}
3	0.36	0.51	2.56×10^{-19}
3	0.4	0.65	2.17×10^{-15}
3	0.5	1	2.28×10^{-15}
3	0.7	1.2	1.78×10^{-15}
3	1	1.98	1.47×10^{-15}
2	0.12	0.15	1.19×10^{-15}
2	0.18	0.22	9.95×10^{-15}
2	0.25	0.3	8.96×10^{-15}
2	0.36	0.45	6.99×10^{-15}
2	0.5	0.6	5.68×10^{-15}
2	0.7	0.88	5.31×10^{-15}
2	0.85	1.61	4.48×10^{-15}
2	1	2	4.07×10^{-15}
1	0.06	0.09	2.87×10^{-15}
1	0.12	0.18	2.96×10^{-15}
1	0.18	0.27	3.29×10^{-14}
1	0.25	0.37	2.82×10^{-14}
1	0.5	0.75	2.59×10^{-14}
1	0.7	0.98	2.63×10^{-14}
1	0.9	1.25	2.26×10^{-14}

Table 4.1: *Overview over all fitted concentrations and diffusion coefficients near the wall of the probe sphere as determined by analysis of the raw TIRM data. The diffusion is given corresponding to the sphere diameter $2R$ and the set fd concentration c_{set}.*

to the potential measurements. A reason why there is no visible effect might be that only the initial slope of the correlation function can be used as an estimate for the diffusion coefficient of the probing sphere near the wall. In case of a network, the particle would be trapped in a cage of surrounding rods and only break this cage with a certain probability or after a certain sojourn time. So the probed time scale is too small and the diffusion appears to be free diffusion. One idea to overcome this problem was to do standard dynamic light scattering in bulk on fd suspensions mixed with the investigated spheres of certain size. But unfortunately the spheres used for the TIRM experiments are to large for dynamic light scattering experimnents, so that no ensemble can be measured. This makes the results unreliable.

Other independent ways, offering nearly the same sensitivity as TIRM, to map out the interaction potential between a sphere and a wall or between two sphere are sparse. Still other methods to look for the existence of a network need to be considered. There is the method used by Lin et al. [45] using laser tweezers, which was already briefly discussed. But the TIRM setup is not suited for such experiments and therefore it was not possible to recreate these experiments. An indirect way would be to do micro rheological measurements or standard rheological measurements to look for an effect. A literature check shows that fd suspensions have already been extensively studied by standard rheological means by Graf et al. [96] Nevertheless, a simple test measurement of the viscosity is performed in order to yield some insight and most of all an idea if it is feasible to measure the effect in bulk with the compared to TIRM rather insensitive rheological measurements.

For this purpose the viscosity of Tris–HCl buffer suspension containing different amounts of fd virus is determined using a falling ball micro viscometer (Anton Paar AMVn–micro viscometer). It uses a steel ball in a capillary filled with solution of interest. In order to determine the viscosity the falling time of the steel ball inside the liquid–filled capillary is measured at a defined angle with respect to the gravitational field and over a given distance. If the density of the solution and some empirical constant for the capillary (diameter 1.6 mm for the performed experiments) is known, the viscosity may be calculated from the falling time. For all measurements the density of the pure buffer is used, neglecting the influence of the addition of fd virus, since it only changes by 0.2 percent when the concentration of fd is increased from 0 to 0.6 mg/ml (see Figure 3.14). Looking at the result in Figure 4.12 the viscosity increases linearly with the concentration and there is no sign of any transition or abrupt change – as suggested by the potential measurements. In agreement with the work of Graf et al. this result shows that it is questionable if rheological measurements would provide any further insight into the observed transition. Maybe micro rheological measurements close to the wall would be sensitive enough to provide a measurement method, which could allow

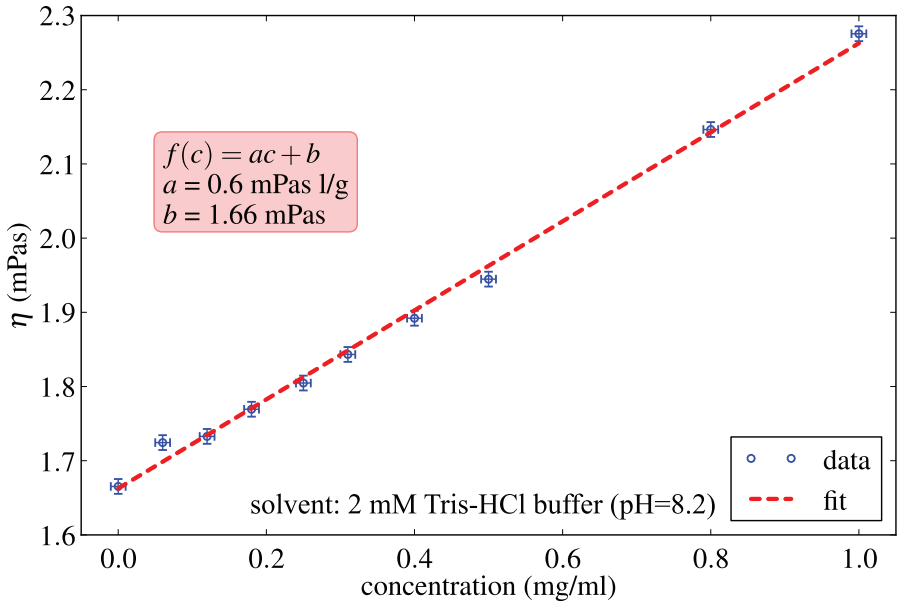

Figure 4.12: *Increase of viscosity by addition of Y21M. The viscosity increases linearly and there is no sign of discontinuity. The viscosity of the pure solvent is considerably higher than that of water, which is a result of the ethanol content.*

to see an effect. This leads immediately to the next question if the observed deepening of the potential is only present near a surface or in the bulk, too. This is still unclear and cannot be solved by TIRM experiments alone.

4.2.3 Reevaluation of fd depletion data with a modified approach

In the last section it has been shown that the simple first order depletion model for rigid, thin rods breaks down above a certain mass concentration of fd. But even for low concentrations of fd virus, there is a deviation between measured energies and the theory at small distances from the wall. This deviation was attributed to non perfect referencing. Nevertheless, the effect becomes more pronounced when going to deeper depletion potentials. It might be worthwhile to give the data points at small distance some additional consideration in order to gain a better idea about the behaviour at high depletant concentrations.

Depletion potentials covering the full accessible range of separation distances are shown in Figures 4.13(a), 4.13(b) and 4.14(a). There the depletion potentials for all investigated sphere sizes are shown. The presented measurements are not necessarily the same as in section 4.2.2, but were conducted in the exact same way. Of course the data at the edges of the range

are not really reliably due to poor statistics. But for the moment this shall be ignored. At distances smaller than 80 nm the potential clearly takes on a different shape. One might see that the shape in this region describes a parabola. In order to use this in a tentative functional description of the depletion data, a model function is sectionally defined, showing the expected depletion behaviour (eq. 4.1) at long distances and a quadratic dependence at short distances (see eq. 4.2).

$$\frac{\tilde{W}_{dep}^{SW}(h)}{kT} = \begin{cases} W_{dep}^{SW}(h) & \text{for } h \geq \tilde{h} \\ -k\,(h-h_0)^2 + \tilde{W}_{dep}^{+} & \text{for } h < \tilde{h} \end{cases} \tag{4.2}$$

With this modification the data are fitted again with c_{fit}, k and W_{dep}^{+} as free fit parameters. The results of these fits are given in Figures 4.13(a), 4.13(b) and 4.14(a) as red lines. Rod length L, temperature T, sphere radius R and molar mass M_{rod} are kept constant at the independently determined values. The parameters $\tilde{h}$, h_0 and $\tilde{W}_{dep}^{+}$ are chosen manually to yield the best result, but are not part of the fitting procedure. It is obvious that the measurement at small separation distances is now described virtually perfectly. Still there is no physical reasoning behind a quadratic energy dependence – at least there is none, which can be proven. With the hypothesis of a temporary rod–network, it is possible that the network behaves like a mechanical spring, showing elastic behaviour. In this case, a quadratic dependence were expected. Yet it is unclear why this should only happen at short distances. Looking at all the presented data the effect seems clearer for the smaller probing spheres. But this is just an effect of the scaling. The quadratic behaviour is visible for all sphere sizes. For moderate concentration the potential becomes repulsive at small distances, while for high concentrations there seems to be another contribution, which is strongly attractive.

Most likely this is van der Waals attraction, which is not accounted for. At concentrations, at which the attraction is no longer explained by the depletion model (high concentrations), also the parabolic behaviour seems to be less pronounced. So again, the model fails completely. But just before this happens, at not too high concentrations, there always seems to be a region in between the large and the small separation distances, where none of the two functional forms fit the data. This intermediate region appears to grow with increasing depletant concentration. The results of all fits, giving all parameters, are shown in table 4.2. The concentrations derived from eq. 4.1, aside from small differences, still agree with the fits made in section 4.2.2, where only one model was considered. The behaviour of the quadratic part is inconclusive. The spring constant, k, increases with increasing fd concentration (see Figure 4.14(b)) and then seems to decrease again. Probably this is because the potential doesn't really exhibit a parabolic shape anymore at higher concentrations. The size of k appears to

D (μm)	c_{set} (g/l)	c_{fit} (g/l)	k (μN/m)	W^{+}_{dep} (k_BT)	$\tilde{W}^{+}_{dep}$ (k_BT)	$\tilde{h}$ (nm)	h_0 (nm)
3	0.060	0.062	2.28	2.45	-0.53	89	57
3	0.120	0.117	4.64	3.17	-0.61	95	52
3	0.250	0.222	7.05	8.29	-0.64	85	58
3	0.360	0.536	19.52	13.62	-2.42	85	58
3	0.500	0.833	75.80	29.92	-9.73	40	20
2	0.060	0.066	1.53	1.71	-1.07	119	42
2	0.120	0.147	3.60	3.20	-1.92	98	40
2	0.250	0.326	5.59	7.37	-0.91	100	68
2	0.360	0.53	12.83	12.67	-1.80	90	60
2	0.500	0.66	22.52	15.9	-1.12	90	70
2	0.700	0.89	11.18	21.61	-4.31	90	40
2	0.850	1.55	5.51	35.88	-1.81	90	40
1	0.060	0.080	2.28	0.72	-0.28	115	100
1	0.120	0.165	1.50	1.86	-0.19	100	85
1	0.180	0.236	1.45	2.58	-0.16	88	69
1	0.250	0.330	2.29	3.74	-0.23	85	75
1	0.500	0.557	6.38	6.95	-0.42	80	60
1	0.700	0.988	5.46	11.31	-0.79	95	65
1	0.900	1.265	7.33	14.89	-0.82	95	65

Table 4.2: *Parameters used for the fits in figures 4.13(a), 4.13(b) and 4.14(a). $\tilde{h}$ and h_0 are no free fit parameters being adjusted manually to yield the best result.*

be proportional to the square of the sphere radius R^2. Furthermore, some of the fits at low distances do not really describe a parabola. In some cases the potential becomes extremely deep and while the data may still be fitted, the spring constant will be severely overestimated. So while the overall behaviour seems to be consistent for all investigated sphere sizes, this might still be just a coincidence.

Conclusion

Since the model purely empirical there is only little to be learned from this in terms of the structural properties of the rods. Yet it reveals that the potential cannot be explained by a pure depletion model alone if false referencing is ruled out. It might be that this is another artifact caused by the use of charged rods and spheres, but there is no direct way to check this with TIRM.

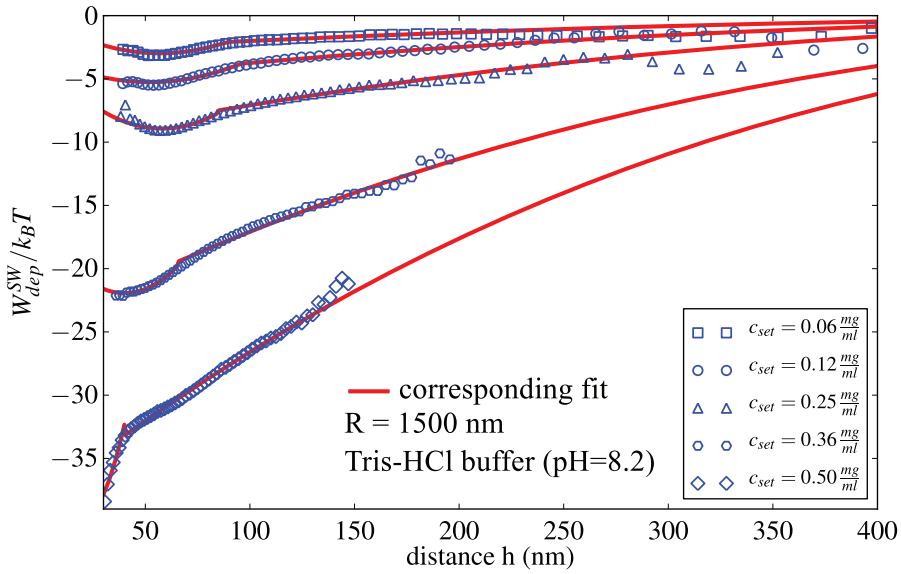

(a) Refitted potentials for R = 1500 nm spheres

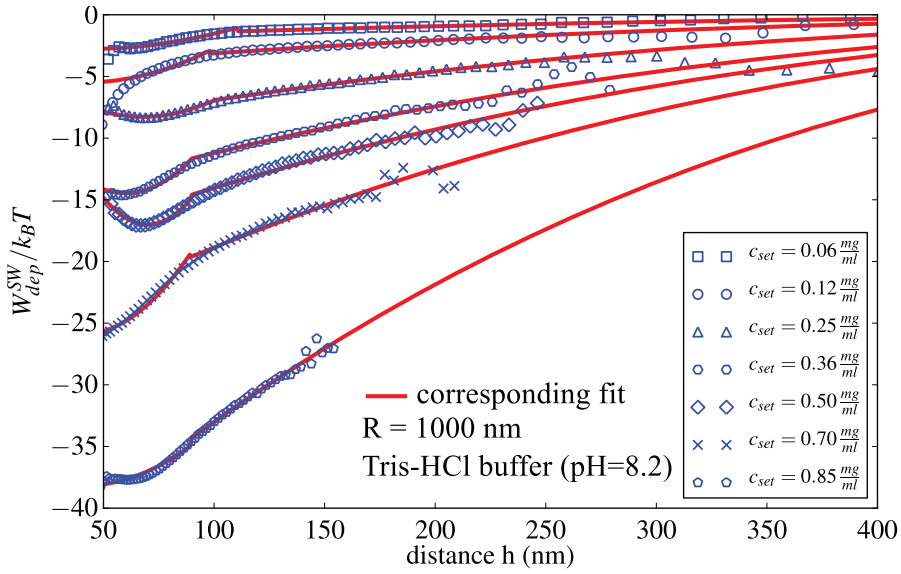

(b) Refitted potentials for R = 1000 nm spheres

Figure 4.13: *In (a), (b) potentials over the full measured range and with the corresponding modified fits are shown for R = 1500 nm and R = 1000 nm polystyrene spheres. Some of the fits are not reasonable because the potential is no really harmonic at small distances.*

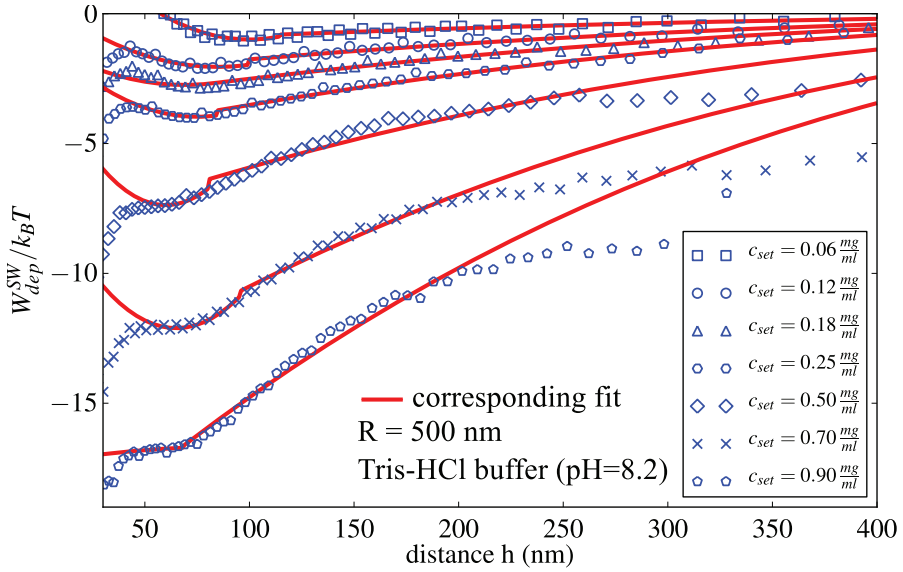

(a) Full range of measured depletion potentials for R = 0.5 µm sphere at different concentration with corresponding fits

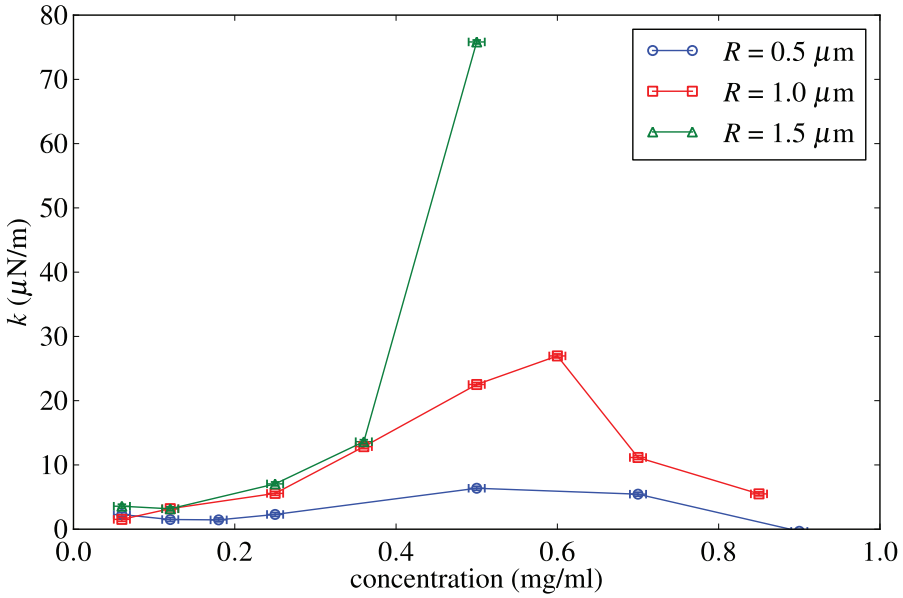

(b) Change of the spring constant k with growing fd concentration for various spheres sizes

Figure 4.14: *In (a) potentials over the full measured range and with the corresponding modified fits are shown for R = 500 nm polystyrene spheres. (b) the fitted spring constants of the harmonic part are plotted versus the concentration. It has to be remarked that some of the fits are not reasonable at small distances.*

4.2.4 Rod induced depletion in a shear flow

This part will discuss depletion potentials measured in a shear gradient. For the first experiment, as before, a quartz glass cell flow cell is used to generate a shear field, but now no optical tweezers or the PMT is used. Like in the previous section the HeNe–laser is used as an illumination source and the penetration depth, β^{-1}, is set to 150 nm. The flow cell has a thickness of d = 2 mm and for data acquisition the camera, as explained in section 3.2.5, is employed. With the help of particle tracking it is possible to observe many particles at the same time and measure an ensemble potential. The measurement is performed with $R = 3$ µm polystyrene spheres (thermo scientific,4206A) in 0.1 mM NaOH solution, while choosing the particle concentration to be high enough to have a sufficient number of particles in the field of view and flowing solution through the cell. The illumination time of the camera is set to 20 ms, but the actual sampling time is considerably higher due to the time it takes to transfer a picture from the camera to the computer. This experiment is done without any depletant and serves as an experimental check if the potential of a particle solely interacting via electrostatics and gravitation stays unaffected by the shear field. The results are shown in Figure 4.15. The flow induces a shear rate of $\dot{\gamma} = 0.86$ 1/s. When doing flow experiments with many particles, the referencing becomes kind of ambiguous and the absolute distance is hard to determine. While the size and the shape of the particles is very well defined, the carried charge appears to vary. This might also explain the stronger variation in the repulsive branch of the two measured potentials. Overall these potentials are identical. The loss in accuracy is expected due to the averaging.

For the next step, in which the rod–like depletant will be added, some simple idea of how the depletant will be influenced by the shear field is required. For rods it is known that they align in a shear field [97]. The rods are of microscopic dimensions, which means they undergo Brownian motion. In effect, the rod will move through the volume in a random fashion, which is called translational diffusion. Corresponding to this nomenclature the rotational motion of the rod, caused by collisions with the surrounding molecules, is called rotational diffusion. In order to align a rod, the shear rate has to be equal or higher than the rotational diffusion coefficient. The rotational diffusion coefficient for perfectly rigid, long, thin rods (high aspect ratio) can be calculated in an analytical way. In order to do this, the Langevin equation for a rod has to be solved, which is a lengthly task. For brevity's sake only the result will be given and for a thorough derivation the reader may be directed to the book of J.K.G. Dhont [98].

$$D_r^{\perp} = \frac{k_B T}{\pi \eta L^3 / (3 \ln (L/D_{rod}))} \tag{4.3}$$

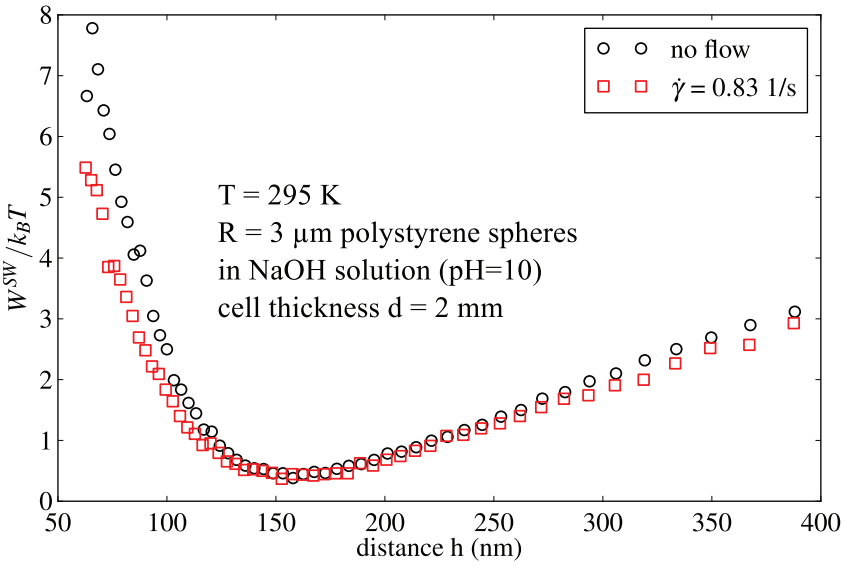

Figure 4.15: *Comparison of a potential measured under flow and one without flow. There are small deviations, but overall the potentials agree. The beads are suspended in a 0.1 mM NaOH solution.*

The rotational diffusion coefficient, $D_r^{\perp}$, depends on the rod dimensions and the solvent properties: diameter D_{rod}, rod length L, the viscosity of the solvent η and the temperature, T, of the system. Calculating the rotational diffusion for a rod with the dimensions of fd virus, in a solvent with a viscosity η = 1 mPas and at T = 295 K, yields D_r = 27.7 1/s. A shear rate higher than this value cannot be achieved by employing a flow cell with a thickness d = 2 mm ($\dot{\gamma}_{max}$ = 5.6 1/s). In order to shear align fd, higher shear rates are required. This can be accomplished by either increasing the flux, which is limited by the valve, or by using a thinner flow cell. Using a cell with a thickness of d = 0.1 mm and otherwise identical dimensions, the maximum achievable shear rate goes up to $\dot{\gamma}_{max}$ = 987.7 1/s.

Now, an idea of what might happen to the depletion interaction is required when the rods are aligned by the shear field. Assuming that the sphere does not severely perturb the flow field, the perceived dimensions of the rods will shrink (see Figure 4.16). The rods stop sampling all the available orientations and by that the excluded for the rods shrinks. Consequently, the effect of depletion will be decreased or in other words the potential is believed to become more shallow. Admittedly, this is a very simple picture. Yet more complex considerations immediately necessitate numerical simulations, which only yields limited physical insight. For the experiment R = 1.5 µm polystyrene spheres (thermo scientific, 4203A) in Tris-HCl buffer (pH = 8.2) are chosen, since the depletion effect on the R = 3 µm spheres is already so

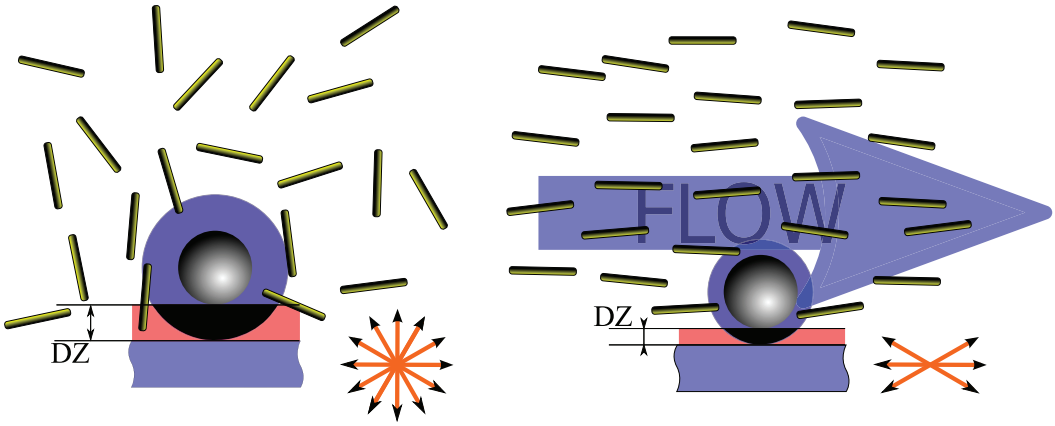

Figure 4.16: *As soon as the rotational diffusion of the rods is suppressed by the shear gradient, the rods are supposed to align in the sketched way. The depleted volume shrinks, since the configurational freedom of the rods is already restricted by the flow field.*

large that it gets hard to measure with TIRM. But the smaller spheres make it hard to observe potentials without any depletion present, because the particles often escape (without tweezers) the illumination field, i. e. are too far away from the wall to be seen. The resulting free potentials are very noisy. In order to be able to align the fd virus, the thinner flow cell (d = 0.1 mm) is used. Still there is no influence of the higher shear gradient on the interaction potential of a probe particle, unaffected by depletion when using the thiner cells (experimental proof in section 4.3.4). Performing the experiments at an fd concentration of c_{set} = 0.12 mg/ml is very disappointing at first glance (see Figure 4.17(a)). There is almost no difference between a potential measured under flow and the one measured in a quiescent state. Going to higher shear rates has no real effect on the potential. For the chosen sample, it should even be slightly easier to align the viruses as for rods in water due to the higher viscosity of the buffer containing 15 % ethanol. Taking a look at the potentials at longer separation distances still hints to some small difference. The potentials recorded under shear are a tad deeper (the slope of the right branch increases). Yet this effect is so small that it may just be an artifact and is well within the experimental resolution of the TIRM method. The used concentration of 0.12 mg/ml worked well for the measurements in rest, but is already above the overlap concentration c^*. That might be the reason why no effect can be seen. The suggested simple model may not apply anymore, since the rods may hinder each other's alignment. So the experiment is repeated at different concentrations. Going to higher concentrations presents, as expected, the same results, meaning no discernible difference between shear and no shear. As stated, this could be a result of the rods already overlapping.

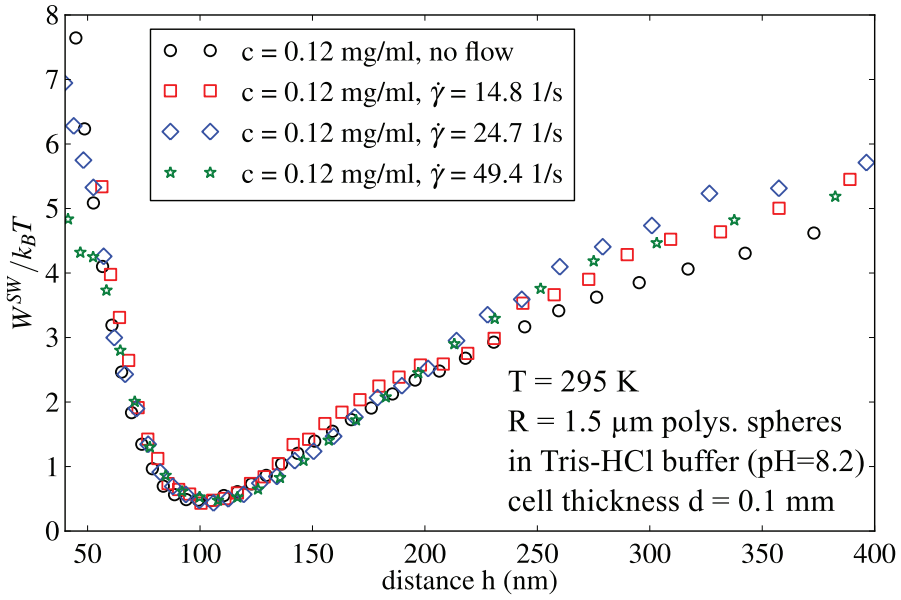

(a) Flow affected potentials for R = 1500 nm spheres with c_{set} = 0.12 mg/ml fd virus

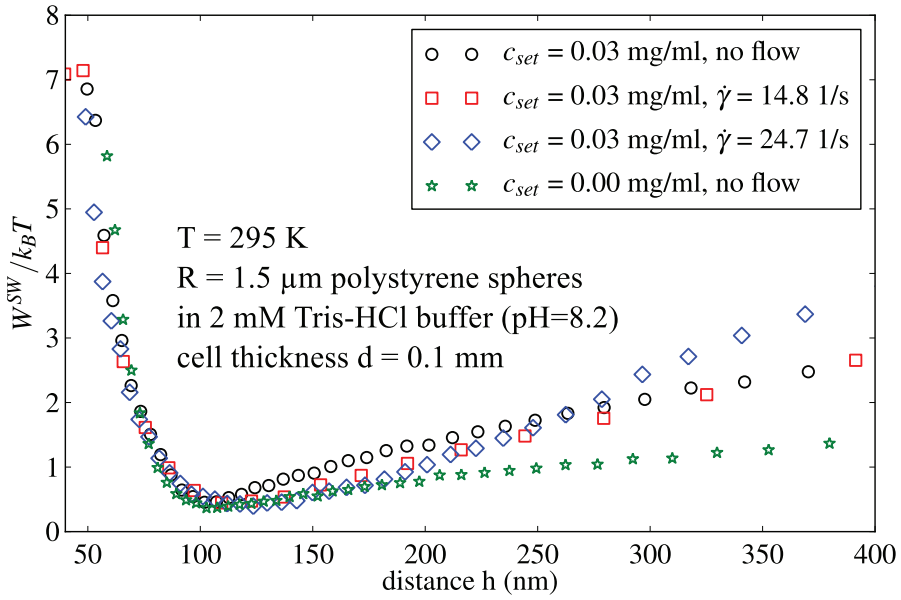

(b) Flow affected potentials for R = 1500 nm spheres with c_{set} = 0.03 mg/ml fd virus

Figure 4.17: *In (a) and (b) full interaction with fd virus present above and below the overlap concentration is shown. Small changes to the flow effected potentials are visible, but are of the same order as the measurement error.*

Therefore, a very low fd concentration, c_{set} = 0.03 mg/ml, is checked. In the potentials, shown in Figure 4.17(b), some kind of influence appears to be visible. When a shear field is applied, the potential depth is decreased (the slope of the right branch decreases). A reference without flow for a potential with fd virus and one without is given. Nevertheless, the overall effect of depletion is already very small and the observed change may still be some kind of error on the measured data points. Furthermore, no absolute distances were calculated for the shown potentials. They are all shifted to overlap with their repulsive branches.

Conclusion

Shear aligning fd virus happens to be more difficult than expected. The behaviour at high concentrations comes as somewhat of a surprise. Since there are no earlier studies on sphere–wall interaction potentials influenced by a shear gradient, it is hard to speculate what causes the potentials to stay practically unchanged. The assumption of a network at small distances could deliver a way to explain the behaviour here, too. Again, it could be speculated that the rods form a loose network close to the wall and the shear gradient strengthens this network, causing it to envelop the probing sphere. But up to this point, this is mere speculation. Shorter rods such as shorter viruses (M13cp) [99] and longer ones (M13) [93] could help to shed some light on this problem. Unfortunately, culturing and cleaning these viruses turned out to be very time consuming and has not yet been successfully done.

4.3 Depletion caused by hard, polydisperse platelets

In this section the depletion effect of moderately polydisperse platelet suspensions will be investigated. The platelets are smaller than the fd viruses, therefore allowing to sample the full depletion potential by TIRM. This somewhat fills the gap left by the lack of shorter viruses. Another point is that platelets could possibly be aligned in a shear gradient in contrast to the rods. This means the platelets might offer a substitute to investigate shear affected potentials. Again, first measurements without flow are performed in order to compare those measurements to the ones performed in a shear field. Yet the polydispersity sets a bit of a challenge. The theory discussed in section 2.1.4.2 by Piech and Walz for monodisperse circular thin platelets is not immediately applicable. But it may be extended, to account for polydisperity by averaging over a distribution of particle sizes. Measurements with tweezers turned out to cause problems, because the suspensions are slightly turbid. Therefore, another measurement mode using fluorescent particles is used to alleviate the problem of turbidity. This kind of

experiment is called TIRF (total internal fluorescence microscopy) (see section 3.2.6) instead of TIRM. The experiments without flow are the first to measure depletion caused by a plate–like depletant and the results agree well with the modified theory. Measurements under flow show indeed the expected behaviour of a vanishing depletion potential above a certain shear rate. Yet only up to a certain platelet concentration. At higher concentrations the observed potentials become similar to those measured with fd virus.

4.3.1 Extending the depletion model

The depletion potential for monodisperse, perfect, hard circular platelets was already mentioned in section 2.1.4.2.

$$-\frac{W_{dep}^{SW}(h)}{kT} = \begin{cases} \frac{2}{3}\pi\rho_N R D^2 f(h,D) & \text{for } h \le D \\ 0 & \text{for } h > D \end{cases} \tag{4.4}$$

$$\rho_N = \frac{c_{plate} N_A}{M_{plate}}$$

$$f(h,D) = \left[\frac{3}{2}\frac{h}{D}\arcsin\frac{h}{D} - \frac{3}{4}\pi\frac{h}{D} + \left(1+\frac{1}{2}\left(\frac{h}{D}\right)^2\right)\sqrt{1-\left(\frac{h}{D}\right)^2}\right]$$

In this expression for the depletion potential [62, 100] caused by platelets, the platelets are regarded as infinitely thin discs with diameter D. The platelet concentration is given by c_{plate} in units of mass per volume, N_A is Avogadro's number, $M_{plate} = \rho_{gibb} L \pi D^2/4$ the platelets' molar mass, and R is the radius of the probe sphere. Strictly, this formula is only valid for monodisperse platelets. For the experiments here this is not the case. That means the given equation has to be modified to account for a distribution $S(D)$ of platelet sizes. Any variation of the thickness of the real platelets is neglected, since it does not contribute significantly to the theoretical potential. To get an expression for polydisperse platelets, the potential in eq. 4.4 is averaged with respect to a size distribution, while assuming that the platelet size follows a log normal distribution,

$$S(D,\bar{D},\sigma_D) = \frac{1}{\sqrt{2\pi}\sigma D}\exp\left(-\frac{(\ln D-\mu)^2}{2\sigma^2}\right) \tag{4.5}$$

$$\sigma = \sqrt{\ln\frac{{\sigma_D}^2}{\bar{D}^2}+1} \tag{4.6}$$

$$\mu = \ln\bar{D}-\frac{\sigma^2}{2} \tag{4.7}$$

where $\bar{D}$ is the expectation value of the disc diameter and σ_D is the corresponding standard deviation. To get a mean depletion potential this distribution is convoluted with the potential for a monodisperse system:

$$\bar{W}^{SW}_{dep}(h) = \int_0^\infty S(D,\bar{D},\sigma_D)W^{SW}_{dep}(h,D)dD \tag{4.8}$$

To average the potential, the total particle number density ρ_N is required. However, it is not directly accessible because only the concentration c_{plate} of a polydisperse system is measurable, which only gives the mass of all particles in solution independent of their size.

In order to calculate the total particle number density the fact that the size distribution is connected to the mass distribution [101] is exploited. The mass of one particle is given by $m_i = \pi(D/2)^2 L\rho_{gibb}$, where L is the thickness of a platelet and ρ_{gibb} the mass density of gibbsite. The total mass concentration is described by

$$c_{plate} = \sum_{i=1}^{N} c_i = \frac{1}{V}\sum_{i=1}^{N} m_i = \frac{4\pi L\rho_{gibb}}{V}\sum_{i=1}^{N} D_i^2 \tag{4.9}$$

while knowing that $D_i = D_i - \bar{D} + \bar{D}$ and the definition of σ_D^2 this reduces to

$$c_{plate} = \frac{N\pi L\rho_{gibb}}{4V}(\bar{D}^2+\sigma_D^2) \tag{4.10}$$

which yields:

$$\rho_N = \frac{4c_{plate}}{\pi L\rho_{gibb}(\bar{D}^2+\sigma_D^2)}. \tag{4.11}$$

Now that all contributions are known the integral expression makes it possible to fit data measured from a polydisperse system. By use of a Levenberg–Marquardt fitting algorithm, $\bar{D}$ and σ_D can be derived for a given concentration c_{plate} and a material density ρ_{gibb}.

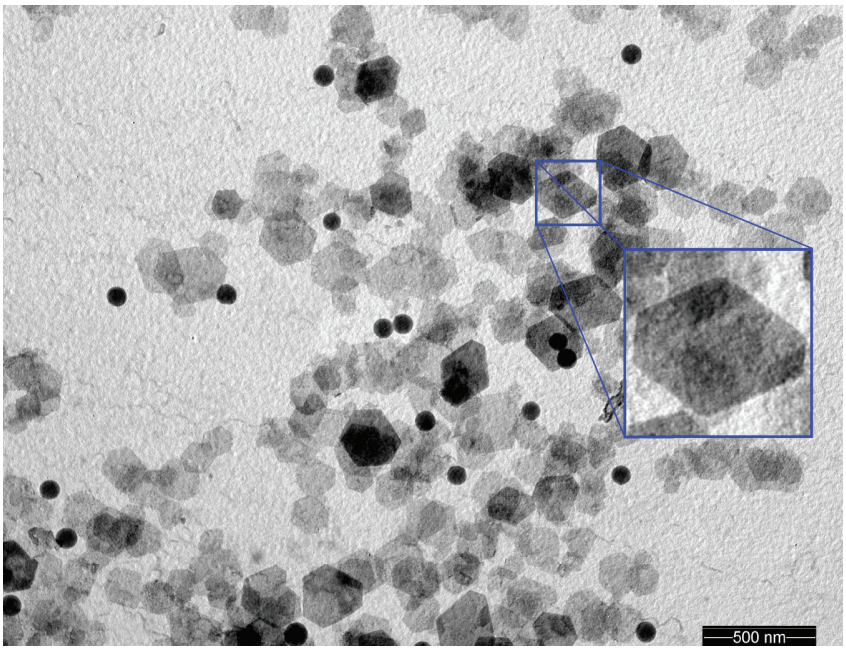

Figure 4.18: *TEM picture of platelets dried on a carbon coated copper TEM–grid together with polystyrene norm–spheres with R = 50* nm. *One of the platelets is magnified. The platelets have an irregular hexagonal shape. Multiple pictures are taken to determine the size distribution of the platelets.*

4.3.2 Characterizing platelets by TEM measurements

Since the platelets are not of biological origin the polydispersity is much higher than for viruses. Also the size varies from synthesis to synthesis, which requires to check the particle size for each batch.

Therefore, TEM measurements are carried out with a Phillips CM200 at an acceleration voltage of 160-200 kV. The samples are prepared by dip–coating carbon coated copper TEM grids in a highly diluted platelet suspension. The grids are dried at room temperature.

The measurements serve also as an additional check, whether the platelets are free of aggregates and to acquire knowledge of the size distribution. A small number of well defined polystyrene spheres with a diameter of 100 ± 4.5 nm are added to the platelet suspension to achieve higher accuracy of the analysis (Figure 4.18).

Collecting particle sizes from a number of images yields the distribution, which is shown in Figure 4.19, together with two continuous distribution curves. The latter have been calculated, assuming a logarithmic–normal distribution (eq. 4.7) using the values for $\bar{D}$ and σ_D

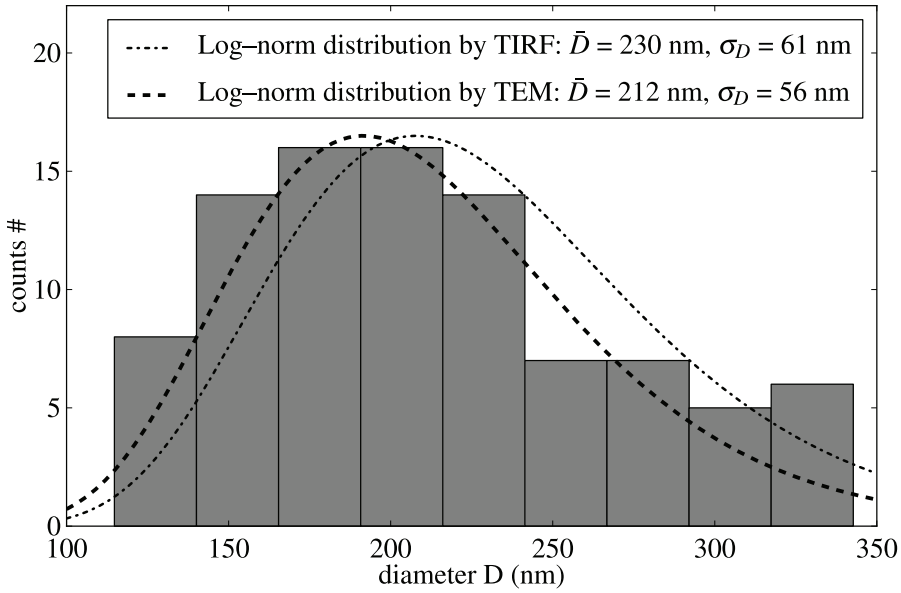

Figure 4.19: *Size distribution, found by TEM–measurements, represented by the histogram and the dashed curve. The shape of the distribution justifies the assumption of a log–normal distribution. For comparison, the size distribution found by TIRF is plotted as the point–dashed curve.*

as determined from TEM image analysis and TIRF measurements, respectively (see section 4.3.3).

The two calculated distribution functions describe the experimental histogram, with regard to the large statistical errors of the experimental data, equally well. Further, it may be concluded that a log–norm distribution is appropriate to describe the size polydispersity of the gibbsite platelets.

Some particles are overlapping, but in none of the pictures can real aggregates be found. So it may safely be assumed that depletion in the TIRF experiments is only caused by singular objects and not by aggregates. For the analysis of the TIRF data, the irregular hexagonal particles will be approximated as circular cylinders with the tips of the hexagon touching the bordering circle. This leads to a discrepancy in shape between model and real particles, resulting in a 17 percent volume difference when assuming regular hexagons.

4.3.3 TIRF measurements on platelets in quiescent suspensions

In order to measure a pure depletion potential, a reference potential of bare spheres without any depletant present has to be measured first. Data acquisition is performed by TIRF, namely

by usage of the CCD camera and a 440 nm diode laser as illumination source. The penetration depth, β^{-1}, is set to 150 nm and R = 2.5 µm green fluorescing polystyrene beads (thermo scientific, G0500) are used as probe particles. The data is extracted by processing the image data with a particle tracking algorithm. The potentials of the bare spheres are fitted with the superposition of electrostatic interaction and a gravitational potential as in the previous sections. Subtracting this potential from measurements with platelets present gives again the pure depletion potentials $W^{SW}_{dep}(h) = W^{SW}(h) - W^{SW}_{ref}(h)$.

For the sake of clarity, it is imperative to note again that there is no way to measure absolute potentials. The energy values are always relative, without a given point of reference. For example, the potential could be declared to be zero at elevation zero. Yet this wouldn't be very instructive to visualize depletion potentials. Instead, to achieve better comparability, the zero value of the potential is ignored altogether and the gravitational branch is taken as a reference. Due to the finite range of the depletion interaction it is obvious that the potentials have to overlap for distances larger than some effective disc diameter. In this region, where the potential values coincide and W^{SW}_{dep} is zero, it is expected that the potentials exhibit the same shape, namely the same linear slope stemming solely from the gravitational force. Consequently, the shift in energy of all potentials is chosen such that they will have the same value in this region.

A further problem is that the refractive index of gibbsite, n = 1.58 [88], deviates sufficiently from water to create turbid aqueous suspensions at rather low concentrations. Using thin measurement cells (d = 0.1 mm) helps to alleviate that problem. Nevertheless, the turbidity of a sample with finite gibbsite platelet concentrations is large enough that a detectable amount of fluorescence light is absorbed/scattered by the suspension before leaving the sample cell, effectively decreasing the observed intensity. Therefore, data recorded in the presence of platelets cannot be referenced to the intensity, I^S_0, of a sticking sphere, leading to a systematic error in distance. The obvious solution would be to index–match the solvent and platelets. However, the current setup is limited to a maximum refractive index of the solvent of n=1.45, while gibbsite has a refractive index of n=1.58. Instead of modifying the setup and changing the sample environment, the problem is circumvented by exploiting the fact that the depletion potential is limited to a finite separation distance $\bar{D}$. Knowing the position of the reference potential minimum, for which referencing can be done due to the absence of platelets, and the size of the platelets, leaves only a single choice for the real distance–dependence of a potential when fitting the model.

Interaction potentials with and without depletion induced by silica coated gibbsite platelets between a green fluorescing probe sphere ($R = 2.5$ µm) in 1 mM NaOH solution and a wall are shown in Figure 4.20. The figure shows that the depletion parts of the potentials are very pro-

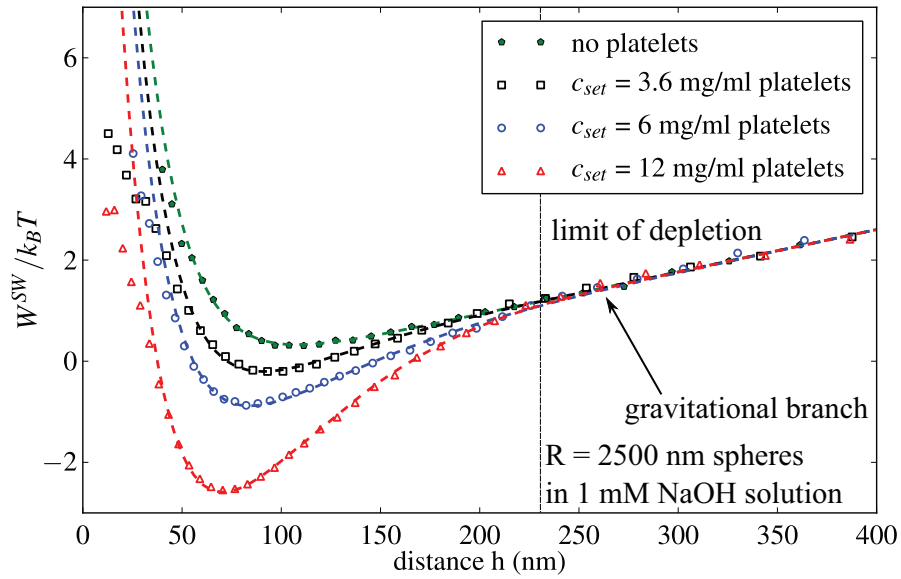

Figure 4.20: *Full sphere–wall interaction potentials for different platelet concentrations with corresponding fits, given as dashed lines. Potentials with depletion are shifted to match with the gravitational branch of the reference potential: for distances higher than the range of the depletion potential (limit annotated), the potentials have to overlap with respect to their gravitational branches.*

nounced for higher platelet concentrations. As previously discussed, the gravitational branch of all potentials has to be the same for distances higher than the range of the depletion interaction, namely for elevations greater than the disc diameter. Because only relative potentials are measured, the raw data have to be shifted in energy to be physically reasonable. The potentials in Figure 4.20 are shifted by -0.65 kT, -1.3 kT and -3 kT with respect to the reference potential and increasing concentration. The total potentials are displayed with corresponding fits, given as dashed lines. The data are well described by the provided model.

The model prefactor, $c_{fit}/L\rho_{gibb}$, is overestimated roughly by ten percent compared to the values which are calculated from L = 6 nm, ρ_{gibb} = 2.4g/cm^3 [88] and the mass concentration c_{set} determined by drying and weighing the stock solution. This is very likely due to the discrepancy in the particles' volume. According to the discussion in section 4.3.2 the volume is 17 % larger than if only regular hexagons are considered and the idealization of disc–like particle shape is used. Furthermore, the length, L, of the cylindrical platelets has an uncertainty, which cannot be quantified, while the mass density was confirmed by independent measurements (see section 3.6.2).

Pure depletion potentials, obtained by subtraction of the parameterized reference potential

from the experimental curves measured at finite platelet concentrations, are shown in Figure 4.21. The overall potential shape agrees with the theoretical prediction and the data is described very well by the fit of the theoretical model. The shape does not deviate significantly from the monodisperse case. Concentrations used to fit the data have to be set about ten percent higher than those determined by weighing due to the shape mismatch to achieve a satisfying result (see table 4.3).

A remarkable point is that the contact value doesn't change with polydispersity or disc diameter for a system of platelets, which is different from the findings with rods as depletant. This is explained by the applied model. For a monodisperse system the contact value is given by

$$W^0_{dep} = \frac{2}{3}\pi\rho_N RD^2 = \frac{8}{3}\frac{cR}{L\rho_{gibb}} \tag{4.12}$$

which is not a function of D. Even for polydisperse systems the contact value is independent of the particle diameter. This can easily be shown in an analytical way for a normalized, arbitrary distribution function ψ. By definition:

$$\tilde{\sigma}^2 = \int_0^\infty (x-\tilde{\mu})^2\psi(x)dx = \int_0^\infty (x^2 - 2\tilde{\mu}x + \tilde{\mu}^2)\psi(x)dx$$

$$\Rightarrow \int_0^\infty x^2\psi(x)dx = \tilde{\mu}^2 + \tilde{\sigma}^2$$

here $\tilde{\sigma}$ is some standard deviation and $\tilde{\mu}$ is the mean value of the distribution. With this general relation and eq. 4.11 it is obvious that

$$\begin{aligned} \bar{W}^0_{dep}(h) &= \int_0^\infty S(D,\bar{D},\sigma_D)W^0_{dep}(D)dD \\ &= \tfrac{8}{3}c_{plate}R/(L\rho_{gibb}). \end{aligned} \tag{4.13}$$

Except for the polydispersity in thickness there is no effect on the contact value. The thickness variation can mostly be neglected since the effect on the mass is less pronounced. The derivation shows that the contact value is also independent of type and shape of the size–distribution.

When comparing the distributions derived from the TIRF–measurements to those obtained by TEM image analysis, some potential error sources have to be considered. However, they are are difficult to quantify in detail. Slight sedimentation of the platelets inside the measurement cell over the course of an experiment increases the local concentration. The effect of this issue is rather small, which is seen when a set of spheres is observed over a long period of time. Having imperfect probe–spheres introduces yet another uncertainty into the data. Further error sources are: not strictly homogeneous illumination of the measurement cell and change of the

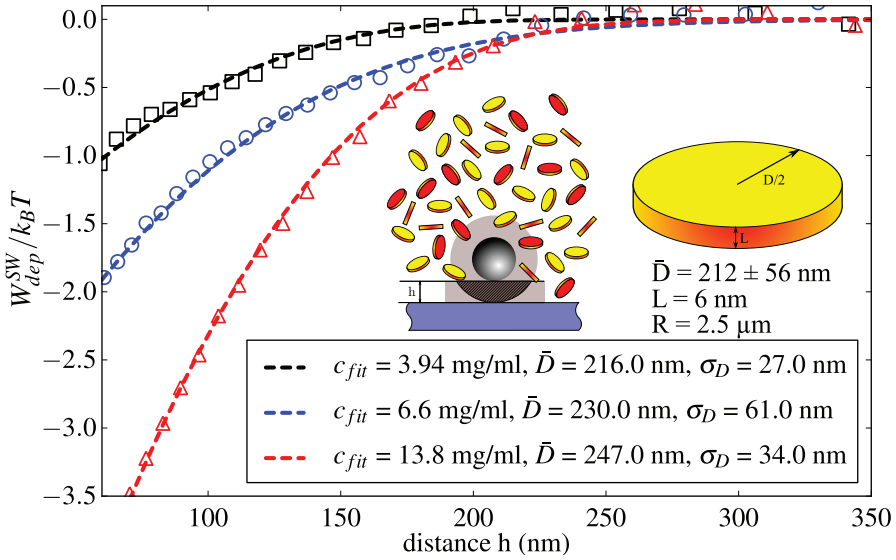

Figure 4.21: *Pure depletion potentials with corresponding fits for spheres (R_S = 2.5 µm) in platelet solutions with different concentrations. The concentration given here are the ones used to yield a satisfying fit. 1 mM NaOH has been added to the solution to set the screening length.*

Debye screening length over time due to CO_2 adsorption into the solvent. In addition, statistics tend to be poor for $h < 30$ nm and $h > 350$ nm. The potentials in Figure 4.21 are cut off at these separations to account for these limitations.

The major error sources are given by low statistics of the TEM–measurement and the irregularity of shape. The results of the TIRM and the TIRF measurements agree well, within the boundaries of their individual errors, which are estimated to be well larger than 15 percent. The mean diameter measured with TEM is overall smaller, probably an artifact of bad statistics. Another explanation for the generally larger diameter of the discs when determined by TIRF might be that the charge of the platelets was not taken into account. There are existing theoretical predictions for depletion of oblate spheroids, including the electrical double layer [102]. The double layer is of the order of the screening length (about 10 nm). Yet considering an error of over 15 percent on the diameters due to polydispersity and the shape mismatch, including the charge wouldn't improve the description of the depletion interaction. Looking at Figure 4.18 it can be seen that the measured distributions are not drastically different, strengthening the conclusion, that charge is negligible here.

c_{set} (mg/ml)	c_{fit} (mg/ml)	$\bar{D}$ (nm)	σ_D (nm)
3.60	3.94	216	27
6.00	6.60	230	61
12	13.8	247	34

Table 4.3: *Summary of fit parameters, comparing fitted concentrations to those determined by weighing.*

Conclusion

TIRF, in combination with particle tracking, is used to map a sphere–wall interaction potential. While not being fundamentally different from TIRM, it offers the advantages of removing background scattering almost completely, helping to reduce the effect of turbidity of the sample solutions. TIRF also offers the advantage of yielding high enough intensities for smaller particle sizes inaccessible with TIRM. Since the particles used here are quite large, this is not really important for the platelet measurements.

The presented measurements of depletion forces by plate–like gibbsite particles are the first ones to be done on real, rigid platelets. The successful extension of the theoretical prediction to encompass polydispersity of the depletant might also offer a way to gain information about other polydisperse systems. The modified model for depletion caused by cylindrical discs fits the measured data sets nearly perfectly. The approach of an averaged potential enables to find an estimate for the parameters of the size distribution of the depletant by means of an optical measurement. It is shown that the theory, in spite of non ideal platelets, is well suited to describing depletion caused by gibbsite platelets and that polydispersity has an imperceptible influence on the contact value.

4.3.4 Platelet induced depletion in shear gradients

As already stated, the measurements with fd virus under flow turned out to be too ambiguous to see any influence of shear field on the interaction potentials. Corresponding experiments shall be repeated here, but with platelets as a depletant instead of the rod–like fd viruses. It would be prudent to perform TIRF measurements to study the flow influenced potentials, but measurements on bare fluorescing spheres (without platelets) show that they are already influenced by a shear gradient. This effect is unexpected and not understood. To avoid the problem, the better signal to noise ratio of TIRF is sacrificed by using non fluorescing $R = 3$ µm polystyrene spheres, while doing TIRM. The measurements are again done using the HeNe laser as illumination source with a penetration depth, β^{-1}, of 150 nm. Intensity data are converted to potentials with the help of particle tracking as described in section 3.2.5. The flow is realized in the same way as in section 4.2.4 by using the flow mass controller, while

the acquisition is done again by using the camera and particle tracking . As solvent a 1 mM NaOH solution is used, which supplies the same screening length as the 2 mM Tris-HCl buffer at pH = 8.2 (κ^{-1} = 9.7 nm). When applying a flow field and measuring a potential, the expectation is given again by the naive model discussed in section 4.2.4. The platelets should align in the flow field as shown in Figure 4.22 and thus diminish the overall interaction energy.

For a infinitely thin, free platelet there is an analytical expression by Happel and Brenner [103] predicting the required shear rate (rotational diffusion of platelets), needed to fully align one platelet.

$$D_r^{\perp} = D_r^{\parallel} = \frac{k_B T}{(4/3)\eta_0 D^3} \tag{4.14}$$

where η_0 is the solvent viscosity. Calculating the diffusion coefficients for platelets with a diameter of 230 nm in water at room temperature yields D_r = 250 1/s. This is much more than for the rods. But the concentrations, generating a strong enough depletion potential, are already well above the overlap concentration, $c^* = 24\rho_{gibb}(L/D)$ = 2.5 mg/ml, of the platelets. This causes the rotational diffusion to be drastically decreased.

The illumination time of the camera is set to 10 ms and 4 times binning of the CCD chip is used, to increase the sensitivity and reduce the amount of acquired data. Potentials are measured at various flow rates, at a plate mass concentration of c_{set} = 7.2 mg/ml as determined by weighing and without platelets present. The data are shown in Figure 4.23. Different from the experiments with fd, the depletion shows exactly the predicted behaviour. Even more, it seems possible to tune the depletion interaction by varying the shear rate, in spite of the fact that the shear rates are well below the estimated value for a free particle. Looking at the

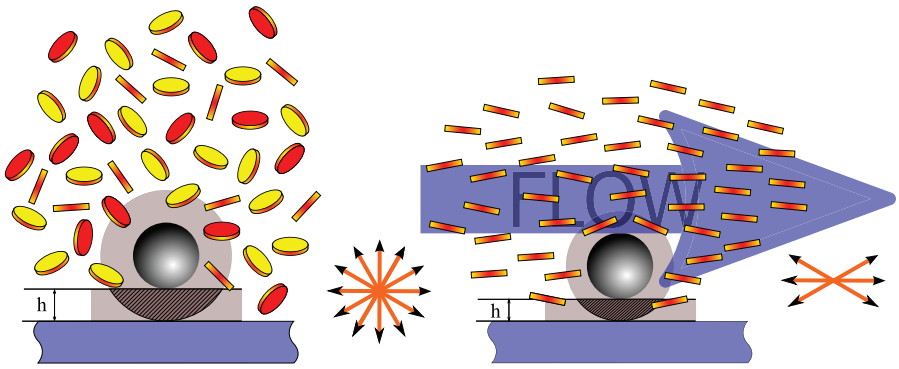

Figure 4.22: *Principal sketch of the alignment of platelets in a shear flow. The dimensions are not accurate. The simple model, described in the text, predicts a decrease of excluded volume and range with increasing shear strength.*

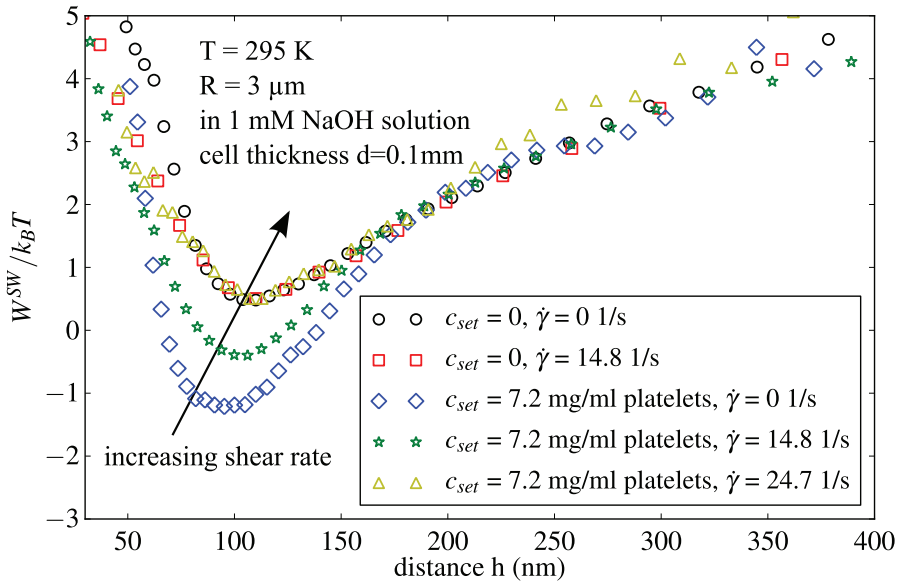

Figure 4.23: *The figure shows potentials recored with and without depletant present, measured at different shear rates and even without shear. It appears as if the depletion can be switched of when a gradient is applied. The measurements without depletant are identical with and without shear, except for some deviation in the repulsive branch.*

reference measurements without platelets, these potentials are identical, in the case of flow or no flow, except for a distortion in the repulsive branch. This has already been observed in section 4.2.4. The possible alignment of the particles at the applied shear rates indicates that there must be already a strong overlap of the platelets.

The variation in the repulsive branches in Figure 4.23 is quite pronounced. As already discussed, this is most probably connected to difference of charge on the surface of the probe particles. Nevertheless, the most part of the reference measurement and the data for bare particles under flow are almost identical. When shearing solutions with platelets present, the variation in the repulsive branch is still visible. The potentials with depletion are shifted in energy, so that the part which is caused by gravitation alone coincides for all potentials. This is done in the same fashion as for the measurements in a quiescent fluid. Applying this kind of referencing allows to visualize the potential depth. Increasing the shear rate leads to a reduction of the potential depth until the depletion practically vanishes at the maximally applied shear rate (Figure 4.23). For lower platelet concentration (c_{set} = 6mg/ml) an identical effect is observed, but the results are not shown here, because the potentials are relatively shallow, which makes it hard to see a change of the potential depth. The measurements are repeated once more with a new sample at c_{set} = 7.2 mg/ml, to exclude that this effect may just be

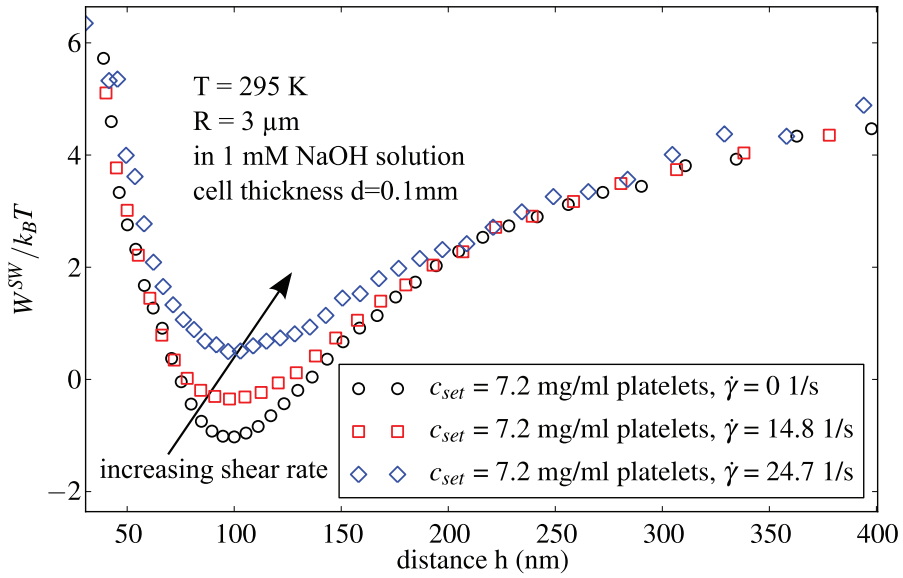

Figure 4.24: *The figure shows potentials measured at the same concentration as in Figure 4.23 at the same concentration. The effect is reproducible. No reference measurement is performed, but the potentials look a bit smoother than the onces measured before.*

created by a contamination of the sample or the sample cell. In Figure 4.24 the results are shown. The same effect is observed. This time no reference potential is taken, because only the reproducibility is of interest. It is surprising that the simple model, which was introduced, seems to describe the occurring effect for platelets in the overlap concentration region of the platelets, but not the viruses. Anyway, the next step should be to probe different concentrations. Lower concentrations than 7.2 mg/ml create a depletion effect, which is small enough that it is comparable to the instrument's measurement resolutio when applying a flow field. So a higher concentration is chosen in order to extend the scope of the experiment and the data basis.

At a mass concentration of $c_{set} = 9$ mg/ml the picture under flow is completely different from the last set of measurements. For the higher platelet mass concentration the potential measured in the quiescent state follows the prediction by creating a deeper potential well. But once a flow is applied, almost no change of the potential can be observed. Or rather, at the lowest applied shear rate of 9.7 1/s, there appears even to be an increase of the potential depth (see Figure 4.25). This is very similar to what is observed for the rods in a shear field, only that the deepening is more pronounced and a measurement artifact can be ruled out here. It might be speculated, as already hinted when the viruses in shear fields were discusses, that there is some kind of concentration limit, above which alignment is not possible anymore. What exactly

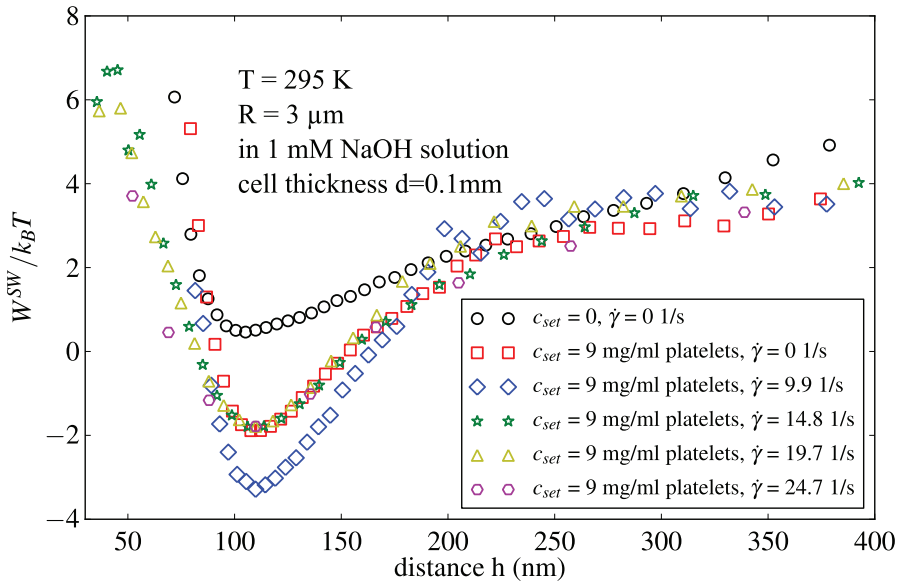

Figure 4.25: *When the concentration is increased, here to c_{set} = 9 mg/ml, it is no longer possible to "switch off" the depletion. Instead the potentials seems to deepen for the lowest applied shear rate. The curves are shifted so that the gravitational branch coincides for all measurements. It is not clear if the deepest curve really only experiences gravitation at higher distances.*

causes the behaviour to change is not clear. Inspecting the deepened curve more closely, the repulsive branch of the potential seems to have become more steep, too. Furthermore, the potential shape appears to have changed altogether (describing a quadratic potential well). All this could well indicate that some loose network is formed, which is enforced by the shear flow. But as already stated this cannot be proven by TIRM measurements.

Conclusion

Influencing depletants by shear field seems to be possible, but more experiments need to be performed in order to extend the data basis. It stays uncertain why an alignment of the platelets is only possible below a certain concentration. Standard rheological experiments are not feasible, since the solution exhibit almost the same viscosity as water, which is too small for commercially available rheometers . In addition to that, the available sample amount is very limited, so that extensive testing of the different methods is not an option at the moment. The transition to a concentration region, where no alignment is possible, is also strengthening the

measurement in section 4.2.4 for the low fd concentration, indicating the observed effect there might be more than just an artifact.

5 Summary and Outlook

The current work reports on the modification made to a standard TIRM setup to enable measurements in shear gradients. The effect of a shear flow on the depletion interaction between a sphere and a wall caused by colloidal suspensions of rods and platelets is investigated.

The thesis starts discussing different approaches, chosen to devise a technique, enabling the acquisition of potentials from colloidal probe spheres in a shear field. In a first step tentative experiments are performed, showing that standard TIRM measurements, employing tweezers and a photomultiplier as detection unit, already result in an influence of flow on the sphere–wall interaction potential. This result is not expected for spherical particles in front of a wall. In a fist attempt to create a simple model in order to explain the occurring effect, it is reasoned that the observed effect stems from the usage of optical tweezers in combination with a shear field. With the tweezers keeping a particle in place, an increase of the apparent weight force of the probe particle with increasing shear rate respectively flow is observed. The effect is strong enough to cover most other potential contributions such as depletion. Moreover, performing single particle measurements in flow fields turn out to be extremely sensitive, since the particle always has a probability to escape the optical trap during a measurement series, making the collection of data extremely time consuming. While the tweezers' effect on an interaction potential is regarded as being an obstacle on the way of measuring flow affected depletion potentials, it might offer a way to measure rotation of particles in works to come. However, when applying shear gradients during this work, the standard TIRM method is abandoned and replaced by one, working without tweezers and employing a CCD camera as detector, while using particle tracking for the analysis. In the course of a number of comparison experiments, the two methods are shown to be equivalent in quiescent state, both offering certain advantages and drawbacks. In addition, doing camera based measurement opens the possibility to do fluorescent measurements and observe multiple particles at the same time. Fluorescence

experiments yield a better signal to noise ratio and the fluorescence intensity is less dependent on the particles size, enabling measurements on relatively small particles (diameter 100 nm), which are not yet accessible.

After finishing the modifications to the setup, the depletion effect caused by fd virus, a model system for long, stiff rods with a high aspect ratio, is studied extensively. In particular, the still finite flexibility of fd virus is one focus of interest. To investigate the influence of flexibility on the depletion of fd virus two different variants are used in measurements without flow: wild type fd and the mutant Y21M. The later one is an fd variant with an altered protein in its shell, giving it a three times higher persistence length than the wild type and otherwise unchanged properties. The data collected on both variants shows no discernible difference, leading to the conclusion that the finite flexibility only plays a minor role for the depletion behaviour of fd. The depletion potentials caused by the two variants of fd virus follow the theoretical prediction for depletion due to infinitely thin, long rods well up to a certain concentration, which depends on the chosen probe sphere size. Above this concentration the measured potentials deviate from the simple depletion prediction, and they are considerably deeper than predicted. It is speculated that this might due to Coulomb interaction or a formation of a rod network close to the wall. But for the purpose of investigating structural changes of the depletant ensemble, TIRM is not the appropriate tool. Conducting experiments with a confocal microscope in the vicinity of the wall and a sphere might give more information about this phenomenon in the future. At low sphere wall separation distances a deviation between theory and measurements is found for all investigated fd concentrations. Refitting data for various probe sphere sizes with a slightly modified depletion model leads to the assumption that fd virus never exhibits pure depletion behaviour. Another possibility to explain the mismatch at small distances might be that this deviating potential is just an artifact of the employed technique, respectively a result of non perfect referencing to the potential without depletant present. To further study and confirm this effect, some independent measurements like micro rheological experiments or force measurements using optical tweezer were required. Unfortunately, this was not possible in the frame of this thesis. Conducting experiments in shear field with fd virus as a depletant gives no indication of an influence of flow. There a some small variations between flow affected depletion potentials and the ones at rest, but the difference is that small that it coincides with the prevalent, inherent measurement error of the technique. The lack of an effect is attributed to the fact that the investigated rod concentrations are already well in the overlap region. This results in a drastic slowdown of the rotational diffusion due to interactions between the rods, which are not taken into consideration for the simple model, predicting an alignment of the rod like depletants.

A second system investigated in the scope of this thesis are silica coated gibbsite platelets. Like fd viruses they are used to study depletion behaviour. In contrast to rod like depletants, no earlier studies comparing theoretical models to the direct oberservation of the depletion effect of plate shaped depletants exist. Due to slight turbidity of the platelet suspensions and possible interaction with the optical tweezers, the potential measurements are performed fluorescently (TIRF). After extending an existing theoretical description for perfectly monodisperse, infinitely thin, circular platelets to account for polydispersity, very good agreement between measurement and theory is found. Furthermore, the modifications to the theory allows to measure the parameters of the platelets' size distribution by fitting the modified model to the experimental depletion potentials. The determined parameters agree well with those determined by TEM measurements. Complementing the measurement in rest, experiments in a flow field are performed. Although for the platelets the necessary shear rates required to align a free platelet are expected to be 10 times higher as compared to the fd viruses, the generated shear gradient appears to influence the depletion behaviour of the platelets. With increasing shear rate, the potentials depth is diminished until the potential becomes indistinguishable from the one without platelets. This is exactly the effect anticipated when considering simple alignment of the rods. Still the applied shear rates are well below the estimated value, above which rotational diffusion should be suppressed. Nevertheless, the investigated concentrations are well within the overlap region, giving rise to a drastically reduced rotational diffusion. Experiments at higher platelet mass concentrations show a behaviour, similar to the one observed for the fd viruses. But at low shear rates even a deepening and change in shape of the potential is observed. Due to a limited amount of platelet sample, further experiments were not possible up to this point. Except for some speculations,no solid explanation for the occurring phenomena may be offered at the moment.

For future work the behaviour in flow fields of shorter and longer rod–like depletants in the form of viruses is of interest. The change of the depletion when a shear gradient is imposed on a platelet suspension needs to be further studied. Here, confocal microscopy studies of labeled platelets or viruses might offer a way to get a better understanding of the underlying mechanism, giving a hint to the change of behaviour when shearing at higher concentrations.

Zusammenfassung

Gegenstand der Arbeit ist die Untersuchung des Einflusses von Suspensionen kolloidaler Stäbchen und Plättchen auf das Wechselwirkungspotential zwischen einer Sondenkugel und einer Wand mit Hilfe von totaler interner Relflexionsmikroskopie (TIRM) in ruhenden Sys-

temen und solchen, die einem Schergradienten ausgesetzt werden. Der erste Teil der Arbeit befasst sich mit der Erweiterung der TIRM–Methode zur Messung in Scherfeldern. Es zeigt sich, dass das Standardverfahren, welches auf der Messung an einzelnen Partikeln beruht, für die Messung in Scherströmungen ungeeignet ist. Im Rahmen der Modifikationen wird der gewöhnlich verwendete Sekundärelektronenvervielfacher durch eine CCD–Kamera ersetzt. Statt Einzelpartikelmessungen erfolgt die Messung vieler Partikel zur selben Zeit. Es lässt sich durch Vergleich zeigen, dass der Einsatz der Kamera weitgehend äquivalent zur Verwendung der Standardmethode ist und zu den selben Ergebnissen führt. Außerdem erweitert die Kamera den Aufbau um die Option der Messung mit fluoreszenten Sondenpartikeln. Als erstes experimentelles System werden stäbchenförmige Verarmungskolloide, sogenannte fd–Viren untersucht. Diese Messungen geschehen einerseits in Ruhe als allgemeine Referenz und andererseits unter Scherung. Die Viren werden dabei als Modellsystem für steife Stäbchen betrachtet. Während der statischen Messungen wird der Einfluss der letztlich doch finiten Flexibiltät der Stäbchen auf die erzeugten Verarmungspotentiale durch Vergleich mit einem, bis auf höhere Steifigkeit identischen, Virusmutanten (Y21M) studiert. Im Rahmen der Genauigkeit von TIRM–Messungen kann kein statistisch relevanter Unterschied zwischen den beiden Varianten ausgemacht werden. Die Viren folgen den theoretischen Vorhersagen für unendlich dünne, lange Stäbchen sehr gut, bis hin zu einer gewissen Schwellenkonzentration, was im Widerspruch zu früheren Arbeiten steht. Oberhalb dieser, von der Sondenkugelgröße abhängigen, Schwellenkonzentration weichen die gemessenen Potentiale deutlich von der Vorhersage ab, und die Wechselwirkungsenergien sind wesentlich höher als dies theoretisch vorausgesagt wird. Stäbchensuspensionen, die einem Scherfeld ausgesetzt werden, zeigen widererwarten keine veränderten Veramungswechselwirkungseigenschaften. Als zweites experimentelles Modellsytem werden Gibbsitplättchen eingesetzt. Es gelingt hier zum ersten mal eine Messung einer von Plättchen verursachter Verarmungswechselwirkung. Nach Erweiterung einer existierenden Theorie auf moderat polydisperse Systeme, zeigt sich gute Übereinstimmung zwischen Modell und Messung. Ergebnisse von Messungen in Scherfeldern unter Anwesenheit der Plättchen weisen darauf hin, dass bei nicht allzu hohen Plättchenmassenkonzentrationen die Verarmungspotentialtiefe kontinuierlich durch Erhöhung der Scherrate verringert werden kann, was auf eine Ausrichtung der Plättchen schließen lässt. Bei höheren Konzentrationen ist das Verhalten ähnlich zu den Beobachtungen bei Stäbchen (keine Änderung). Im Gegenteil zeigt sich eine Vertiefung des Potentials für spezifische Scherraten.

Acknowledgements

At this point I want to thank everybody who supported me in one way or another during my work. First I would like to express my gratitude to Dr. Peter. Lang for his excellent supervision and giving me the possibility to work on the interesting topic of surface effects and near wall interactions.

I want to thank Professor Stefan Egelhaaf for taking over the co–supervision of my thesis, and Professor Jan Dhont for giving me the opportunity to do my PhD in the soft matter group in Jülich.

Further, I would like to thank Dr. Pavlik Lettinga for supplying me with fd virus samples and giving helpful advice on microscopy techniques, which made a great part of my thesis only possible; Dr. Dzina Kleshchanok for providing me with a generous amount of silica coated gibbsite platelets, with which the depletion behaviour of platelets could be experimentally studied for the first time; and Dr. Simon Rogers for reading my thesis and helping me with the English grammar. I thank the rest of my colleagues for the nice working atmosphere and many helpful discussions.

Especially, I would like to thank my family and friends for their constant support.

Die hier vorgelegte Dissertation habe ich eigenständig und ohne unerlaubte Hilfe angefertigt. Die Dissertation wurde in der vorgelegten oder in ähnlicher Form noch bei keiner anderen Institution eingereicht. Ich habe bisher keine erfolglosen Promotionsversuche unternommen.

Düsseldorf, den 14.09.2011

Christoph July

List of Figures

List of Tables

Bibliography

[1] Henk N.W. Lekkerkerker and Remco Tuinier. *Colloids and the Depletion Interaction*. Springer, 2011.

[2] Fumio Oosawa and Sho Asakura. Surface tension of high-polymer solutions. *The Journal of Chemical Physics*, 22(7):1255–1255, 1954.

[3] Sho Asakura and Fumio Oosawa. Interaction between particles suspended in solutions of macromolecules. *J. Polym. Sci*, 33(126):183–192, 1958.

[4] Davide Marenduzzo, Kieran Finan, and Peter R. Cook. The depletion attraction: an underappreciated force driving cellular organization. *The Journal of Cell Biology*, 175(5):681–686, 2006.

[5] G. Binnig, C. F. Quate, and Ch. Gerber. Atomic force microscope. *Phys. Rev. Lett.*, 56(9):930–933, Mar 1986.

[6] W. K. Wijting, W. Knoben, N. A. M. Besseling, F. A. M. Leermakers, and M. A. Cohen Stuart. Depletion interaction measured by colloidal probe atomic force microscopy. *Phys. Chem. Chem. Phys.*, 6:4432–4439, 2004.

[7] David G Grier. Optical tweezers in colloid and interface science. *Current Opinion in Colloid & Interface Science*, 2(3):264 – 270, 1997.

[8] D. L. Sober and J. Y. Walz. Measurement of long range depletion energies between a colloidal particle and a flat surface in micellar solutions. *Langmuir*, 11(7):2352–2356, 1995.

[9] Amber Sharma and John Y. Walz. Direct measurement of the depletion interaction in a charged colloidal dispersion. *J. Chem. Soc., Faraday Trans.*, 92:4997–5004, 1996.

[10] Edward S. Pagac, Robert D. Tilton, and Dennis C. Prieve. Depletion attraction caused by unadsorbed polyelectrolytes. *Langmuir*, 14(18):5106–5112, 1998.

[11] Zvonimir Dogic, Kirstin R. Purdy, Eric Grelet, Marie Adams, and Seth Fraden. Isotropic-nematic phase transition in suspensions of filamentous virus and the neutral polymer dextran. *Phys. Rev. E*, 69(5):051702, May 2004.

[12] W. Neil Everett, Richard E. Beckham, Kenith Meissner, and Michael A. Bevan. Evanescent wave excited luminescence from levitated quantum dot modified colloids. *Langmuir*, 23(17):8950–8956, 2007.

[13] Laurent Helden. *Untersuchung von Partikel-Wand-Wechselwirkung mit evaneszenter Lichtstreuung*. PhD thesis, Universität Konstanz, 2003.

[14] Z. Dogic and S. Fraden. Development of model colloidal liquid crystals and the kinetics of the isotropic, semectic transition. *Philosophical Transactions of the Royal Society of London. Series A:Mathematical, Physical and Engineering Sciences*, 359(1782):997–1015, 2001.

[15] A. P. Gast, C. K. Hall, and W. B. Russel. Polymer-induced phase separations in nonaqueous colloidal suspensions. *Journal of Colloid and Interface Science*, 96(1):251 – 267, 1983.

[16] Monique H. Vingerhoeds, Theo B.J. Blijdenstein, Franklin D. Zoet, and George A. van Aken. Emulsion flocculation induced by saliva and mucin. *Food Hydrocolloids*, 19(5):915 – 922, 2005.

[17] Erika Silletti, Monique H. Vingerhoeds, Willem Norde, and George A. van Aken. The role of electrostatics in saliva-induced emulsion flocculation. *Food Hydrocolloids*, 21(4):596 – 606, 2007.

[18] Erik ten Grotenhuis, Remco Tuinier, and Cornelus G. de Kruif. Phase stability of concentrated dairy products. *J Dairy Sci*, 86(3):764–769, March 2003.

[19] P. Debye. Light scattering in solutions. *J. Appl. Phys.*, 15(4):338–342, 1944.

[20] Bruno H. Zimm. Molecular theory of the scattering of light in fluids. *J.Chem. Phys.*, 13(4):141–145, 1945.

[21] Bruce J. Berne and Robert Pecora. *Dynamic Light Scattering*. Dover Publications Inc., 1976.

[22] Jacob N. Israelachvili and Gayle E. Adams. Measurement of forces between two mica surfaces in aqueous electrolyte solutions in the range 0-100 nm. *J. Chem. Soc., Faraday Trans. 1*, 74:975–1001, 1978.

[23] Dirk L. J. Vossen, Astrid van der Horst, Marileen Dogterom, and Alfons van Blaaderen. Optical tweezers and confocal microscopy for simultaneous three-dimensional manipulation and imaging in concentrated colloidal dispersions. *Rev. sci. Instrum.*, 75(9):2960–2970, 2004.

[24] Eric M. Furst. Interactions, structure, and microscopic response: Complex fluid rheology using laser tweezers. *Soft Materials*, 1(2):167–185, 2003.

[25] William A. Ducker, Tim J. Senden, and Richard M. Pashley. Direct measurement of colloidal forces using an atomic force microscope. *Nature*, 353(6341):239–241, September 1991.

[26] Dennis C. Prieve. Measurement of colloidal forces with tirm. *Advances in Colloid and Interface Science*, 82(1-3):93 – 125, 1999.

[27] John Y Walz. Measuring particle interactions with total internal reflection microscopy. *Current Opinion in Colloid & Interface Science*, 2(6):600 – 606, 1997.

[28] Simon Biggs, Dennis C. Prieve, and Raymond R. Dagastine. Direct comparison of atomic force microscopic and total internal reflection microscopic measurements in the presence of nonadsorbing polyelectrolytes. *Langmuir*, 21(12):5421–5428, 2005.

[29] Michael A. Bevan and Dennis C. Prieve. Direct measurement of retarded van der waals attraction. *Langmuir*, 15(23):7925–7936, 1999.

[30] C. Hertlein, L. Helden, A. Gambassi, S. Dietrich, and C. Bechinger. Direct measurement of critical casimir forces. *Nature*, 451(7175):172–175, January 2008.

[31] Florian Soyka, Olga Zvyagolskaya, Christopher Hertlein, Laurent Helden, and Clemens Bechinger. Critical casimir forces in colloidal suspensions on chemically patterned surfaces. *Phys. Rev. Lett.*, 101(20):208301, Nov 2008.

[32] C. Bechinger, D. Rudhardt, R. Roth P. Leiderer, and S. Dietrich. Understanding depletion forces beyond entropy. *Phys. Rev. Lett.*, 83,19:3960–3963, 1999.

[33] Dzina Kleshchanok, Remco Tuinier, and Peter R. Lang. Direct measurements of polymer-induced forces. *J. Phys.: Cond. Matt.*, 20(7):073101, FEB 20 2008.

[34] Xiaochen Xing, Zifu Li, and To Ngai. ph-controllable depletion attraction induced by microgel particles. *Macromolecules*, 42:7271–7273, 2009.

[35] Amit Kulkarni and Charles Zukoski. Depletion interactions and protein crystallization. *Journal of Crystal Growth*, 232(1-4):156 – 164, 2001. Proceedings of the Eighth International Conference on Crystalliza tion of Biological Macromolecules.

[36] Christoph Gögelein. *Phase Behaviour of Proteeins and Colloid-Polymer Mixtures*. PhD thesis, Heinrich-Heine-Universität-Düsseldorf, 2008.

[37] B Neu and HJ Meiselman. Depletion-mediated red blood cell aggregation in polymer solutions. *Biophy. Jour.*, 83(5):2482–2490, NOV 2002.

[38] R. Roth and R. Evans. The depletion potential in non-additive hard-sphere mixtures. *Europhys. Lett.*, 53(2):271, 2001.

[39] Y.-L. Chen and K. S. Schweizer. Depletion interactions in suspensions of spheres and rod–polymers. *J. Chem. Phys.*, 117:3, 2002.

[40] Y Mao, ME Cates, and HNW Lekkerkerker. Theory of the depletion force due to rodlike polymers. *J. Chem. Phys.*, 106(9):3721–3729, MAR 1 1997.

[41] Dzina Kleshchanok, Remco Tuinier, and Peter R. Lang. Depletion interaction mediated by a polydisperse polymer studied with total internal reflection microscopy. *Langmuir*, 22(22):9121–9128, 2006.

[42] Y. K. Leong. Depletion interaction in colloidal suspensions: a comparison between theory and experiment. *Colloids and Surfaces A*, 118(1-2):107 – 114, 1996.

[43] P. Holmqvist, D. Kleshchanok, and Peter R. Lang. Interaction potential and near wall dynamics of spherical colloids in suspension of rod-like fd-virus. *Eur. Phys. J. E*, 26:177–182, 2008.

[44] Peter Holmqvist, Dzina Kleshchanok, and Peter R. Lang. Unexpected slow near wall dynamics of spherical colloids in a suspension of rods. *Langmuir*, 23(24):12010–12015, 2007.

[45] Keng-hui Lin, John C. Crocker, Ana C. Zeri, and A. G. Yodh. Colloidal interactions in suspensions of rods. *Phys. Rev. Lett.*, 87(8):088301, Aug 2001.

[46] Laurent Helden, Gijsje H. Koenderink, Paul Leiderer, and Clemens Bechinger. Depletion potentials induced by charged colloidal rods. *Langmuir*, 20(14):5662–5665, 2004. PMID: 16459575.

[47] L. Helden, R. Roth, G. H. Koenderink, P. Leiderer, and C. Bechinger. Direct measurement of entropic forces induced by rigid rods. *Phys. Rev. Lett.*, 90(4):048301, Jan 2003.

[48] Jianxin Tang and Seth Fraden. Isotropic–cholesteric phase transition in colloidal suspensions of filamentous bacteriophagefd. *Liquid Crystals*, 19:459–467, 1994.

[49] H. Van Olphen. *An introduction to clay colloid chemistry*. Wiley,NY, 1977.

[50] Herman Z. Cummins. Liquid, glass, gel: The phases of colloidal laponite. *Journal of Non-Crystalline Solids*, 353(41-43):3891 – 3905, 2007.

[51] Haydn H. Murray. Traditional and new applications for kaolin, smectite, and palygorskite: a general overview. *Applied Clay Science*, 17(5-6):207 – 221, 2000.

[52] G.C Maitland. Oil and gas production. *Current Opinion in Colloid & Interface Science*, 5(5-6):301 – 311, 2000.

[53] A. Ashkin. Acceleration and trapping of particles by radiation pressure. *Physical Review Letters*, 24:156–, 1970.

[54] John Y. Walz and Dennis C. Prieve. Prediction and measurement of the optical trapping forces on a microscopic dielectric sphere. *Langmuir*, 8(12):3073–3082, 1992.

[55] Herman von Helmholtz. Studien über elektrische grenzschichten. *Annalen der Physik und Chemie*, 7:337, 1879.

[56] Otto Stern. Zur theorie der elektrolytischen doppelschicht. *Z. Electrochem.*, 30:508, 1924.

[57] Jacob N. Israelchivili. *Intermolecular & Surface Forces*. Academic Press, 1991.

[58] Hans-Jürgen Butta, Karlheinz Graf, and Michael Kappl. *Physics and Chemistry of Interfaces*. Wily-VCH, 2006.

[59] B. Derjaguin. Untersuchungen fiber die reibung und adhäision. *Kolloid Zeits.*, 69:155, 1934.

[60] B. V. Derjaguin, V. M. Muller, and Yu. P. Toporov. Effect of contact deformations on the adhesion of particles. *Journal of Colloid and Interface Science*, 53(2):314 – 326, 1975.

[61] H.C. Hamaker. The london–van der waals attraction between spherical particles. *Physica*, 4(10):1058 – 1072, 1937.

[62] Martin Piech and John Y. Walz. Depletion interactions produced by nonadsorbing charged and uncharged spheroids. *Journal of Colloid and Interface Science*, 232(1):86 – 101, 2000.

[63] Paul C. OdiachiJr. and Dennis C. Prieve. Effect of added salt on the depletion attraction caused by non-adsorbing clay particles. *Colloids and Surfaces A*, 146(1-3):315 – 328, 1999.

[64] Herman Chew, Dau-Sing Wang, and Milton Kerker. Elastic scattering of evanescent electromagnetic waves. *Appl. Opt.*, 18(15):2679–2687, Aug 1979.

[65] Gustav Mie. Beiträge zur optik trüber medien, speziell kolloidaler metalllösungen. *Annalen der Physik*, 25:377, 1908.

[66] Christopher Hertlein, Norbert Riefler, Elena Eremina, Thomas Wriedt, Yuri Eremin, Laurent Helden, and Clemens Bechinger. Experimental verification of an exact evanescent light scattering model for tirm. *Langmuir*, 24(1):1–4, 2008. PMID: 18052301.

[67] D.C.PrieveandJ.Y.Walz. Scattering of an evanescent surface wave by a microscopic dielectric sphere. *Appl. Opt.*, 32:1629–1641, 1993.

[68] Norbert Riefler, Elena Eremina, Christopher Hertlein, Laurent Helden, Yuri Eremin, Thomas Wriedt, and Clemens Bechinger. Comparison of t-matrix method with discrete sources method applied for total internal reflection microscopy. *Journal of Quantitative Spectroscopy and Radiative Transfer*, 106(1-3):464 – 474, 2007.

[69] Giovanni Volpe, Thomas Brettschneider, Laurent Helden, and Clemens Bechinger. Novel perspectives for the application of total internal reflection microscopy. *Optics Express*, 17:23975–23985, 2009.

[70] Christopher W. Macosko. *Rheology Principles, Measurements, and Applications*. Wily-Vch, 1994.

[71] Wolfgang Demtröder. *Experimentalphysik 1*. Springer, 2001.

[72] John C. Crocker and David G. Grier. Methods of digital video microscopy for colloidal studies. *Journal of Colloid and Interface Science*, 179(1):298 – 310, 1996.

[73] Michael A. Bevan and Dennis C. Prieve. Hindered diffusion of colloidal particles very near to a wall: Revisited. *J. Chem. Phys.*, 113(3):1228–1236, 2000.

[74] Nasser A. Frej and Dennis C. Prieve. Hindered diffusion of a single sphere very near a wall in a nonuniform force field. *J. Chem. Phys.*, 98(9):7552–7564, 1993.

[75] H. Brenner. The slow motion of a sphere through a viscous fluid towardds a plane surface. *Chemical engineering science*, 16(3-4):242–251, 1961.

[76] Steven A. Berkowitz and Loren A. Day. Mass, length, composition and structure of the filamentous bacterial virus fd. *Journal of Molecular Biology*, 102(3):531 – 547, 1976.

[77] S. A. Reisberg L. A. Day, C. J. Marzee and A. Casadevall. Dna packing in filamentous bacteriophages. *Ann. Rev. Biophys.*, 17:509–539, 1988.

[78] A. W. C. Lau, Keng-Hui Lin, and A. G. Yodh. Entropic interactions in suspensions of semiflexible rods: Short-range effects of flexibility. *Phys. Rev. E*, 66(2):020401, Aug 2002.

[79] Ahmad S. Khalil, Jorge M. Ferrer, Ricardo R. Brau, Stephen T. Kottmann, Christopher J. Noren, Matthew J. Lang, and Angela M. Belcher. Single M13 bacteriophage tethering and stretching. *Proceedings of the National Academy of Sciences*, 104(12):4892–4897, 2007.

[80] D.A.Marvin and B. Hohn. Filamentous bacterial viruses. *Bact. Rev.*, 53:172–2009, 1969.

[81] Edward Barry, Daniel Beller, and Zvonimir Dogic. A model liquid crystalline system based on rodlike viruses with variable chirality and persistence length. *Soft Matter*, 5(13):2563–2570, 2009.

[82] Wee M Tan, Raz Jelinek, Stanley J Opella, Pratap Malik, Tamsin D Terry, and Richard N Perham. Effects of temperature and y21m mutation on conformational heterogeneity of the major coat protein (pviii) of filamentous bacteriophage fd. *Journal of Molecular Biology*, 286(3):787 – 796, 1999.

[83] Kirstin R. Purdy and Seth Fraden. Isotropic-cholesteric phase transition of filamentous virus suspensions as a function of rod length and charge. *Phys. Rev. E*, 70(6):061703, Dec 2004.

[84] Anieke M. Wierenga, Tjerk A. J. Lenstra, and Albert P. Philipse. Aqueous dispersions of colloidal gibbsite platelets: synthesis, characterisation and intrinsic viscosity measurements. *Colloids and Surfaces A*, 134(3):359 – 371, 1998.

[85] Zvonimir Dogic and Seth Fraden. Ordered phases of filamentous viruses. *Current Opinion in Colloid & Interface Science*, 11(1):47 – 55, 2006.

[86] Felix M. van der Kooij, Katerina Kassapidou, and Henk N. W. Lekkerkerker. Liquid crystal phase transitions in suspensions of polydisperse plate-like particles. *Nature*, 406(6798):868–871, August 2000.

[87] Judith E. G. J. Wijnhoven. Coating of gibbsite platelets with silica. *Chemistry of Materials*, 16(20):3821–3828, 2004.

[88] Dr. David Lide. *CRC Handbook of Chemistry and Physics, 91*. Taylor and Francis Group, LLC, 2010.

[89] Vittorio Degiorgio, Roberto Piazza, and Robert B. Jones. Rotational diffusion in concentrated colloidal dispersions of hard spheres. *Phys. Rev. E*, 52(3):2707–2717, Sep 1995.

[90] Johan Buitenhuis, Jan K. G. Dhont, and Henk N. W. Lekkerkerker. Static and dynamic light scattering by concentrated colloidal suspensions of polydisperse sterically stabilized boehmite rods. *Macromolecules*, 27:7267–7277, 1994.

[91] A Ashkin and JM Dziedzic. Optical trapping and manipulation of viruses and bacteria. *Science*, 235(4795):1517–1520, March 1987.

[92] Pablo Blanco, Hartmut Kriegs, M. Paul Lettinga, Peter Holmqvist, and Simone Wiegand. Thermal diffusion of a stiff rod-like mutant y21m fd-virus. *Biomacromolecules*, 12(5):1602–1609, 2011.

[93] Kirstin R. Purdy and Seth Fraden. Influence of charge and flexibility on smectic phase formation in filamentous virus suspensions. *Phys. Rev. E*, 76(1):011705, Jul 2007.

[94] Y. Mao, M. E. Cates, and H. N. W. Lekkerkerker. Depletion stabilization by semidilute rods. *Phys. Rev. Lett.*, 75(24):4548–4551, Dec 1995.

[95] K. Yaman, C. Jeppesen, and C. M. Marques. Depletion forces between two spheres in a rod solution. *EPL (Europhysics Letters)*, 42(2):221, 1998.

[96] Christian Graf, Hansgerd Kramer, Martin Deggelmann, Martin Hagenbüchle, Christian Johner, Christoph Martin, and Reinhart Weber. Rheological properties of suspensions of interacting rodlike fd–virus particles. *J. Chem,.Phys.*, 98(6):4920–4928, 1993.

[97] R G Winkler, K Mussawisade, M Ripoll, and G Gompper. Rod-like colloids and polymers in shear flow: a multi-particle–collision dynamics study. *Journal of Physics: Condensed Matter*, 16(38):S3941, 2004.

[98] J. K. G. Dhont. *An Introduction to Dynamics of Colloids*. Elsevier, 1996.

[99] L. Chasteen, J. Ayriss, P. Pavlik, and A. R. M. Bradbury. Eliminating helper phage from phage display. *Nucleic Acids Research*, 34(21):e145, 2006.

[100] S. M. Oversteegen and H. N. W. Lekkerkerker. Testing the derjaguin approximation for colloidal mixtures of spheres and disks. *Phys. Rev. E*, 68(2):021404, Aug 2003.

[101] Peter R. Lang. Depletion interaction mediated by polydisperse rods. *J. Chem. Phys.*, 127(12):124906, SEP 28 2007.

[102] Martin Piech and John Y. Walz. Analytical expressions for calculating the depletion interaction produced by charged spheres and spheroids. *Langmuir*, 16(21):7895–7899, 2000.

[103] J. Happel and H. Brenner. *Low Reynolds number hydrodynamics*. kluwer the language of science, 1963.

1. **Soft Matter**
   From Synthetic to Biological Materials
   Lecture manuscripts of the 39th IFF Spring School March 3 – 14, 2008
   Jülich, Germany
   edited by J.K.G. Dhont, G. Gompper, G. Nägele, D. Richter, R.G. Winkler (2008),
   c. 1000 pages
   ISBN: 978-3-89336-517-3

2. **Structural analysis of diblock copolymer nanotemplates using grazing incidence scattering**
   by D. Korolkov (2008), III, 167 pages
   ISBN: 978-3-89336-522-7

3. **Thermal Nonequilibrium**
   Thermal forces in fluid mixtures
   Lecture Notes of the 8th International Meeting on Thermodiffusion,
   9 – 13 June 2008, Bonn, Germany
   edited by S. Wiegand, W. Köhler (2008), 300 pages
   ISBN: 978-3-89336-523-4

4. **Synthesis of CMR manganites and ordering phenomena in complex transition metal oxides**
   by H. Li (2008), IV, 176 pages
   ISBN: 978-3-89336-527-2

5. **Neutron Scattering**
   Lectures of the JCNS Laboratory Course held at the Forschungszentrum Jülich and the research reactor FRM II of TU Munich
   edited by R. Zorn, Th. Brückel, D. Richter (2008), ca. 500 pages
   ISBN: 978-3-89336-532-6

6. **Ultrafast Magnetization Dynamics**
   by S. Woodford (2008), 130 pages
   ISBN: 978-3-89336-536-4

7. **Role of Surface Roughness inTribology: from Atomic to Macroscopic Scale**
   by C. Yang (2008), VII, 166 pages
   ISBN: 978-3-89336-537-1

8. **Strahl- und Spindynamik von Hadronenstrahlen in Mittelenergie-Ringbeschleunigern**
   von A. Lehrach (2008), II, 171 Seiten
   ISBN: 978-3-89336-548-7

9. **Phase Behaviour of Proteins and Colloid-Polymer Mixtures**
   by C. Gögelein (2008), II, 147 pages
   ISBN: 978-3-89336-555-5

10. **Spintronics – From GMR to Quantum Information**
    Lecture Notes of the 40th IFF Spring School March 9 – 20, 2009
    Jülich, Germany
    edited by St. Blügel, D. Bürgler, M. Morgenstern, C. M. Schneider,
    R. Waser (2009), c. 1000 pages
    ISBN: 978-3-89336-559-3

11. **ANKE / PAX Workshop on SPIN Physics**
    JINR, Dubna, Russia / June 22. – 26, 2009
    Org. Committee: A. Kacharava, V. Komarov, A. Kulikov, P. Lenisa, R. Rathmann,
    H. Ströher (2009), CD-ROM
    ISBN: 978-3-89336-586-9

12. **Entwicklung einer Nanotechnologie-Plattform für die Herstellung Crossbar-basierter Speicherarchitekturen**
    von M. Meier (2009), 135 Seiten
    ISBN: 978-3-89336-598-2

13. **Electronic Oxides –**
    Correlation Phenomena, Exotic Phases and Novel Functionalities
    Lecture Notes of the 41st IFF Spring School March 8 – 19, 2010
    Jülich, Germany
    edited by St. Blügel, T. Brückel, R. Waser, C.M. Schneider (2010), ca. 1000 pages
    ISBN: 978-3-89336-609-5

14. **4th Georgian-German School and Workshop in Basic Science**
    Tbilisi, Georgia / May 3 – 7, 2010
    Org. Committee: E. Abrosimova, R. Botchorishvili, A. Kacharava, M. Nioradze,
    A. Prangishvili, H. Ströher (2010); CD-ROM
    ISBN: 978-3-89336-629-3

15. **Neutron Scattering**
    Lectures of the JCNS Laboratory Course held at Forschungszentrum Jülich and the research reactor FRM II of TU Munich
    edited by Th. Brückel, G. Heger, D. Richter, G. Roth and R. Zorn (2010),
    ca 350 pages
    ISBN: 978-3-89336-635-4

16. **Ab *initio* investigations of magnetic properties of ultrathin transition-metal films on *4d* substrates**
    by A. Al-Zubi (2010), II, 143 pages
    ISBN: 978-3-89336-641-5

17. **Investigation of a metal-organic interface realization and understanding of a molecular switch**
    by O. Neucheva (2010), 134 pages
    ISBN: 978-3-89336-650-7

18. **Reine Spinströme in lateralen Spinventilen, *in situ* Erzeugung und Nachweis**
von J. Mennig (2010), V, 95 Seiten
ISBN: 978-3-89336-684-2

19. **Nanoimprint Lithographie als Methode zur chemischen Oberflächenstrukturierung für Anwendungen in der Bioelektronik**
von S. Gilles (2010), II, 169 Seiten
ISBN: 978-3-89336-686-6

20. **Macromolecular Systems in Soft- and Living-Matter**
Lecture Notes of the 42nd IFF Spring School 2011 February 14 – 25, 2011 Jülich, Germany
edited by J. K.G. Dhont, G. Gompper, P. R.Lang, D. Richter, M. Ripoll, D. Willbold, R. Zorn (2011), ca. 1000 pages
ISBN: 978-3-89336-688-0

21. **The spin structure of magnetic nanoparticles and in magnetic nanostructures**
by S. Disch (2011), V, 342 pages
ISBN: 978-3-89336-704-7

22. **Element-selective and time-resolved magnetic investigations in the extreme ultraviolet range**
by P. Grychtol (2011), xii, 144 pages
ISBN: 978-3-89336-706-1

23. **Spin-Transfer Torque Induced Dynamics of Magnetic Vortices in Nanopillars**
by V. Sluka (2011), 121 pages
ISBN: 978-3-89336-717-7

24. **Adsorption von Phthalocyaninen auf Edelmetalloberflächen**
von I. Kröger (2011), vi, 206 Seiten
ISBN: 978-3-89336-720-7

25. **Time-Resolved Single Molecule FRET Studies on Folding/Unfolding Transitions and on Functional Conformational Changes of Phosphoglycerate Kinase**
by T. Rosenkranz (2011), III, 139 pages
ISBN: 978-3-89336-721-4

26. **NMR solution structures of the MloK1 cyclic nucleotide-gated ion channel binding domain**
by S. Schünke (2011), VI, (getr. pag.)
ISBN: 978-3-89336-722-1

27. **Neutron Scattering**
Lectures of the JCNS Laboratory Course held at Forschungszentrum Jülich and the research reactor FRM II of TU Munich
edited by Th. Brückel, G. Heger, D. Richter, G. Roth and R. Zorn (2011), ca 350 pages
ISBN: 978-3-89336-725-2

28. **Neutron Scattering**
Experiment Manuals of the JCNS Laborator Course held at Forschungszentrum Jülich and the research reactorFRM II of TU Munich
edited by Th. Brückel, G. Heger, D. Richter, G. Roth and R. Zorn (2011), ca. 180 pages
ISBN: 978-3-89336-726-9

29. **Silicon nanowire transistor arrays for biomolecular detection**
by X.T.Vu (2011), vii, 174 pages
ISBN: 978-3-89336-739-9

30. **Interactions between parallel carbon nanotube quantum dots**
by K. Goß (2011), viii, 139 pages
ISBN: 978-3-89336-740-5

31. **Effect of spin-orbit scattering on transport properties of low-dimensional dilute alloys**
by S. Heers (2011), viii, 216 pages
ISBN: 978-3-89336-747-4

32. **Charged colloids and proteins: Structure, diffusion, and rheology**
by M. Heinen (2011), xii, 186 pages
ISBN: 978-3-89336-751-1

33. **Scattering Methods for Condensed Matter Research: Towards Novel Applications at Future Sources**
Lecture Notes of the 43rd IFF Spring School 2012
March 5 – 16, 2012 Jülich, Germany
edited by M. Angst, T. Brückel, D. Richter, R. Zorn ca. 1000 pages
ISBN: 978-3-89336-759-7

34. **Single-Site Green Function of the Dirac Equation for Full-Potential Electron Scattering**
by P. Kordt (2012), 138 pages
ISBN: 978-3-89336-760-3

35. **Time Resolved Single Molecule Fluorescence Spectroscopy on Surface Tethered and Freely Diffusing Proteins**
by D. Atta (2012), iv, 126 pages
ISBN: 978-3-89336-763-4

36. **Fabrication and Utilization of Mechanically Controllable Break Junction for Bioelectronics**
by D. Xiang (2012), 129 pages
ISBN: 978-3-89336-769-6

37. **Contact Mechanics and Friction of Elastic Solids on Hard and Rough Substrates**
by B. Lorenz (2012), iv, 121 pages
ISBN: 978-3-89336-779-5

38. **Ab initio Calculations of Spin-Wave Excitation Spectra from Time-Dependent Density-Functional Theory**
by M. Niesert (2012), 146 pages
ISBN: 978-3-89336-786-3

39. **Neutron Scattering**
Lectures of the JCNS Laboratory Course held at Forschungszentrum Jülich and the research reactor FRM II of TU Munich
edited by Th. Brückel, G. Heger, D. Richter, G. Roth and R. Zorn (2012), ca 350 pages
ISBN: 978-3-89336-789-4

40. **Neutron Scattering**
Experiment Manuals of the JCNS Laborator Course held at Forschungszentrum Jülich and the research reactorFRM II of TU Munich
edited by Th. Brückel, G. Heger, D. Richter, G. Roth and R. Zorn (2012), ca. 175 pages
ISBN: 978-3-89336-790-0

41. **Influence of a shear flow on colloidal depletion interaction**
by C. July (2012), xviii, 105 pages
ISBN: 978-3-89336-791-7

Schlüsseltechnologien / Key Technologies
Band / Volume 41
ISBN 978-3-89336-791-7

JÜLICH
FORSCHUNGSZENTRUM